

University of Cincinnati

Date: 3/9/2015

I, Shirley Peng, hereby submit this original work as part of the requirements for the degree of Master of Science in Materials Science.

It is entitled:

Synthesis and Characterization of Crosslinked Polyurethane-Clay Nanocomposites

Student's name: Shirley Peng

This work and its defense approved by:

Committee chair: Jude Iroh, Ph.D.

Committee member: Gregory Beaucage, Ph.D.

Committee member: Rodney Roseman, Ph.D.



14046

Synthesis and Characterization of Crosslinked Polyurethane-Clay Nanocomposites

A thesis submitted to the
Division of Research and Advanced Studies
University of Cincinnati
In partial fulfillment of the requirements for the degree of

Master of Science
2015

In the Department of Mechanical and Materials Engineering
College of Engineering and Applied Science

By
Shirley Peng

B.S. Chemistry, State University of New York at Oswego, 2013

Abstract

A series of crosslinked polyurethane (PU)-clay nanocomposites were synthesized, characterized and evaluated for their corrosion protective properties. The neat PU system was synthesized through the prepolymer route and based on polytetrahydrofuran as the soft segment, methylene diphenyl diisocyanate as the hard segment and glycerin as the crosslinker. PU nanocomposites were prepared via *in-situ* polymerization with concentrations of Cloisite 30B clay varied between 0.25 wt% and 10 wt%. Coatings were prepared by solution casting the neat PU and PU nanocomposites onto Al2024-T3 substrates and curing the specimens thermally.

The chemical composition of neat PU and PU nanocomposites were elucidated using Fourier-Transform infrared (FTIR) spectroscopy. The dispersion and conformation of clay layers was studied using X-ray diffraction (XRD). The effect of clay on the morphology of the PU matrix was examined through scanning electron microscopy (SEM). Rheological studies were performed to understand the influence of clay and temperature on the viscosity of PU. The structure and mechanical properties were characterized using dynamic mechanical spectroscopy (DMS). Surface energy was determined using a dynamic contact angle (DCA) analyzer. Corrosion performance was evaluated using direct current polarization (DCP) and electrochemical impedance spectroscopy (EIS) tests.

FTIR analysis showed that all monomers had reacted during polymerization through the disappearance of hydroxyl and isocyanate peaks. New peaks characteristic of

the carbamate functional group were formed indicating the presence of PU. Diffractograms showed that nanocomposites possessing exfoliated clay is achieved up to concentrations of 1 wt%. Exceeding this limit produced nanocomposites with intercalated and agglomerated structures. SEM images revealed that high concentrations of clay caused phase separation behavior to occur. Rheological measurements demonstrated that clay addition and increase in temperature reduced the overall viscosity of PU. Surface energy analysis showed that increasing the concentration of clay directly increased the hydrophobicity of the coatings. Long-term corrosion studies demonstrated that clay suppressed the rate of corrosion and enhanced the nanocomposites' corrosion resistance. Furthermore, clay improved the barrier properties of PU coatings and significantly extended their lifespan in a corrosive environment.

Acknowledgements

I started on this journey through graduate school two years ago and I am grateful to all the people I met along the way that have guided me to complete this chapter of my life. First and foremost, I would like to express my appreciation and gratitude to my advisor Dr. Jude Iroh for his invaluable insights and support from the time I joined his group in 2013. This thesis would not have been possible without his guidance and motivation. I would also like to thank my thesis committee members Dr. Gregory Beaucage and Dr. Rodney Roseman for taking the time to read my thesis and provide suggestions.

Second, I would like to thank my present group members Nathan Holliday, Anushree Deshpande, Praveen Balasubramani, Patricia Okafor, Yujie Zhang, Xueying He, Wajeeh Marashdeh and Brenton Huxel for their tremendous assistance and friendship. Additionally, I would like to thank the past members Linqian Feng and Aniket Vyas for teaching me how to operate instruments in the lab.

Third I would like to acknowledge Dr. Necati Kaval of the chemistry department, Dr. Pablo Rosales and Dr. Melodie Fickenscher at AMCC, and Fei Yu (Ph.D candidate) for their instrumentation assistance in FTIR, SEM and XRD.

Last but not least, I would like to dedicate this work to my parents for their continuous love, encouragement and generous support throughout my time in graduate school.

Table of Contents

Abstract	ii
Acknowledgements	v
List of Tables	ix
List of Figures	x
Chapter 1: Introduction	1
1.1 Polyurethane.....	1
1.1.1 Polyurethane Synthesis.....	2
1.1.2 Crosslinked Polyurethane.....	4
1.2 Montmorillonite clay.....	5
1.3 Polymer-clay nanocomposites.....	6
1.3.1 Polyurethane-Clay Nanocomposites.....	7
1.4 Corrosion.....	9
1.5 Research Objectives.....	10
Chapter 2: Experimental Procedures	11
2.1 Materials.....	11
2.2 Sample Preparation.....	11
2.2.1 Synthesis of neat polyurethane.....	12
2.2.2 Synthesis of polyurethane-clay nanocomposites.....	12
2.2.3 Preparation of Coatings.....	13
2.3 Characterization.....	14

2.3.1	Fourier-Transform Infrared (FTIR) Spectroscopy.....	14
2.3.2	X-Ray Diffraction (XRD).....	14
2.3.3	Scanning Electron Microscopy (SEM).....	14
2.3.4	Dynamic Contact Angle (DCA).....	15
2.3.5	Brookfield Viscometer.....	16
2.3.6	Dynamic Mechanical Spectroscopy (DMS).....	17
2.3.7	Corrosion Testing.....	18
2.3.7.1	Direct Current Polarization (DCP).....	19
2.3.7.2	Electrochemical Impedance Spectroscopy (EIS).....	19
Chapter 3:	Results and Discussion.....	21
3.1	Structural Characterization.....	21
3.1.1	FTIR analysis of monomers.....	21
3.1.2	FTIR analysis of neat polyurethane.....	21
3.1.2.1	Analysis of crosslinking.....	23
3.1.3	FTIR analysis of C30B.....	24
3.1.4	FTIR analysis of polyurethane-clay nanocomposites.....	24
3.1.5	Clay dispersion.....	25
3.1.6	Morphology.....	27
3.1.7	Surface Properties.....	28
3.2	Rheological Properties.....	29
3.2.1	Effect of clay.....	29
3.2.2	Effect of temperature.....	30

3.3	Dynamic Mechanical Properties.....	32
3.3.1	Presence of crosslinks in neat polyurethane.....	33
3.3.2	Effect of clay on storage modulus.....	33
3.3.3	Effect of clay on $\tan \delta$	36
3.4	Corrosion Evaluation.....	38
3.4.1	Direct current polarization.....	38
3.4.1.1	Tafel plots.....	38
3.4.1.2	E_{corr} and I_{corr}	39
3.4.2	Electrochemical impedance spectroscopy.....	41
3.4.2.1	Nyquist and Bode plots.....	41
3.4.2.2	Coating lifetime.....	45
	Chapter 4: Conclusion.....	47
	Chapter 5: Suggestions and Future Work.....	49
	References.....	50
	Figures.....	60

List of Tables

Table 2.2-1: Sample name with corresponding clay concentration in PU.....	13
Table 2.3-1: Surface tension of the polar and dispersive test liquids.....	16
Table 3.1-1: Assigned characteristic peaks for neat PU.....	22
Table 3.1-2: Effect of clay concentration on hydrogen bonding.....	25
Table 3.1-3: Measured contact angles of neat PU and PU nanocomposites.....	28
Table: 3.2-1: Activation Energies (in KJ/mol) at varied spindle speeds.....	32
Table 3.4-1: Corrosion rate of all coatings over a 60-day salt water exposure period.....	40
Table 3.4-2: Polarization resistance of neat PU and PU nanocomposites over a 60-day period.....	41

List of Figures

Figure 1.1-1: Morphology of thermoplastic PU.....	2
Figure 1.1-2: Urethane formation.....	2
Figure 1.1-3: Side reactions during PU synthesis [5].....	4
Figure 1.2-1: Structure of montmorillonite clay.....	6
Figure 1.3-1: Configurations exhibited by clay in a polymeric matrix.....	7
Figure 1.3-2: Organic modifier for Cloisite 30B clay.....	8
Figure 1.3-3: Chemical and physical interactions between clay and urethane groups.....	8
Figure 2.2-1: Schematic for PU nanocomposite synthesis.....	13
Figure 2.3-1: DCA plot of one full test run.....	15
Figure 2.3-2: Typical plot of storage modulus and $\tan \delta$	17
Figure 2.3-3: Schematic setup for electrochemical corrosion tests.....	18
Figure 2.3-4: Typical Tafel plot.....	19
Figure 2.3-5: Typical Nyquist plot.....	20
Figure 2.3-6: Typical Bode plot.....	20
Figure 3.1-1: FTIR spectra of (a) PTHF, (b) glycerin, (c) MDI.....	60
Figure 3.1-2: FTIR spectrum of neat PU.....	60
Figure 3.1-3: Labeled urethane bonds with their correlating wavenumbers.....	22
Figure 3.1-4: FTIR of PU crosslinked with varied concentrations of glycerin at low wavenumbers.....	61
Figure 3.1-5: FTIR of PU crosslinked with varied concentrations of glycerin at high wavenumbers.....	61

Figure 3.1-6: Effect of glycerin concentration on hard/crosslinking segment C-O peak.....	62
Figure 3.1-7: Effect of glycerin concentration on hard/crosslinking segment C=O (H-bonded) peak.....	62
Figure 3.1-8: Effect of glycerin concentration on urethane N-H peak.....	63
Figure 3.1-9: FTIR spectra of Cloisite 30B clay.....	64
Figure 3.1-10: FTIR spectra of PU nanocomposites with clay loading at (a) 0.25 wt%, (b) 0.5 wt%, (c) 1 wt%, (d) 2 wt%, (e) 5 wt% and (f) 10 wt%.....	65
Figure 3.1-11: Close-up of organic moiety clay peak at 461 cm^{-1}	65
Figure 3.1-12: Deconvolution of 1730 cm^{-1} (free C=O group) and 1709 cm^{-1} (H-bonded C=O) peaks.....	66
Figure 3.1-13: Diffractogram of Cloisite 30B clay.....	67
Figure 3.1-14: Diffractogram of (a) neat PU, (b) PU-C025, (c) PU-C05 and (d) PU-C1.....	68
Figure 3.1-15: Diffractogram of (a) PU-C2 (b) PU-C5 and (c) PU-C10.....	68
Figure 3.1-16: SEM image of C30B powder at (a) 1500x and (b) 20kx.....	69
Figure 3.1-17: Cross-sectional SEM image of neat PU at (a) 1500x and (b) 10kx.....	70
Figure 3.1-18: Cross-sectional SEM images of PU-C025 at (a) 1500x and (b) 10kx.....	71
Figure 3.1-19: Cross-sectional SEM images of PU-C05 at (a) 1500x and (b) 10kx.....	72
Figure 3.1-20: Cross-sectional SEM images of PU-C1 at (a) 1500x and (b) 10kx.....	73
Figure 3.1-21: Cross-sectional SEM images of PU-C2 at (a) 1500x and (b) 10kx.....	74
Figure 3.1-22: Cross-sectional SEM images of PU-C5 at (a) 1500x and (b) 20kx.....	75
Figure 3.1-23: Cross-sectional SEM images of PU-C10 at (a) 1500x and (b) 12kx.....	76
Figure 3.1-24: Surface energy of PU as clay concentration is increased.....	77

Figure 3.2-1: Effect of clay and shear rate on the viscosity of PU at 25°C.....	78
Figure 3.2-2: Viscosity of neat PU as a function of temperature and shear rate.....	79
Figure 3.2-3: Viscosity of PU-C025 as a function of temperature and shear rate.....	79
Figure 3.2-4: Viscosity of PU-C05 as a function of temperature and shear rate.....	80
Figure 3.2-5: Viscosity of PU-C1 as a function of temperature and shear rate.....	80
Figure 3.2-6: Viscosity of PU-C2 as a function of temperature and shear rate.....	81
Figure 3.2-7: Viscosity of PU-C5 as a function of temperature and shear rate.....	81
Figure 3.2-8: Viscosity of PU-C10 as a function of temperature and shear rate.....	82
Figure 3.2-9: Change in viscosity at constant shear rate as a function of temperature.....	83
Figure 3.3-1: Storage modulus curve of PU synthesized with glycerin (crosslinked) and PU synthesized with butanediol (linear).....	84
Figure 3.3-2: Tan δ curve of PU synthesized with glycerin (crosslinked) and PU synthesized with butanediol (linear).....	84
Figure 3.3-3: Storage modulus of neat PU and PU nanocomposites.....	85
Figure 3.3-4: Change in E_G at -90°C as a function of clay concentration.....	86
Figure 3.3-5: Change in E_R at 40°C as a function of clay concentration.....	86
Figure 3.3-6: Modulus enhancement as a function of clay volume fraction.....	87
Figure 3.3-7: Comparison of experimental modulus with the Halpin-Tsai model.....	88
Figure 3.3-8: Tan δ of neat PU and PU nanocomposites.....	89
Figure 3.3-9: Glass-transition temperatures as a function of clay concentration.....	89
Figure 3.3-10: Damping properties as a function of clay concentration.....	90
Figure 3.4-1: Tafel polarization curve of bare aluminum alloy.....	91

Figure 3.4-2: Tafel polarization curve of neat PU and PU nanocomposites after 7 days exposure.....	91
Figure 3.4-3 Tafel polarization curve of neat PU and PU nanocomposites after 14 days exposure.....	92
Figure 3.4-4 Tafel polarization curve of neat PU and PU nanocomposites after 30 days exposure.....	92
Figure 3.4-5: Tafel polarization curve of neat PU and PU nanocomposites after 60 days exposure.....	93
Figure 3.4-6: E_{corr} of neat PU and PU nanocomposites over 60 days exposure to salt water.....	94
Figure 3.4-7: I_{corr} of neat PU and PU nanocomposites over 60 days exposure to salt water.....	94
Figure 3.4-8: Nyquist plot of bare aluminum alloy.....	95
Figure 3.4-9: Nyquist plot of (a) neat PU, PU-C025, PU-C05, PU-C1 (b) PU-C2, PU-C5 and PU-C10 after 7 days exposure to salt water.....	96
Figure 3.4-10: Nyquist plot of (a) neat PU, PU-C025, PU-C05, PU-C1 (b) PU-C2, PU-C5 PU-C10 and (c) close-up of corroded PU-C5 after 14 days exposure to salt water.....	97
Figure 3.4-11: Nyquist plot of (a) corroded PU-C10 close-up and (b) non-corroded PU nanocomposites after 30 days exposure.....	99
Figure 3.4-12: Nyquist plot of (a) non-corroded PU nanocomposites and (b) close-up of corroded PU-C2 after 60 days exposure to salt water.....	100
Figure 3.4-13: Equivalent circuit for coating with one-time constant.....	42
Figure 3.4-14: Equivalent circuit for coating with two time-constants.....	43
Figure 3.4-15: Bode plot of bare aluminum alloy.....	101
Figure 3.4-16: Bode plot of PU containing 0 wt% clay over 60-day exposure to salt water.....	101
Figure 3.4-17: Bode plot of PU containing 0.25 wt% clay over 60-day exposure to salt water.....	102

Figure 3.4-18: Bode plot of PU containing 0.5 wt% clay over 60-day exposure to salt water.....	102
Figure 3.4-19: Bode plot of PU containing 1 wt% clay over 60-day exposure to salt water.....	103
Figure 3.4-20: Bode plot of PU containing 2 wt% clay over 60-day exposure to salt water.....	103
Figure 3.4-21: Bode plot of PU containing 5 wt% clay over 60-day exposure to salt water.....	104
Figure 3.4-22: Bode plot of PU containing 10 wt% clay over 60-day exposure to salt water.....	104
Figure 3.4-23: Change in initial impedance as exposure time is increased.....	105
Figure 3.4-24: Predicted coating lifetime of neat PU and PU nanocomposites.....	106

Chapter 1: Introduction

1.1 Polyurethane

The development of polyurethane (PU) dates back to the 1930's, when Dr. Otto Bayer first formulated the polymer as an attempt to circumvent the patents placed on polyamides and polyesters [1, 2]. The material was produced through a polyaddition reaction between diisocyanate and butanediol in which soft fibers were obtained [2]. It wasn't until the beginning of World War II that PU would become a replacement for rubber. Throughout the war, PU was used to manufacture gas resistant garments, airplane finishes and protective coatings. By the mid-50s, they had made their way into applications such as adhesives and rigid foams, and gradually into our daily lives [1-3].

For the past few decades, PUs have been extensively investigated due to their versatility and desirable properties such as good abrasion strength, excellent flexibility and high impact resilience [4-7]. These properties are influenced by their unique morphology consisting of a soft and hard segment [8]. The soft phase is composed of a flexible polyol (e.g. polyether, polyester) that gives the polymer elastomeric properties whereas the hard phase is based on polyisocyanates (e.g. diisocyanates, triisocyanates) and a short chain extender (e.g. glycol) providing rigidity [9, 10]. An illustration of their broad structure can be observed in figure 1.1-1.

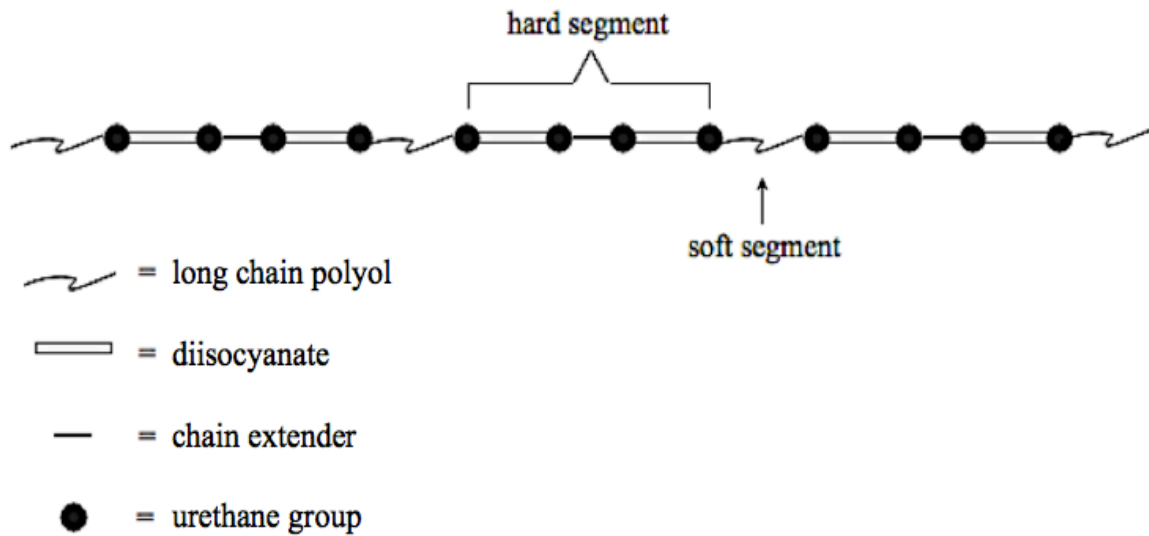


Figure 1.1-1: Morphology of thermoplastic PU

Additionally, the chemistry of PU can be easily tailored by selecting monomers with certain structures (e.g. aliphatic, aromatic) to obtain desired final properties that meet various demands and end applications [11, 12]. As of today, PUs have increasingly been employed in the manufacturing of footwear components, insulation materials, synthetic leather and coatings [13, 14].

1.1.1 Polyurethane Synthesis

PU is characterized by the formation of a carbamate (urethane) functional group as observed in figure 1.1-2.

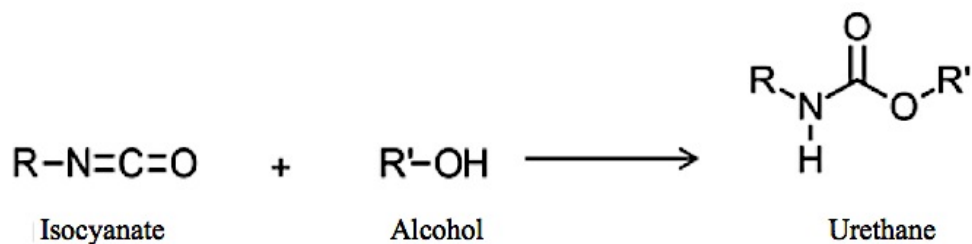


Figure 1.1-2: Urethane formation

PU's can be synthesized either through the one-shot method or the prepolymer (two-shot) method. The one-shot process requires the polyol, polyisocyanate, chain extenders and any other additives such as fillers, to be simultaneously blended together in one reaction pot. After some time, the reaction mixture is cured in either a mold or processed in another manner. This technique allows the isocyanate to react freely with any monomer containing a reactive hydroxyl group. Although the procedure is relatively simple, this process allows no control over the final structure of PU [15, 16].

The two-shot process involves a two-step sequence that allows greater control and uniformity over the final structure of PU. The first step involves the reaction between the polyol and polyisocyanate (in excess) to yield an isocyanate (NCO)-terminated prepolymer. In the second step, the prepolymer reacts with a chain extender in order to link together the NCO-terminated prepolymers to form a high molecular weight PU. Thereafter, the reaction is cured to obtain PU [17-19].

Because isocyanate groups are highly reactive, traces of water can initiate side reactions to occur during urethane group formation. Additionally reaction temperature and ratio of starting materials are another cause. The most common side products include urea, biuret, allophanate and isocyanurate, as observed in figure 1.1-3. [20-24].

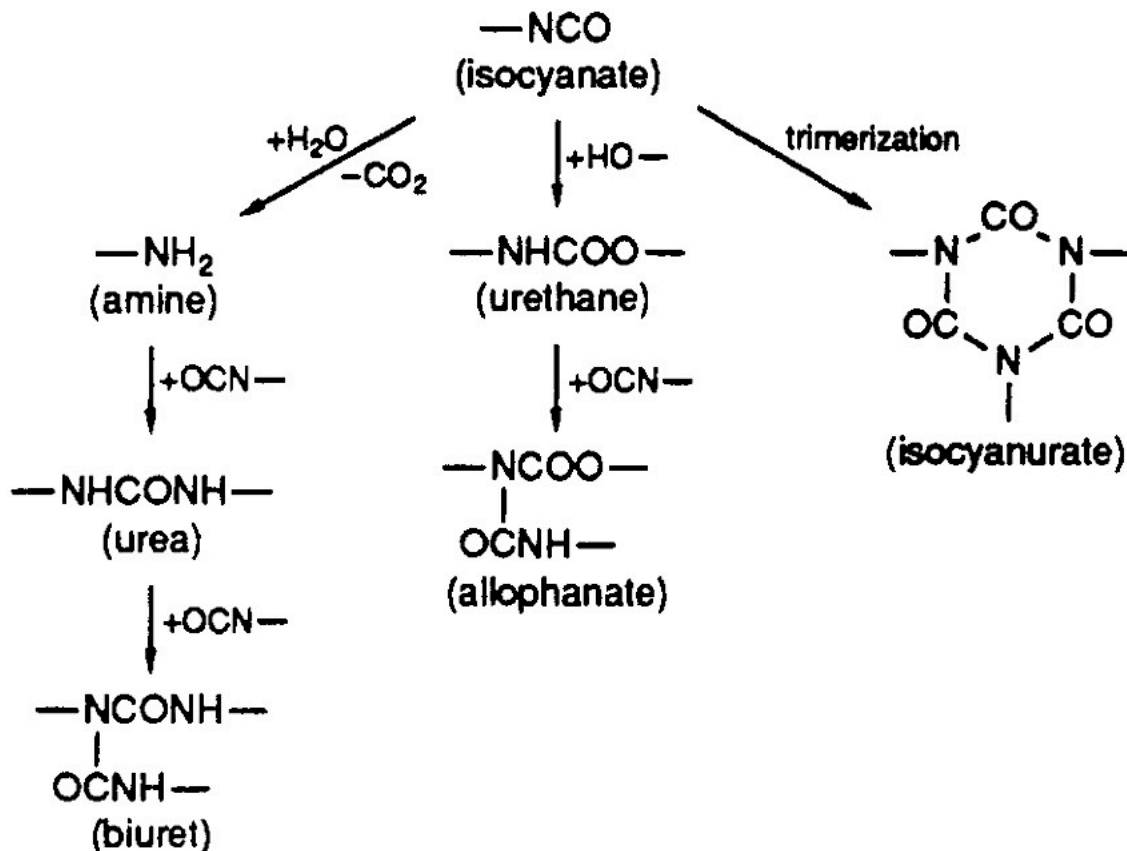


Figure 1.1-3: Side reactions during PU synthesis [14]

Usually, the presence of these compounds are undesirable as it decreases the amount of isocyanate groups available to react with the hydroxyl-terminated monomers. In some cases, these reactions are intentional as this process introduces additional crosslinks into the PU structure [20, 25].

1.1.2 Crosslinked Polyurethane

The mechanism of crosslinking PU has been employed to control one of the material's many properties [26]. Because the soft and hard domains of PU are thermodynamically incompatible, this yields micro-phase separation to occur in the hard

segment through intermolecular hydrogen bonding [27-30]. Additionally, the formation of a two-phase morphology can be affected by the molecular weight of the soft segment, the quantity of the hard segment and the choice of chain extender used [31]. To reduce the occurrence of this phenomenon, chemical crosslinks can be introduced into the system through tri-functional chain extenders [32].

Prior research studies have utilized hydroxyl-terminated crosslinkers such as trimethylol propane (TMP) [32, 33], trimethylol propoxylate [34] and polyether triol [35] to form crosslinked PU. Also, amine-terminated crosslinkers such as methylene-bis-*ortho*-chloroaniline (MOCA) [36] have been widely applied to form urea networks.

A majority of crosslinked PUs to date have found applications as shape memory polymers and foams [32, 33, 37]. However, crosslinked PUs are also widely utilized as protective and decorative coatings [38].

1.2 Montmorillonite Clay

Montmorillonite (MMT) clay has been one of the most widely investigated reinforcing agents due to their high aspect ratio, rich intercalation chemistry and relatively low cost [39, 40]. In its natural state, MMT is comprised of stacked tetrahedral and octahedral aluminosilicate sheets with cations residing between the galleries of each layer (figure 1.2-1). When the material is present in aggregate form, the size ranges between 0.1-10 μm . Each individual silicate platelet, which makes up the layered clay structure, are approximately 1.0 nm in thickness [41, 42]. Because polymer matrices are

incompatible with Na^+ or Ca^{2+} ions, organic cation surfactants are often added to counteract this hydrophilic surface and increase their organophilicity [40, 43, 44].

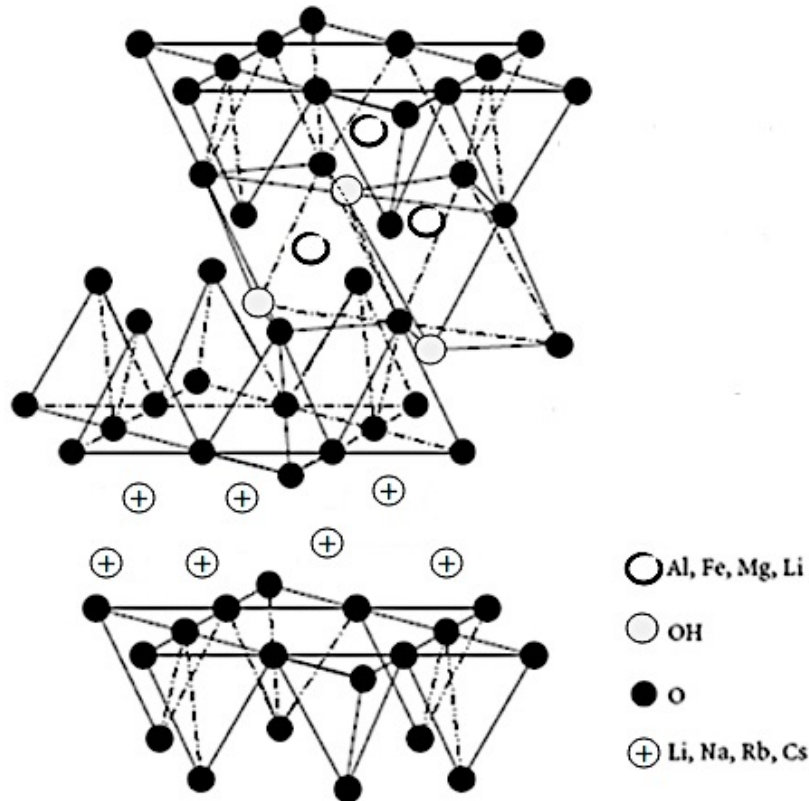


Figure 1.2-1: Structure of montmorillonite clay

1.3 Polymer-Clay Nanocomposites

Nanocomposites are classified as composites possessing at least one phase showing dimensions in the nanometer range [45]. MMT clay has been commonly used as a nanofiller for polymeric matrices. Incorporation of these fillers in low quantities can elicit significant improvements in the polymer's resistance to chemicals, reduce gas permeability and increase thermal stability [46-49]. Additionally these improvements are correlated with how the silicate layers are dispersed in the matrix [40, 50, 51].

When clay layers are incompatible with the polymer matrix, the platelets will tend to aggregate and result in conventional form. When the polarities of two materials are similar, clay layers can become intercalated or exfoliated. Intercalation involves the insertion of polymer chains within the gallery of the clay contributing to expansion of the interlayer spacing. Meanwhile, exfoliation involves platelets to be fully separated and delaminated [40, 52].

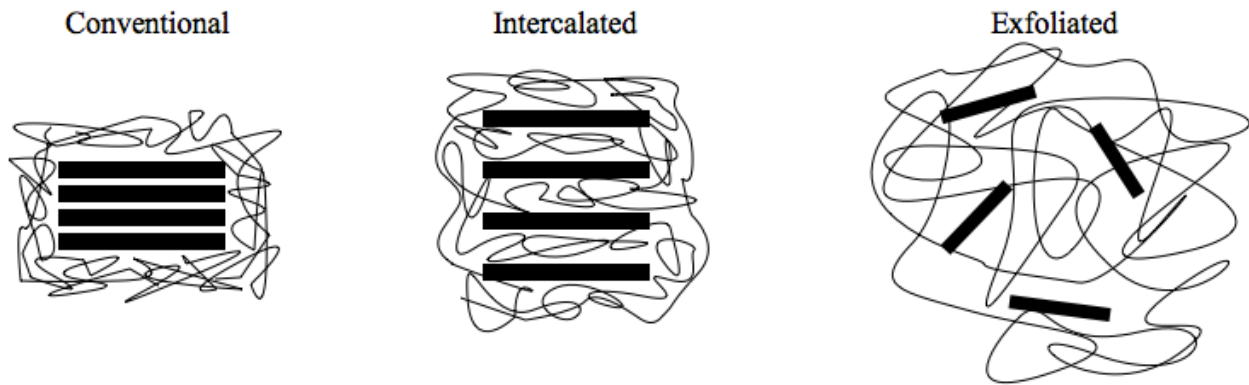


Figure 1.3-1: Configurations exhibited by clay in a polymeric matrix

1.3.1 Polyurethane-Clay nanocomposites

Clay has been extensively used in PU to improve upon its thermal stability and barrier properties [53, 54]. The pioneering work in PU-clay nanocomposites was first reported by Wang and Pinnavaia [55] in which the researchers demonstrated that PU-clay nanocomposites exhibited significant improvement in tensile strength and strain-at-break. Thereafter, a number of researchers began to report studies on PU-clay nanocomposites, utilizing different types of MMT clay and investigating their synergistic properties [56-59].

Of the commercially available clay fillers, Cloisite 30B (C30B) has been shown to have the best compatibility with PU [60, 61]. C30B is a MMT clay modified with a quaternary ammonium salt. As observed in figure 1.2-2, the organic surfactant possesses two hydroxyl groups, a methyl group and a tallow that is comprised of ~65% C-18, ~30% C-16 and ~5% C-14 [62, 63].

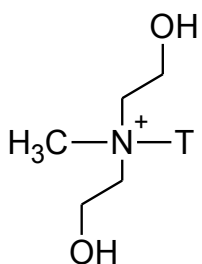


Figure 1.3-2: Organic modifier for Cloisite 30B clay

The ability for C30B to achieve good dispersion in PU arises from its organic modifier's hydroxyl-capped quaternary ammonium groups, which can interact chemically with isocyanate groups and physically hydrogen bond with urethane groups in the matrix (figure 1.3-3) [36, 64].

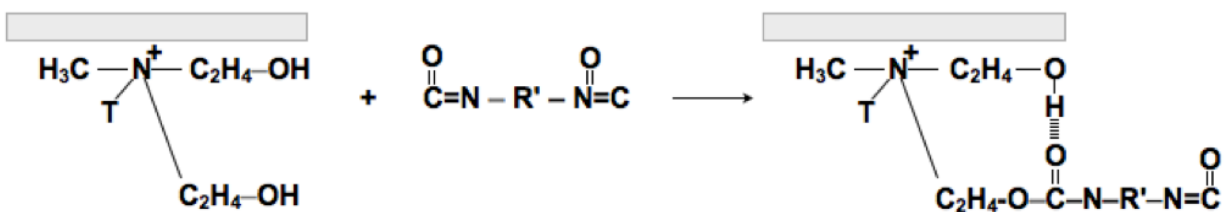


Figure 1.3-3: Chemical and physical interactions between clay and urethane groups

Prior researchers have concluded that well-dispersed clay led to better overall properties in PU. Pizzatto *et al.* [65], reported that dispersed C30B contributed to better

mechanical properties in PU than agglomerated clay. Kaushik *et al.*[66], reported that exfoliated C30B inhibited water diffusivity and reduced water absorption. Furthermore, Ashhari and authors [67] showed that dispersed clay prepared through sonication improved the anticorrosive properties of PU. The commonality between these studies is that the focus is on the reinforcement of thermoplastic polyurethanes (TPU). Few studies have been geared toward studying the properties of crosslinked polyurethane-clay nanocomposites and therefore in this research, we will try to further exploit this area.

1.4 Corrosion

Over the past 30 years, the annual cost of corrosion in the U.S. is estimated to amount to over \$200 billion, with a majority of the cost associated with utilities, transportation and infrastructure [68]. From the point of view on safety, the detrimental effects of corrosion such as fatigue cracking and structure failure can have harmful consequences for humans and the surrounding environment [69, 70] The process of corrosion occurs when electrons are stripped off the metal through anodic oxidation then consumed in cathodic reduction. This leaves resulting cations on the metal's surface that is readily available to become corrosion products. Therefore the basic requirements for corrosion to initiate are an anode, cathode, an electrolyte and an oxidizing species [71].

Many studies have focused on using organic coatings to act as a physical barrier to protect metallic surfaces from corrosive environments [72-75]. This is because organic matrices can maintain electrical resistivity across the entire coating thickness [76]. However, all polymeric coatings are prone to oxygen and water permeation and therefore

many types of fillers such as MMT clay have been employed to increase the barrier properties of these materials [77-83]. In this work, our prepared crosslinked-PU nanocomposite systems will be evaluated as a potential corrosion protective coating.

1.5 Research Objectives

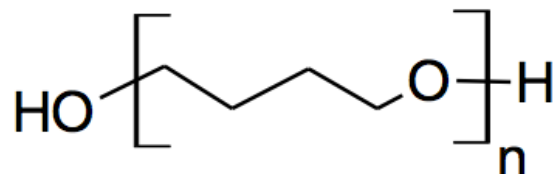
The three aims of this research is to develop and characterize a novel PU-clay nanocomposite system, and evaluate its application as an anticorrosion coating.

- The PU will be synthesized with crosslinked structure using glycerin as the tri-functional crosslinking agent. PU nanocomposites will be prepared through *in-situ* polymerization in which sonication will be applied to the solution to ensure that clay platelets are well dispersed within the nanocomposite.
- The concentration of C30B clay will be varied from low to high weight percentages in the system to study how clay influences the different properties of PU.
- The effect of clay dispersion and clay concentration will be correlated to the corrosion performance of each system. This will assist with determining the optimal amount of clay that will achieve coatings with the best resistivity against corrosion.

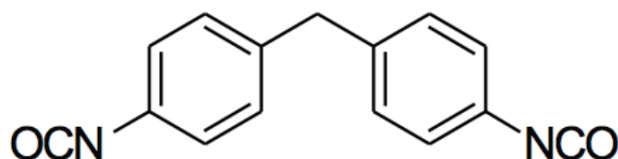
Chapter 2: Experimental Procedures

2.1 Materials

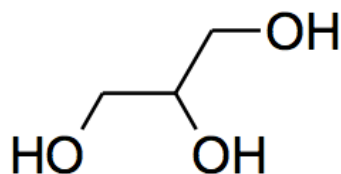
- Polytetrahydrofuran (Sigma Aldrich, Mn=1000 g/mol)



- 4, 4'-Methylenebis(phenyl isocyanate) (Sigma Aldrich)



- Certified A.C.S. grade glycerin (Fisher Scientific)



- N,N-Dimethylformamide (Sigma Aldrich)
- Cloisite 30BTM (Southern Clay Products)

2.2 Sample Preparation

Prior to synthesis, C30B clay was dried in the oven for 24h at 100°C to remove any water or absorbed moisture. Other materials were used as received from their respective suppliers.

2.2.1 Synthesis of neat polyurethane

In a three-neck round bottom flask, 10 mmol of polytetrahydrofuran (PTHF) was dissolved in 100 mL N,N-Dimethylformamide (DMF) and heated to 60°C in a water bath under nitrogen atmosphere. Twenty mmol of 4, 4'-Methylenebis(phenyl isocyanate) (MDI) was added to the flask and both monomers were allowed to react for 1h to form a NCO-terminated prepolymer. The solution was maintained at 60°C to which 6 mmol of glycerin was added dropwise and stirred for 10 min. Afterwards, the mixture was removed from heat and stirred for an additional 30 min at room temperature to obtain PU in branched form. The whole solution was poured into a Teflon mold and the solvent removed at 70°C for 24h to fully cure and crosslink the material.

2.2.2 Synthesis of polyurethane-clay nanocomposites

PU nanocomposites were prepared via *in-situ* polymerization. PTHF was dissolved in a three-neck flask containing 100 mL DMF at room temperature. Different quantities of clay (Table 2.2-1) were added to the solution under rapid stirring for 2h followed by sonication for 1h to completely disperse clay layers. The mixture was then heated to 60°C under nitrogen atmosphere where polymerization was carried out in the same manner as the neat PU. The schematic of this mechanism can be observed in figure 2.2-1.

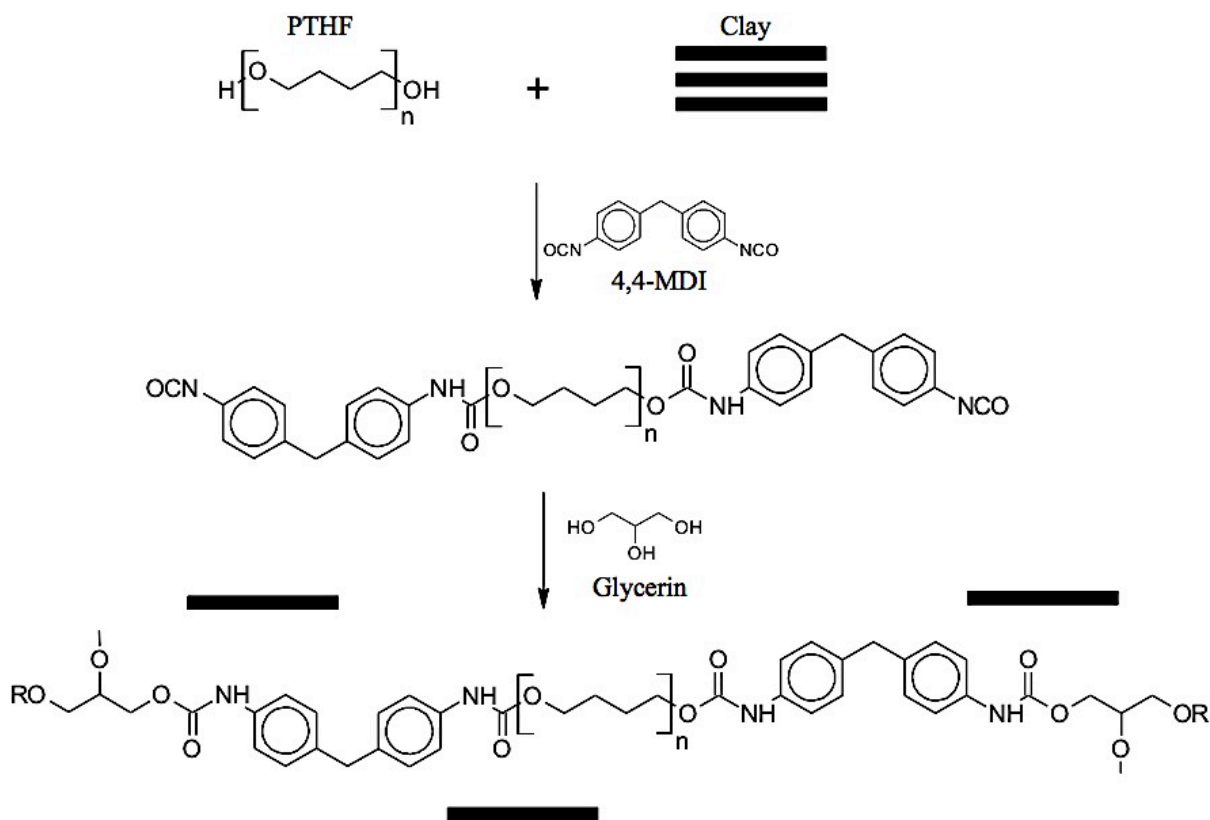


Figure 2.2-1: Schematic for PU nanocomposite synthesis

Table 2.2-1: Sample name with corresponding clay concentration in PU

Sample Name	Clay Concentration (wt%)
Neat PU	0
PU-C025	0.25
PU-C05	0.5
PU-C1	1
PU-C2	2
PU-C5	5
PU-C10	10

2.2.3 Preparation of Coatings

Neat PU and PU nanocomposite solutions were casted onto 1'' x 4'' x 1/8'' Al2024-T3 alloys using the solution drop technique. The coatings were cured in the oven for 10h

at 70°C to achieve films with thickness of approximately 0.1 mm. The final coatings had a smooth surface finish with no voids or cracks present.

2.3 Characterization

2.3.1 Fourier-Transform Infrared (FTIR) Spectroscopy

FTIR was used to elucidate the chemical composition of neat PU and PU nanocomposites. A total of 32 scans were collected using a Thermo Scientific Nicolet 6700 spectrometer in the wavenumber range between 4000 cm⁻¹ and 400 cm⁻¹.

2.3.2 X-Ray Diffraction (XRD)

XRD was performed on a PANalytical X'Pert Pro Diffractometer with Cu-K α radiation wavelength at 0.154 nm. The samples were evaluated between 2° and 7°. Bragg's Law (equation 1) [84] was applied to calculate d-spacing between clay layers.

$$d = \frac{n\lambda}{2\sin\theta} \quad (1)$$

The parameter n is a constant (equal to 1), λ is the wavelength of radiation and θ is the angle of diffraction.

2.3.3 Scanning Electron Microscopy (SEM)

SEM was performed using a Philips FEI XL 30 ESEM-FEG operating at 30kV. The samples were prepared on carbon-taped aluminum stubs and sputter coated with Au-Pd. Images were captured using Scandium software and analyzed using ImageJ.

2.3.4 Dynamic Contact Angle (DCA)

The contact angle freestanding films was measured through the Wilhelmy plate method performed on a Thermo CAHN dynamic contact angle analyzer (model DCA-322). For each sample, two sets of rectangular freestanding films were prepared with perimeters ranging between 15 mm to 18 mm. The first set of samples were submerged in distilled water (polar solvent) and the second set of samples were submerged in hexadecane (dispersive solvent), both at a stage speed of 50.8 micron/s. This process produced a plot showing the advancing and receding angles between the solid and liquid phase, from which contact angle was extrapolated from the advancing angle (figure 2.3-1).

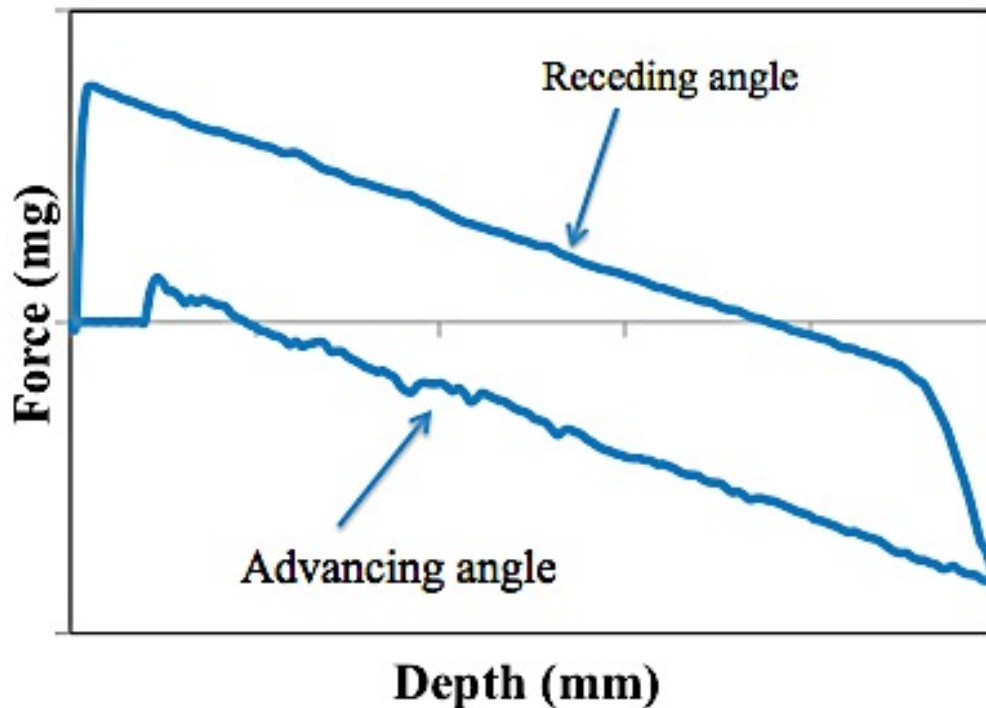


Figure 2.3-1: Typical DCA plot of one full test run

The surface energy of the films were calculated through the Owens-Wendt geometric means approach (equation 2) [86]:

$$(1 + \cos\theta)\gamma_{LV} = 2\sqrt{(\gamma_{SV}^D \gamma_{LV}^D)} + 2\sqrt{(\gamma_{SV}^P \gamma_{LV}^P)} \quad (2)$$

Where θ is the contact angle, γ_{LV} is the surface tension at the liquid-vapor interface, γ_{SV}^D is the surface tension of the dispersive component at the solid-vapor interface, γ_{LV}^D is the surface tension of the dispersive component at the liquid-vapor interface, γ_{SV}^P is surface tension of the polar component at the solid-vapor interface and γ_{LV}^P is the surface tension of the polar component at the liquid-vapor interface. The surface tensions of the water and hexadecane test liquids are reported in Table 2.3-1.

Table 2.3-1: Surface tension of the polar and dispersive test liquids [59]

Test Liquid	Polar (γ_{LV}^P)	Dispersive (γ_{LV}^D)	Surface Tension (dynes/cm)
Distilled Water	50.3	22.5	72.8
Hexadecane	0.00	27.6	27.6

2.3.5 Brookfield Viscometer

Rheological measurements were acquired using a rotational Brookfield DV-I+ Viscometer. A container diameter of 18.66 mm and S31 spindle with diameter of 5.88 mm was used. Viscosity measurements were carried out at spindle speeds between 5 and 100 rpm and were correlated with shear rate using equations 3 and 4 [85]:

$$\omega \left(\frac{\text{rad}}{\text{s}} \right) = \frac{2\pi(\text{speed})}{60} \quad (3)$$

$$S \text{ (s}^{-1}\text{)} = \frac{2\omega R_c^2}{(R_c^2 - R_b^2)} \quad (4)$$

Where ω , R_c and R_b represents the conversion factor for angular velocity, container radius and spindle radius, respectively. All samples were analyzed in their branched state.

2.3.6 Dynamic Mechanical Spectroscopy (DMS)

DMS was performed using Seiko Instruments SII EXSTAR 6000 spectrometer in tensile mode. Freestanding films were prepared with length of 20 mm, width ranging between 8 mm and 9 mm, and thickness between 0.5 mm and 0.7 mm. Samples were analyzed from -100°C to 50°C at a heating rate at $5^\circ\text{C}/\text{min}$ and constant frequency of 1Hz. This generated a plot showing storage modulus and $\tan \delta$ curve (figure 2.3-2). Each sample was analyzed at least three times in order to obtain error from the standard deviation of the combined values.

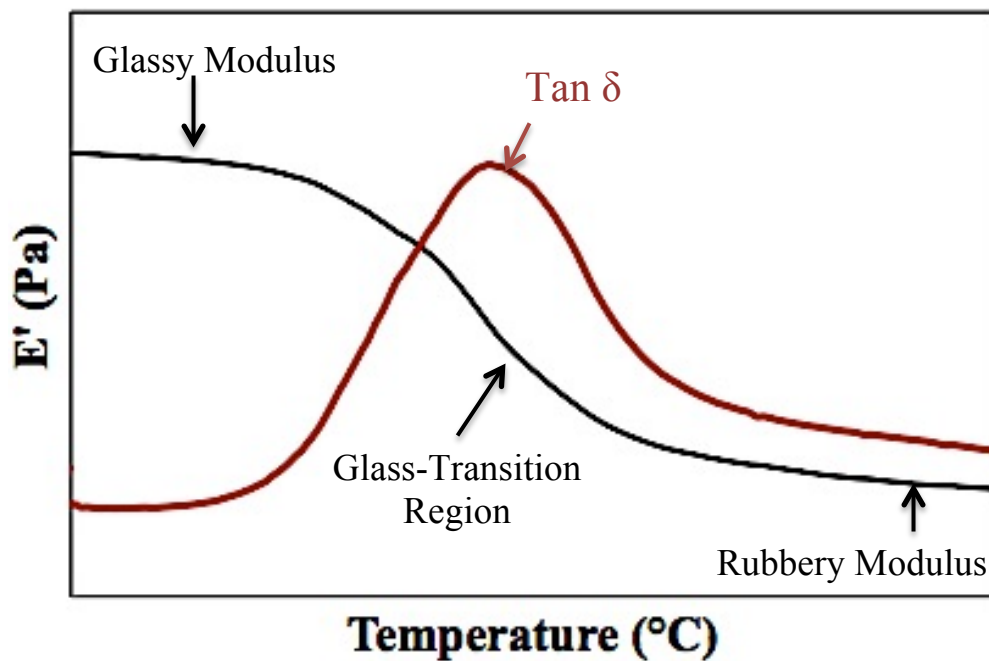


Figure 2.3-2: Typical plot of storage modulus and $\tan \delta$

2.3.7 Corrosion Testing

Direct current polarization and electrochemical impedance spectroscopy were both employed to evaluate the corrosion properties and performance of neat PU and PU nanocomposite coatings. Test methods were carried out using GAMRY Instruments Reference 3000 Potentiostat. Samples were prepared by securing a glass cell to the coating using a clamp. The cell was filled with 3.5 wt% sodium chloride (NaCl) solution to mimic corrosive sea water conditions and covered a surface area of 2.88 cm² on the surface of the coatings. A saturated calomel electrode (SCE) containing KCl solution and a graphite rod were used as the reference electrode and counter electrode, respectively. The setup for both techniques is illustrated in figure 2.3-3.

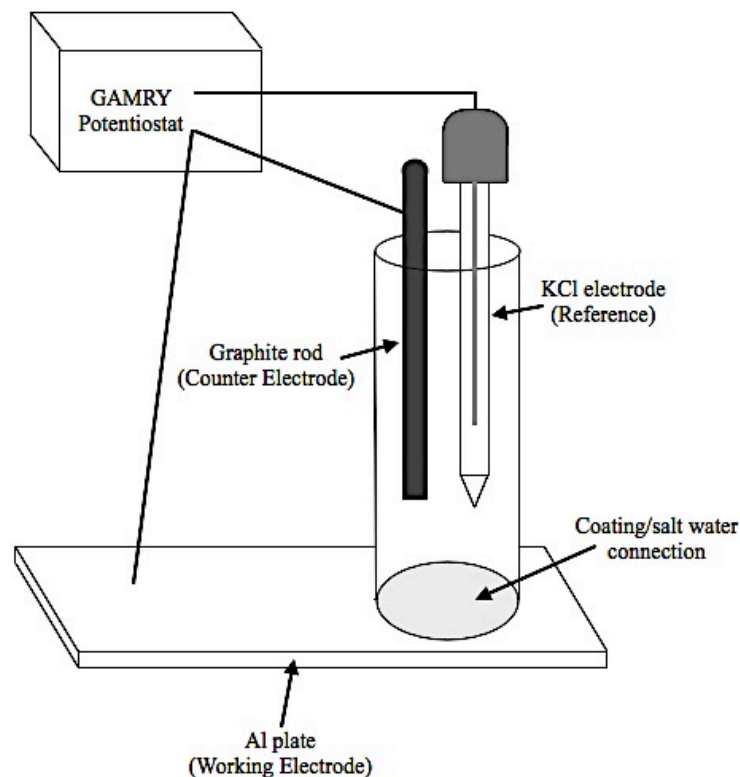


Figure 2.3-3: Schematic setup for electrochemical corrosion tests

2.3.7.1 Direct Current Polarization (DCP)

DCP was carried out to evaluate the corrosion resistance and corrosion rate of all coatings. Tafel plots were generated by applying a current potential from -0.3 V to +0.3 V at a scan rate of 2 mV/s. An example of the Tafel plot can be observed in figure 2.3-4.

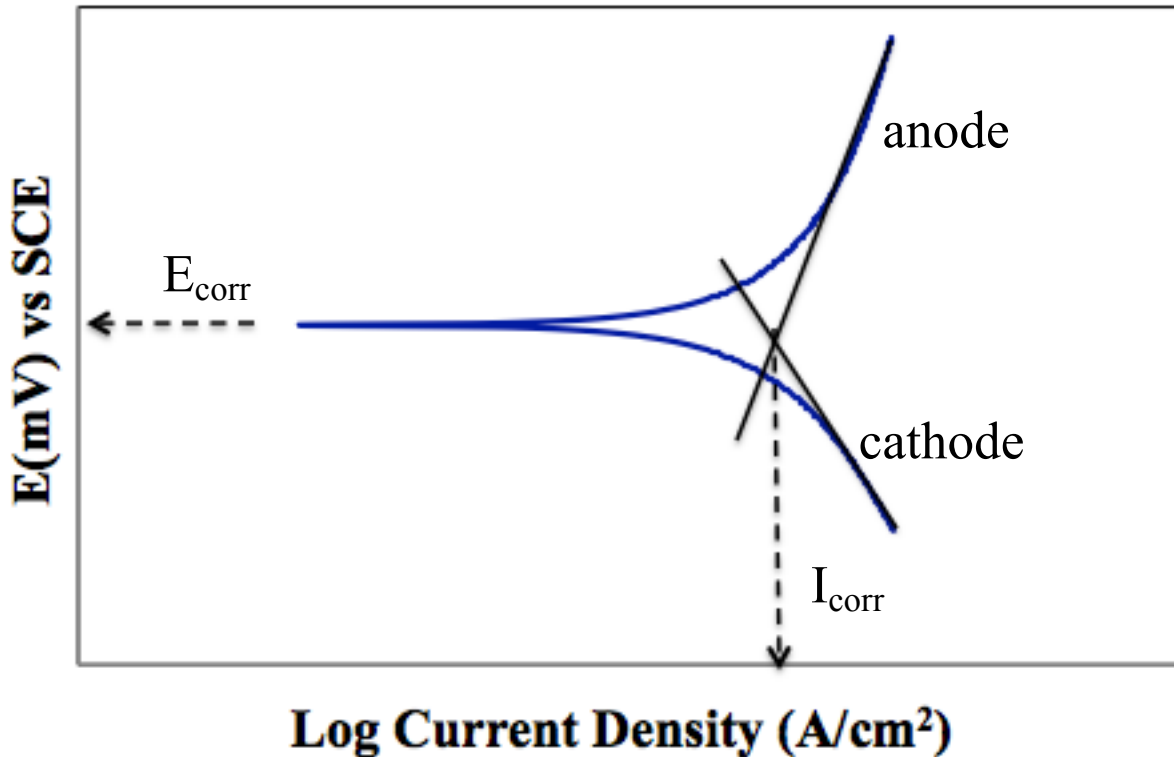


Figure 2.3-4: Typical Tafel plot

2.3.7.2 Electrochemical Impedance Spectroscopy (EIS)

EIS evaluated the barrier properties and corrosion performance of the coatings. Potentiostatic curves were obtained over a frequency range from 10⁶ to 10⁻² Hz with AC voltage amplitude at +10 V. This method generated a Nyquist plot (figure 2.3-5) showing imaginary impedance versus real impedance as a function of frequency. Another

representation of this plot is the Bode plot (figure 2.3-6), which presents impedance versus frequency.

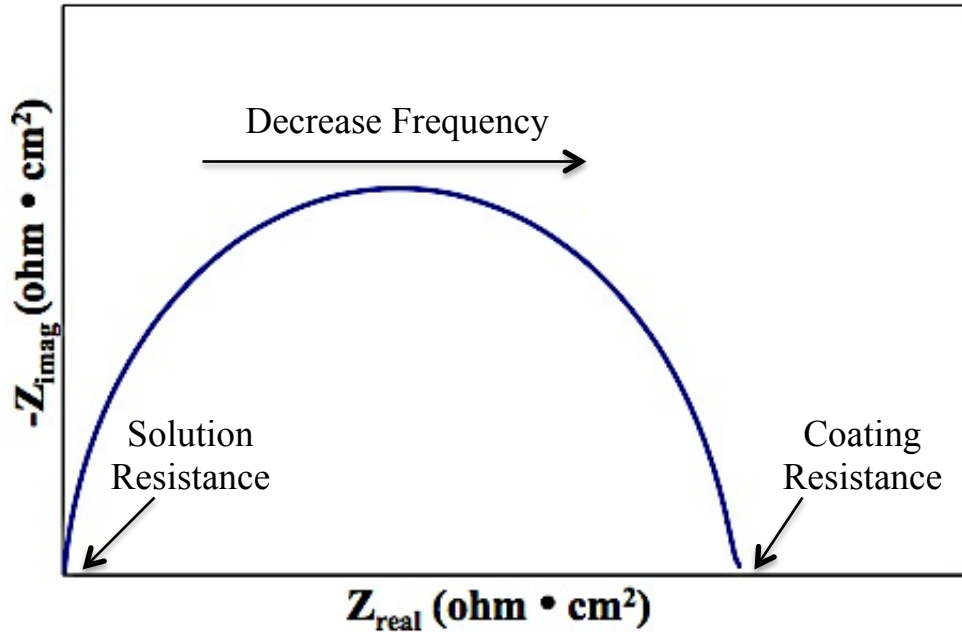


Figure 2.3-5: Typical Nyquist Plot

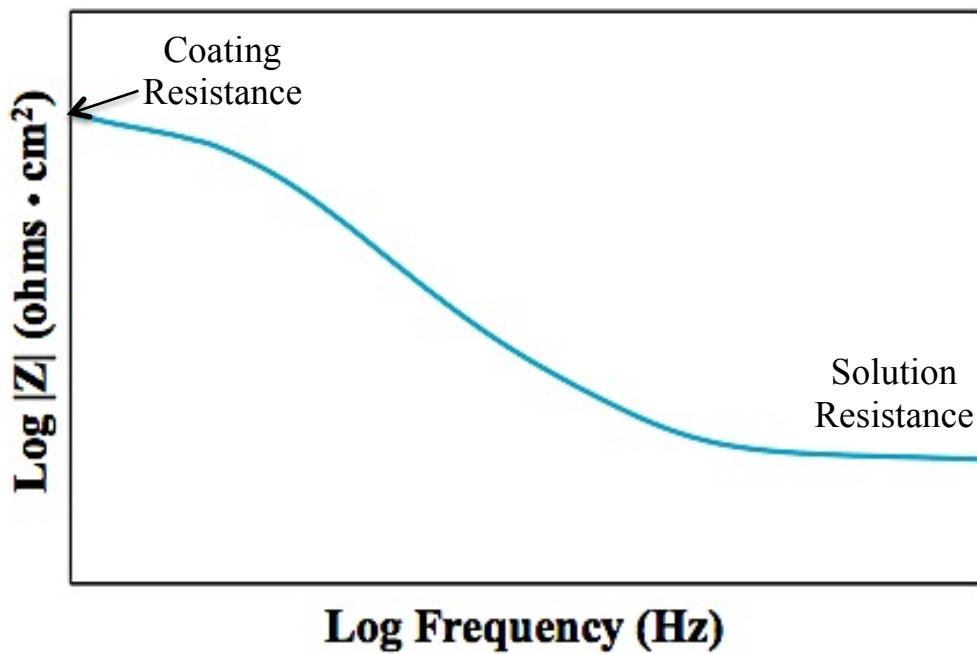


Figure 2.3-6: Typical Bode Plot

Chapter 3: Results and Discussion

3.1 Structural Characterization

3.1.1 FTIR analysis of monomers

Figure 3.1-1(a-c) shows the IR spectra of PTHF, glycerin and MDI. The reactive hydroxyl groups (-OH) in the PTHF and glycerin spectra (figures 3.1-1a and 3.1-1b) are observed as broad vibrations at 3453 cm^{-1} and 3457 cm^{-1} , respectively. In the PTHF spectrum, CH_2 and CH groups can be observed at 2797 cm^{-1} , 2861 cm^{-1} and 2941 cm^{-1} . Additionally, the sharp peak at 1113 cm^{-1} represents the C-O ether stretch. In the glycerin spectrum, similar peaks were observed. The hydrocarbon groups were present at 2881 cm^{-1} and 2936 cm^{-1} , and the ether stretch was present at 1043 cm^{-1} . In the MDI spectrum (figure 3.1-1c), the highly reactive isocyanate group (-NCO) can be observed at 2281 cm^{-1} . At low wavenumbers, the multitude of peaks were attributed to hydrocarbon bonds.

3.1.2 FTIR analysis of neat polyurethane

Figure 3.1-2 shows the IR spectrum of neat PU. It is observed that isocyanate and hydroxyl groups were not present in the spectrum demonstrating that all monomers had fully reacted during polymerization/curing. In turn, new peaks appeared at 1223 cm^{-1} , 1730 cm^{-1} and 3309 cm^{-1} , which are attributed to C-O, C=O and N-H stretches, confirming the formation of urethane groups. The set of three peaks situated around the 2800 cm^{-1} region are attributed to CH_2 and CH bonds from the PTHF monomer. Additionally, the sharp peak at 1111 cm^{-1} is from the PTHF's ether stretch. A minor peak

can be observed around 1644 cm^{-1} , which is attributed to C=O stretching from urea. The formation of urea was due to some absorbed moisture in the reaction mixture and during the curing process.

Further assigned characteristic peaks of neat PU are reported in Table 3.1-1 and were confirmed with those reported by Hiltz and Szabo [87]. Additionally, the stretching of bonds at wavenumbers reported between 1072 cm^{-1} and 1538 cm^{-1} can be viewed in figure 3.1-3, to reduce any confusion associated with peak description.

Table 3.1-1: Assigned characteristic peaks for neat PU

Wavenumber (cm^{-1})	Characteristic Peak
1072	C-O ether stretch
1111	C-O ether stretch
1223	C-O urethane stretch
1310	C-N aromatic secondary amine
1538	N-H bend and C=O stretch
1597	C=C aromatic ring stretch
1708	C=O stretch
1730	C=O stretch
2796	C-H and CH_2 stretch
2858	C-H and CH_2 stretch
2941	C-H and CH_2 stretch
3309	N-H stretch

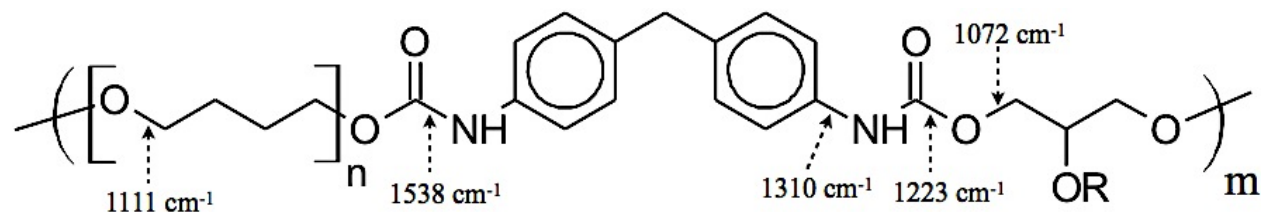


Figure 3.1-3: Labeled urethane bonds with their correlating wavenumbers

3.1.2.1 Analysis of crosslinking

The concentration of glycerin was varied to study the effect of crosslinking on the chemical structure of PU. Figures 3.1-4 and 3.1-5 show the IR spectra of PU crosslinked with 3 mmol, 6 mmol and 10 mmol of glycerin at low and high wavenumbers. As previously mentioned in the experimental section, the neat PU was crosslinked with 6 mmol of glycerin. It was observed in the spectra that peaks became more pronounced at 1072 cm^{-1} , 1710 cm^{-1} and 3309 cm^{-1} . The area under the 1072 cm^{-1} peak was divided by the area under the 1111 cm^{-1} peak to show that MDI and glycerin reacted as PTHF concentration was reduced (figure 3.1-6). The area of the 1710 cm^{-1} peak was divided by the area of the 1730 cm^{-1} peak to observe hard segment ratio at varied glycerin concentration (figure 3.1-7). Area under the 3309 cm^{-1} was calibrated with their respective spectrum's 1597 cm^{-1} C=C peak (figure 3.1-8) as expressed in the equation 5.

$$\text{Area under peak} = \frac{A_{3309}}{A_{1597}} \quad (5)$$

The 1072 cm^{-1} peak is characteristic of the C-O stretch from the hard/crosslinking segment of the polyurethane (composed of glycerin and MDI). As glycerin concentration increased, the ratio of 1072 cm^{-1} to 1111 cm^{-1} peak increased (figure 3.1-6). This can be due to (1) decreased PTHF concentration in the PU and (2) addition of crosslinks in the system as each functionality of glycerin

reacted with isocyanate groups. This trend was also observed in the 1710 cm^{-1} to 1730 cm^{-1} peak (figure 3.1-7) in which hydrogen-bonded carbonyl groups was greatest at higher glycerin concentration, indicating increased hard segment content. Finally, the area under the 3309 cm^{-1} peak (figure 3.1-8) showed that greater amounts of glycerin led to the formation of more N-H bonds. For all spectrums, no -OH groups were present around the 3400 cm^{-1} region. This demonstrated that all monomers reacted to completion and that crosslinking was present in the system as the hydroxyl groups belonging to glycerin were all reacted.

3.1.3 FTIR analysis of C30B

Figure 3.1-9 shows the spectrum of Cloisite 30B clay. At low wavenumbers of 460 cm^{-1} and 520 cm^{-1} , peaks arise due to inorganic moieties within the clay such as Mg-O bonds. Peaks observed at 919 cm^{-1} , 1043 cm^{-1} and 3626 cm^{-1} are designated to Al-OH-Al deformation, Si-O-Si stretch and silicate O-H stretch, respectively. While peaks at 1469 cm^{-1} , 2851 cm^{-1} and 2923 cm^{-1} pertain to CH_2 stretches from the organic modifier.

3.1.4 FTIR analysis of polyurethane-clay nanocomposites

IR spectra of PU nanocomposites are observed in figure 3.1-10. Incorporation of clay at concentrations between 2 wt% and 10 wt% led to the appearance of the silicate peak at 461 cm^{-1} . The increase in this peak's intensity can also be observed in figure 3.1-11. However, even with the addition of clay, characteristic polyurethane peaks can still

observed around the 1223 cm^{-1} , 1730 cm^{-1} and 3300 cm^{-1} regions confirming that clay did not obstruct the formation of polyurethane.

Since clay platelets have the ability to physically interact with urethane groups, the extent of hydrogen bonding within the system was studied. To do so, ratio of the area under the 1709 cm^{-1} and 1730 cm^{-1} peaks (figure 3.1-12) correlating to hydrogen bonded carbonyl and free carbonyl groups, respectively, were calculated. As shown in Table 3.1-2, hydrogen bonding increased up to 0.5 wt% clay. Beyond this concentration, hydrogen interactions decreased. The degree of clay dispersion could be a source for this behavior such that clay layers tending toward intercalation or agglomeration have decreased surface area and therefore result in fewer interactions with urethane linkages.

Table 3.1-2: Effect of clay concentration on hydrogen bonding

Sample	A_{1710}/A_{1730}
Neat PU	0.68
PU-C025	0.76
PU-C05	0.86
PU-C1	0.80
PU-C2	0.71
PU-C5	0.71
PU-C10	0.73

3.1.5 Clay dispersion

The spacing between silicate layers within the nanocomposites were studied by using XRD. Figure 3.1-13 shows the XRD pattern of C30B clay. A strong peak was observed at peak at $2\theta=4.78\pm 0.03^\circ$ (d-spacing of $18.46\pm 0.1\text{\AA}$) which coincides with values reported by others [88]. XRD patterns of neat PU and PU nanocomposites are

shown in figures 3.1-14 and 3.1-15. No peaks were observed in the PU nanocomposites containing 0.25 wt%, 0.5 wt% and 1 wt% clay (figure 3.1-14(b-d)). This demonstrated that ordered arrangement of the clay layers was completely lost and clay platelets were exfoliated. Additionally, exfoliated clay structure indicated that silicate layers were well dispersed within the PU matrix.

PU nanocomposites containing 2 wt%, 5 wt% and 10 wt% clay (figure 3.1-15(a-c)) show weak, broad peaks at $2\theta=4.55\pm 0.07^\circ$ (d-spacing of $19.4\pm 0.3\text{\AA}$), $2\theta=4.46\pm 0.08^\circ$ (d-spacing of $19.8\pm 0.4\text{\AA}$) and $2\theta=4.86\pm 0.03^\circ$ (d-spacing of $18.1\pm 0.2\text{\AA}$), respectively. At 2 wt% and 5 wt% clay, the clay gallery spacing increased in comparison to C30B indicating that PU chains had penetrated clay layers resulting in intercalated clay morphology. It was also observed that the intensities of the peaks in the nanocomposites decreased in comparison to C30B, which indicates that some parts of the nanocomposites are partially exfoliated. At 10 wt% clay loading, the d-spacing slightly decreased below the d-spacing of C30B clay indicating the nanocomposite may be agglomerated. It is assumed that aggregated clay has smaller gallery spacing due to platelets stacking closer together, which would result in an upward shift in 2θ . This inability of the silicate layers to be properly dispersed in the PU matrix is hypothesized to be a consequence of too much clay being present in the system such that the free volume is significantly reduced [89]. Since well-dispersed clay often produce nanocomposites with enhanced properties, it can be said that the optimal clay concentration in the crosslinked PU system should be at or below 1 wt%.

3.1.6 Morphology

The cross-sectional morphology of the nanocomposites was also explored for all specimens as it provides information concerning the interior surface, existence of voids, et cetera [90]. In the SEM micrograph of C30B powder shown in figure 3.1-16(a-b), aggregates were dominant in the sample as clay existed in its conventional form. Rough and layered-like structures were observed in the aggregates. The average width of larger clay particles were measured to be 7 ± 2 μm . The morphologies of neat PU and PU nanocomposites are observed in figures 3.1-17 through 3.1-23. For the neat PU, PU-C025, PU-C05 and PU-C1 specimens, a smooth cross-sectional morphology was observed demonstrating homogeneity in their physical structure. As clay concentration increased to 2 wt%, the morphology showed slight fibrous-like structures (figure 3.1-21a). Intercalation of clay may have led to this behavior. Additionally, this indicates the presence of phase separation taking place within the nanocomposite. Similar morphology was observed for nanocomposites at 5 wt% and 10 wt% loading (figures 3.1-22a and 3.1-23a), however, more voids were present in these specimens. Measurement of these pore-like spaces showed an average perimeter of 3 ± 2 μm for the 5 wt% clay nanocomposite and 5 ± 3 μm for the 10 wt% clay nanocomposite. This showed that high amounts of clay facilitated phase separation behavior as a result of aggregation within the matrix. At higher magnifications of the 5 wt% clay nanocomposite (figure 3.1-22b) more voids were present within a void demonstrating that intercalation/aggregation was present throughout the matrix. In the 10 wt% nanocomposite (figure 3.1-23b), clay aggregates saturated the matrix such that morphology was visibly layered and rough.

3.1.7 Surface properties

The Wilhelmy plate technique measures contact angle indirectly by detecting the change in weight as the specimen is immersed then withdrawn in a test liquid [86]. In relation to the drop-method, which only measures the surface, the plate method takes into account the cross-section in order to achieve a more accurate contact angle measurement that reflects the properties of the entire sample [91].

Table 3.1-3 shows the contact angles of neat PU and PU nanocomposites measured with water. It is observed that the contact angles increased as clay concentration in the nanocomposites was increased. This shows that hydrophobicity was significantly enhanced upon clay addition. It is hypothesized that increase in hydrophobicity (especially at concentrations between 2 wt% and 10 wt% clay) could be due to the rough matrix induced by clay particles, as previously observed in SEM.

Table 3.1-3: Measured contact angles of neat PU and PU nanocomposites

Sample	Contact Angle-Water (°)
Neat PU	37.7 ± 0.5
PU-C025	47.6 ± 0.5
PU-C05	58.1 ± 0.5
PU-C1	66.3 ± 0.5
PU-C2	71.9 ± 0.5
PU-C5	72.3 ± 0.5
PU-C10	75.3 ± 0.5

The surface energies of neat PU and PU nanocomposites are shown in figure 3.1-24. It is observed that surface energy decreased as clay concentration increased. This indicated that the nanocomposites wettability in water was reduced. Because the filler is

organophilic, this shows that the bulk properties of nanocomposites are slowly being dominated by the chemical nature of the clay.

3.2 Rheological Properties

Understanding the flow of polymer solutions is critical during processing where a lower viscous solution is easier to process in comparison to a solution with higher viscosity. In this section, the effect of clay and change in temperature will be studied to observe how these variables affect the rheology of polymers.

3.2.1 Effect of clay

The viscosities of neat PU and PU nanocomposites at 25°C are shown in figure 3.2-1. It is observed that clay reduced the overall viscosity of the neat PU as shear rate increased. This behavior can be explained by clay platelets interfering with polymerization leading to lower molecular weight polymer chains being formed, prior to curing. Since viscosity is dependent on the concentration and size of the polymer, a lower molecular weight polymer would be less effective in increasing the viscosity of the polymer solution than a higher molecular weight polymer, therefore solution viscosity will be lower. Additionally, the neat PU showed shear thinning-like behavior, which could be attributed to the low concentration of PU prepared in DMF solvent during polymerization. Shear-thinning behavior was also slightly observed in the PU-C025, PU-C1, PU-C5 and PU-C10 solutions. For coating applications, shear thinning behavior is

desired as it allows good spreadability and reduces the risk of aggregate formation during processing.

3.2.2 Effect of temperature

The viscosities of neat PU and PU nanocomposites as a function of temperature are shown in figures 3.2-2 to 3.2-8. For the neat PU (figure 3.2-2), increasing the temperature to 40°C resulted in overall reduction in viscosity and the appearance of a more prominent shear thinning behavior followed by a plateau in viscosity. Further increase in temperature to 70°C led to a similar behavior. As shown in the rheological data for PU-C025 (figure 3.2-3), shear thinning was also observed as temperature was increased, at low shear rates. At higher shear rates, slight perturbations in viscosity can be observed. This indicated that slight shear thickening behavior maybe occurring. At increased clay concentrations, more fluctuations can be observed at higher shear rates. The slight increases in viscosities could be a direct effect of clay-urethane interactions where strong interactions would impose restrictions to chain motion and therefore thicken the solution. In the 10 wt% clay nanocomposite solution (figure 3.2-8), it is observed that at 70°C, the overall viscosity was greater than the viscosity at 60°C. This unique behavior was attributed to clay agglomeration, which would lead to increased viscosity [92]. It was noticed that for all polymer solutions, as temperature increased the surface of the polymer began to form a gel-like film. This observation may have been an indication that high temperatures induced crosslinking reactions to take place within the PU system. Additionally for the PU nanocomposites, this behavior could also be due to interfacial

interactions between clay and urethane groups through means of physical or chemical crosslinking.

The energy required for viscous flow of polymer solutions was acquired through the Arrhenius equation (equation 6), which describes how viscosity varies with temperature at a constant shear rate [93].

$$\eta = Ae^{\frac{E_a}{RT}} \quad (6)$$

The variables, η , A, E_a , R and T represent the viscosity of solution, Arrhenius constant, activation energy, universal gas constant and temperature, respectively. Linearization of this equation can be achieved by taking the natural log of both sides, as presented in equation 7 [93].

$$\ln \eta = \frac{E_a}{RT} + \ln A \quad (7)$$

By plotting $\ln \eta$ versus $1/T$ (figure 3.2-9), the activation energy can be attained by multiplying the slope with the gas constant.

Table 3.2-1 reports the calculated activation energies of neat PU and PU nanocomposites at constant spindle speeds of 10 rpm, 30 rpm, 50 rpm and 100 rpm. It was demonstrated that at low spindle speeds of 10 rpm and 30 rpm, PU-C1 experienced the highest activation energy. At higher spindle speeds of 50 rpm and 100 rpm, the PU-C2 nanocomposite exhibited the greatest activation energy. Since activation energy is dependent on the rate at which viscosity decreases as a function of increasing

temperature, it can be assumed that the 1 wt% clay nanocomposite exhibited the greatest thermal sensitivity at lower spindle speeds whereas the 2 wt% nanocomposite exhibited the highest thermal sensitivity at higher spindle speeds. This unique phenomenon is assumed to be due to deformation of clay-urethane bonds in the nanocomposite systems as temperature is increased. Such deformation includes the shear force aligning the clay layers into the direction of motion, which would result in greater reduction in viscosity. The PU-C10 nanocomposite has the lowest activation energy for all spindle speeds. The reasoning behind this could be due to the applied shear force being unable to break apart clay agglomerates and therefore viscosity would slightly increase or maintain relatively constant.

Table: 3.2-1: Activation Energies (in KJ/mol) at varied spindle speeds

Sample	10 RPM	30 RPM	50 RPM	100 RPM
Neat PU	14.0	15.7	15.8	15.9
PU-C025	19.9	18.3	16.8	16.2
PU-C05	26.0	18.5	18.0	18.3
PU-C1	26.4	27.6	22.2	21.0
PU-C2	21.2	27.5	26.5	22.7
PU-C5	18.9	17.5	10.9	15.8
PU-C10	8.30	11.0	8.90	8.80

3.3 Dynamic Mechanical Properties

Dynamic mechanical spectroscopy (DMS) provides information on the dynamic mechanical properties of polymers undergoing sinusoidal deformation as a function of temperature [94, 95]. This technique was used to understand the influences of filler content on the structural and thermo-mechanical behavior of crosslinked PU.

3.3.1 Presence of crosslinks in neat polyurethane

To demonstrate that crosslinking in the neat PU system was formed, DMS was performed on both the neat PU system and a linear PU system that was composed of PTHF, MDI and 1,4-butanediol as the short-diol chain extender. The synthesis of the linear system was carried out in the same manner as the crosslinked system to reduce any disparity. The storage moduli and $\tan \delta$ curves of crosslinked and linear PU are shown in figures 3.3-1 and 3.3-2, respectively. The crosslinked neat PU exhibited a higher rubbery plateau modulus than the linear PU, indicating greater elasticity within the system. Generally, the rubbery plateau modulus increases as restrictions to motion are imposed by the crosslink networks.. The $\tan \delta$ plot for the crosslinked PU showed a lower peak height than the linear PU, which is indicative of a lower damping ability due to constraints to chain mobility. From the $\tan \delta$ versus temperature plots, it was shown that the glass-transition temperature (T_g) of crosslinked PU is -43°C and that for the linear PU is -53°C . This observed disparity in T_g is in agreement with data reported by Chiou *et al.* [34] in which the authors demonstrated that increasing crosslink density directly increased T_g due to greater restrictions in molecular motion of the polymer.

3.3.2 Effect of clay on storage modulus

The storage modulus of neat PU and PU nanocomposites are shown in figure 3.3-3. The glassy region storage modulus (E_G) is indicative of the rigidity of a material below T_g . The change in E_G as a function of clay concentration is shown in figure 3.3-4. As observed, E_G sharply increased once 0.25 wt% clay was introduced to the PU. At higher

concentrations of clay, the modulus continued to increase until reaching a plateau at 5 wt% clay. The enhancement in modulus is attributed to good interfacial interactions existing between clay and urethane groups by means of hydrogen bonding. This physical interaction can alter chain mobility and enhance overall stiffness of the nanocomposite substantially. After adding 10 wt% of clay to the matrix, a slight decrease in E_G was observed. This behavior can be a result of clay being unable to properly disperse throughout the matrix and agglomerating as a consequence. Agglomeration would negate the properties of the polymer that can be attained because this would lead to formation of a microcomposite system. Additionally, lack of proper dispersion would lead to reduced contact between the clay and urethane groups, and therefore reduced hydrogen bonding in the system, as previously calculated in Table 3.1-2.

The glass-transition region lies between the glassy region and rubbery plateau region of the storage modulus. Nanocomposites containing between 0.25 wt% to 1 wt% clay showed a narrow transition similar to what was observed in neat PU. This suggested that a homogenous matrix was achieved due to clay layers being fully exfoliated and uniformly distributed. Additionally, this concurs with the phase morphology observed in cross-sectional SEM images such that a smooth matrix with little to none clay aggregates or voids were present. Between 2 wt% and 10 wt% clay loading, a broad transition was observed indicating that a heterogeneous matrix resulted, which also correlated with SEM results. It is assumed that high concentrations of rigid clay may facilitate micro-phase separation by means of increasing the hard segment content in the PU. The disparity in soft and hard segment content can arise from C30B's organic surfactant modifiers having

the ability to chemically and physically interact with isocyanate and urethane groups, respectively. Also, clay aggregation may play a role such as causing a disturbance in the PU chains during curing.

The rubbery plateau modulus (E_R) characterizes the elasticity of polymers. The change in E_R as a function of clay concentration can be observed in figure 3.3-5. Increases in this modulus can be affected by the rigidity of silicate layers restricting chain motion and physical crosslinking present between the filler and matrix. To determine the enhancement in modulus (E_δ), equation 8 was used:

$$E_\delta = \frac{E_f}{E_m} \quad (8)$$

Where E_f is the modulus of the filled polyurethane and E_m is the modulus of the neat polyurethane. In figure 3.3-6, the change in E_δ as a function of clay volume fraction is shown. By taking the tangent of E_δ at low and high clay concentrations, the percolation threshold was determined to be at 0.65 vol% (or 1.2 wt%). Below this threshold, E_R increased significantly as a result of good interfacial interactions existing between the two components. Optimum value of elasticity was reached at 1 wt% clay loading. Surpassing this limit led to slower modulus increase, which suggests that a jammed system was present [96, 97].

Additionally, the experimental modulus was compared to the Halpin-Tsai (H-T) model, which is based on the assumption that the silicate platelets are completely

exfoliated. To calculate values for this theoretical model, a modified H-T equation (equations 9-11) was used to compensate for geometry of clay [98].

$$E_c = E_m [(1 + \xi \eta \phi_f) / (1 - \eta \phi_f)] \quad (9)$$

$$\eta = [(E_f/E_m) - 1] / [(E_f/E_m) + \xi] \quad (10)$$

$$\xi = 2 \left[\frac{l}{t} \right] \quad (11)$$

Where E_c , E_m and E_f are the composite modulus, matrix modulus and filler modulus, respectively, Φ_f is the volume fraction of the clay filler and $[l/t]$ is the aspect ratio of the filler (in this case ~ 100) [98]. Figure 3.3-7 shows the experimental composite modulus calculated Halpin-Tsai composite modulus. At low volume fractions of clay, the model predicted values that fit to those of the experimental, however at higher volume fractions ($\Phi_f > 1$), the model began to deviate significantly. This demonstrates that at clay loading between 0.25 wt% and 1 wt%, the clay platelets were highly oriented and achieved better dispersion [96]. This would support the results observed in XRD such that no peaks were observed in their diffractograms. At higher concentrations it is suspected that clay platelets were non-exfoliated aggregates and filler-filler interactions existed as a result.

3.3.2 Effect of clay on $\tan \delta$

Figure 3.3-8 shows the temperature-dependent $\tan \delta$ peaks for alpha transition of the neat PU and PU nanocomposites. Between 0.25 wt% and 1 wt% clay, a narrow peak possessing one T_g (denoted as $T_{g,1}$) was observed. This is synonymous with their

corresponding glass-transition regions observed in the storage modulus versus temperature curves. Exceeding 1 wt% clay led to further $\tan \delta$ peak broadening and the appearance of a second T_g (denoted as $T_{g,2}$). The nanocomposites' T_g values are presented in figure 3.3-9. The neat PU has a single $T_{g,1}$ at -39°C . As clay content increased, a shift in $T_{g,1}$ to lower temperatures was observed. This phenomenon could be attributed to clay limiting the curing process of the nanocomposites, which may result in lower amounts of chemical networks being formed in the matrix [99]. In nanocomposites with 2 wt% to 10 wt% clay, a second T_g was observed ($T_{g,2}$), which shifted to higher temperatures as clay concentration increased. It is believed that in these nanocomposites, the hard segment present in the PU was increased and required higher temperatures to initiate chain motion.

Furthermore, damping properties of the neat PU and PU nanocomposites were obtained by measuring the area under the $\tan \delta$ curve. Damping is associated with the ability of a material to dissipate energy upon deformation. A higher area demonstrates a higher ability for energy dispersion and vice versa for a smaller area. Figure 3.3-10 shows the variation of $\tan \delta$ peak area with clay concentration. Neat PU exhibited the highest damping ability and incorporation of clay significantly decreased damping up to 43% as shown by PU-C10 containing 10 wt% clay. This demonstrated that flexibility of the chains was reduced and higher degrees of molecular interactions were existent in the nanocomposites' matrix.

3.4 Corrosion Evaluation

3.4.1 Direct Current Polarization

DCP is an effective electrochemical technique used to characterize general corrosion behavior in coatings. The open current potential, E_{corr} , reflects the potential at which the rate of cathodic and anodic half-cell reactions are equal and the current density, I_{corr} , is directly proportional to corrosion rate.

3.4.1.1 Tafel plots

The polarization curve for bare Al alloy is shown in figure 3.4-1. For coated Al alloy substrates, Tafel curves generated over the course of 7 days, 14 days, 30 days and 60 days are shown in figures 3.4-2, 3.4-3, 3.4-4, and 3.4-5, respectively. Within 2h of exposure to salt water, the bare Al alloy was passivated as shown by the sharp increase in the slope of the anodic arm of the Tafel curve. Passivation behavior occurs when an Al alloy is in contact with a corrosive environment [100] and generally involves the substrate forming of an oxide layer on its surface as a defense against further corrosion. For coated Al alloy, after 7 days immersion (figure 3.4-2), no passivation was observed. This demonstrated that all coatings provided an immediate protective layer to restrict salt water from reaching the substrate's surface. After 30 days of salt water exposure, (figure 3.4-4) passivation of Al alloy coated with neat PU, PU-C2, PU-C5 and PU-C10, respectively, was observed. Furthermore after 60 days of salt water exposure, (figure 3.4-5) no passivation occurred in the substrate coated with PU-C025, PU-C05 and PU-C1,

respectively. This demonstrated that salt water had not yet permeated through these coatings.

3.4.1.2 E_{corr} and I_{corr}

The change in E_{corr} over the course of 60 days is shown in figure 3.4-6. After 30 days of exposure, the substrate coated with neat PU, PU-C2, PU-C5 and PU-C10, respectively, exhibited much lower E_{corr} values than the substrate coated with nanocomposites containing lower concentrations of clay (between 0.25 wt% and 1 wt%). After 60 days immersion, the E_{corr} value was greatest in the nanocomposite coating containing 0.25 wt% clay. The range in E_{corr} for all coatings from highest to lowest can be observed below:

$$PU-C025 > PU-C1 > PU-C05 > \text{neat PU} > PU-C2 > PU-C10 > PU-C5$$

Generally, higher E_{corr} values are correlated with better resistance to corrosion [101]. Since the addition of clay at low amounts yielded less negative E_{corr} values, this demonstrates that clay was able to form a protective barrier to inhibit redox reactions from occurring at the Al alloy surface.

The change in I_{corr} over the course of 60 days is shown in figure 3.4-7. In the first 2 weeks of exposure, the I_{corr} values remained relatively consistent for all coatings, ranging between 14 nA to 23 nA on day 7, and between 13 nA to 25 nA on Day 14. After 30 days exposure, I_{corr} drastically increased to the μA range for neat PU (2.3 μA), PU-C5 (0.50 μA) and PU-C10 (0.11 μA) coatings. This drastic increase in current density can be

correlated with the coatings' resistance to polarization being degraded. As reported in Table 3.4-1, it is observed on day 30 that the corrosion rate for neat PU, PU-C5 and PU-C10 are significantly higher than other coatings. After 60 days salt water immersion, it was observed that these coating had decreased in corrosion rate, which could be attributed to the metal's passive oxide layer suppressing the anodic reaction from progressing on the surface. The corrosion rate was lowest for the PU-C025, PU-C05 and PU-C1 coatings after the 60-day period, which demonstrates that PU with lower clay concentration had better resistance to corrosion. This could be due to the exfoliated clay being able to form a better protective barrier within the PU system.

Table 3.4-1: Corrosion rate of all coatings over a 60-day salt water exposure period

Time (Days)	Neat PU	PU-C025	PU-C05	PU-C1	PU-C2	PU-C5	PU-C10
	Corrosion Rate ($\times 10^{-3}$ mils per year)						
7	2.2	2.5	3.6	2.5	2.7	2.5	3.4
14	1.9	3.3	3.8	2.8	3.0	2.0	3.4
30	350	3.5	4.7	2.8	2.5	73	16
60	92	3.3	3.6	3.1	8.9	41	47

The polarization resistance (R_p) reflects the coatings ability to resist applied current that induces corrosion. By using taking the slopes of the anodic and cathodic arms, and extrapolating i_{corr} from the Tafel curve, R_p can be calculated using the Stern-Geary equation (equation 12) [102].

$$R_p = 2.303 \frac{\beta_a \beta_c}{\beta_a + \beta_c} \left(\frac{1}{i_{corr}} \right) \quad (12)$$

The calculated values of R_p for neat PU and PU nanocomposites are reported in Table 3.4-2. The R_p values of the substrates coated with neat PU, PU-C5 and PU-C10 decreased significantly after 30 days immersion in salt water. This demonstrates that the electrical resistivity in these coatings was decreased. The substrate coated with PU-C025, PU-C05, PU-C1 and PU-C2, respectively, displayed high R_p values that maintained relatively in the same magnitude after 30 days exposure. After 60 days exposure, the R_p of the substrate coated with PU-C2 decreased significantly while the R_p of other coatings did not budge. A higher R_p is indicative of greater resistance to corrosion, whereas a lower value indicates poor resistance to corrosion.

Table 3.4-2: Polarization resistance of neat PU and PU nanocomposites over a 60-day period

Time (Days)	Neat PU	PU-C025	PU-C05	PU-C1	PU-C2	PU-C5	PU-C10
Polarization Resistance ($\times 10^7$ ohms)							
7	8.9	8.0	1.4	4.5	6.3	7.3	4.4
14	11	6.0	1.5	4.0	5.6	7.9	4.7
30	0.020	4.6	1.4	3.9	1.2	0.051	0.16
60	0.026	5.0	1.1	2.5	0.31	0.068	0.052

3.4.2 Electrochemical Impedance Spectroscopy

EIS was used to evaluate the barrier properties and corrosion performance of all coatings. Unlike DCP tests, EIS is a non-destructive method that characterizes the changes in coating behavior after being exposed to a corrosive environment.

3.4.2.1 Nyquist and Bode plots

The Nyquist plot of bare Al alloy is shown in figure 3.4-8. For all coated substrates, the Nyquist plots after salt water exposure for 7 days, 14 days, 30 days and 60

days are shown in figures 3.4-9(a-b), 3.4-10(a-c), 3.4-11(a-b) and 3.4-12(a-b), respectively. The Nyquist plot allows for a single impedance value to be obtained at a specified frequency. Impedance can also be correlated to a coating's ability to resist polarization.

From high to low frequencies two semi-circles were observed in the bare Al substrate (figure 3.4-8) after exposure to saltwater for less than 2h. The latter semi-circle demonstrated that corrosion has commenced on the surface of the metal. For neat PU and PU nanocomposite coatings, one time-constant was observed in their Nyquist plot after 7 days immersion in saltwater (figure 3.4-9). A single time constant depicts that salt water had interacted with the coating and begun to alter the coating's dielectric properties [103]. The equivalent circuit used to fit a one-time constant Nyquist plot is shown in figure 3.4-13 where R_s is the resistance of the NaCl solution, C_c is the coating capacitance, R_{ct} is the charge transfer resistance (or polarization resistance) and W_B is the bounded Warburg diffusion.

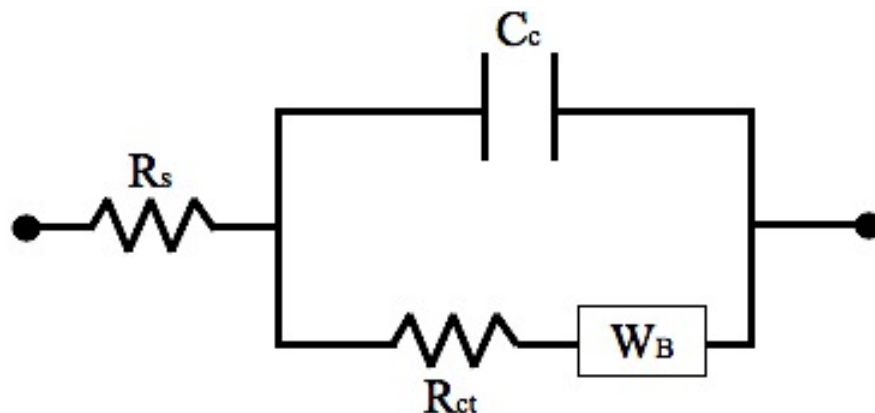


Figure 3.4-13: Equivalent circuit for coating with one-time constant

A complete second semicircle, indicative of a two-time constant, was observed for neat PU and PU-C5 after 14 days exposure (figure 3.4-10), indicating the coating has been damaged. The curve showing two-time constants was fitted using the equivalent circuit shown in figure 3.4-14, where R_{po} is the pore resistance and C_{dl} is the double-layer capacitance.

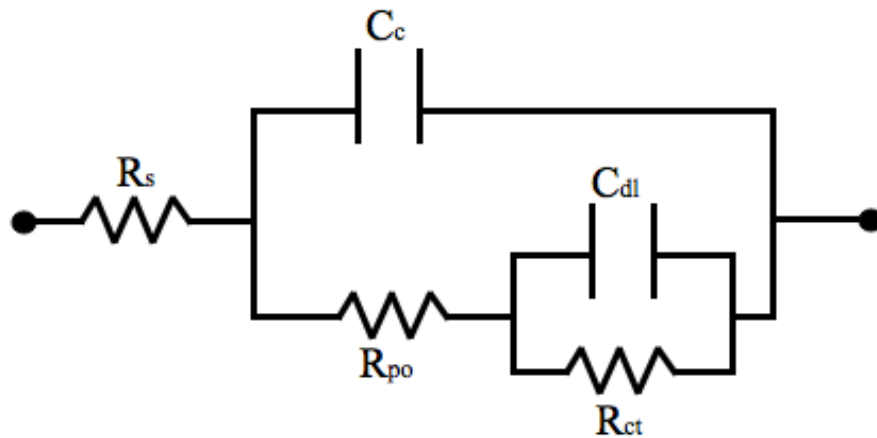


Figure 3.9-8: Equivalent circuit for coating with two time-constants

Additionally, failure of the PU-C5 coating showed a minor inductive loop appearing at low frequency. The inductive loop is due to adsorption of intermediate products in the corrosion reaction [104]. After 30 days (figure 3.4-11), the PU-C10 coating failed, however a significant increase in the impedance was observed after corrosion had initiated. It is hypothesized that this behavior is attributed to the surface of the Al substrate being altered to defend itself against corrosion. Further exposure to salt water for 60 days (figure 3.4-12) led to the PU-C025, PU-C05 and PU-C1 coatings maintaining a one-time constant with slight decrease in impedance.

The Bode plots of bare Al alloy, neat PU and PU nanocomposites can be observed in figures 3.4-15 through 3.4-22. In comparison to the Nyquist plot, Bode plots show the change in impedance as frequency is increased. At very high frequencies, the solution resistance is present, however this is not observed since the instrument is unable to go above 10^6 Hz. Fortunately, solution resistance only measures the salt water's resistance, which can be ignored in this case. Two dips in impedance was observed in the bare Al alloy Bode plot (figure 3.4-15), which shows that corrosion has commenced. In reference with the Nyquist plot, the first dip in impedance corresponds to the first-semi-circle showing coating resistance and the second dip is the second semi-circle indicative of corrosion.

The Bode plot of neat PU (figure 3.4-16) showed that after corroding on day 14, continued immersion in salt water decreased the impedance even further. This trend was also true for the PU-C5 (figure 3.4-21) coating, which failed on days 14. The PU-C10 (figure 3.4-22) coating showed an increased after corrosion initiated on day 30, which can be attributed to a thicker oxide layer being formed on the Al surface therefore providing a more defensive barrier to corrosion. It was interesting to observe that coatings possessing high quantities of clay failed within a month of immersion. Since the clay was unable to properly disperse and form a homogenous matrix, this showed that the barrier properties in these nanocomposites were not optimized. From SEM images, it was observed that greater quantities of voids were present in the PU-C5 and PU-C10 nanocomposites. Because of this morphology, it is assumed that corrosive ions and water were able diffuse through the coating more easily and reach the substrate at a faster rate.

After 60 days immersion in salt water, the PU-C025 (figure 3.4-17), PU-C05 (figure 3.4-18) and PU-C1 (figure 3.4-19) coatings did not show signs of corrosion. As time elapsed, the impedance values were only slightly decreased, but still remained above 10^6 ohm. Prior researchers have stated that coatings possessing impedance below 10^6 are shown to have poor corrosion protection [105, 106]. This significant enhancement in the PU barrier properties is likely a result of the exfoliated clay being able to form a tortuous pathway in the matrix to suppress the diffusion of water and oxygen to the metallic surface. From these results, it can be said that low clay concentrations are optimal for crosslinked PU to possess better barrier properties.

3.4.2.2 Coating lifetime

Accelerated lifetime prediction of coatings is critical in evaluating how long a coating will last prior to failure. The lifespan can be estimated by correlating the change in coating resistance overtime until failure. Figure 3.4-23 shows the change in initial impedance as a function of immersion time. The plot was fitted with a straight line indicating that coating failure for the neat PU, PU with low clay concentration and PU with high clay concentration all followed a first order decay. The proposed equation to predict time until failure is expressed in equation 13 [107].

$$t_{fail} = \theta \left[\ln \left(\frac{Z_0 - Z_m}{Z_{fail} - Z_m} \right) \right] \quad (13)$$

Where Z_0 is the impedance of the fresh coating, Z_{fail} is the impedance at which the coating fails (in this case at 20 kohm), Z_m is the impedance of bare Al (1 kohm) and θ represents the decay constant. The decay constant was determined by taking the inverse of the slope obtained in the $\ln Z_t$ versus time plot, where Z_t is the impedance at time “t”.

Predicted lifetime of neat PU and PU nanocomposite coatings are shown in figure 3.4-24. The neat system was estimated to last less than a year in a corrosive environment followed by the PU-C10, PU-C5 and PU-C2 coatings with estimated lifespans of 0.5 years, 0.6 years and 0.8 years, respectively. At 1 wt% clay loading, the coating was approximated to last for 3 years, however optimization of PU with 0.25 wt% and 0.5 wt% clay significantly improved predicted coating lifetime up to 6-7.5 years.

Chapter 4: Conclusion

A series of crosslinked PU-clay nanocomposites were synthesized via *in-situ* polymerization, characterized and evaluated as a corrosion protective coating. FTIR analysis confirmed that urethane groups were formed in the prepared systems. Addition of clay reduced the viscosity of the PU solution demonstrating improvement in its processability. XRD analysis demonstrated that nanocomposites prepared with low clay concentrations between 0.25 wt% and 1 wt% existed with silicate layers that were well dispersed and exfoliated. Exceeding 1 wt% clay concentration led to silicate layers becoming intercalated and agglomerated as free volume within the matrix was reduced. SEM images of these nanocomposites revealed that clay lacking proper dispersion facilitated phase separation behavior to occur in the matrix leading to the formation of voids.

DMS analysis established that a crosslinked neat PU system was obtained through increase in rubbery plateau modulus, decrease in $\tan \delta$ peak and shift to higher T_g , when compared to a linear PU system. Upon addition of clay, an increase in storage modulus was observed, which can be attributed to the rigidity of the filler and physical interactions occurring between the clay and urethane groups. Additionally, nanocomposites possessing mediocre- to poorly- dispersed platelets caused possible formation of phase-separated microcomposites to occur due to increase in hard segment content.

DCP tests demonstrated that substrates coated with PU-C025, PU-C05 and PU-C1 specimens outperformed other coatings by achieving the lowest corrosion rates and delaying any signs of passivation. Prediction of these nanocomposite coatings' lifespan through EIS tests showed their life expectancy to last between 3 to 7.5 years, which is a significant improvement over the lifespan of the neat PU. It can be concluded that the concentration and dispersion of clay play a major role in improving the barrier properties required for a coating to have good corrosion protection.

Chapter 5: Suggestions and Future Work

The focus of this research was based on characterizing a novel crosslinked polyurethane clay nanocomposite system and testing the material as a potential applicant in corrosion resistant coatings. Although the goals of this work were achieved, further work is required to expand upon the characterization of this system. Such suggestions include:

- Application of TEM to observe the morphology of clay platelets.
- Utilization of AFM to study the surface of the neat PU and PU nanocomposite systems.

Additionally improvements to PU system are needed if it will have potential applications as a coating. When preparing the coatings, it was noticed that adhesion between the PU and aluminum alloy was not strong. This could have been due to PU lacking the proper polarity to bond to metallic substrates. In order to compensate for this, the PU can be prepared with isocyanate-terminated chains in which moisture can be used to cure the material onto the substrate. The formation of chemical bonds on the surface of metal is believed to provide a stronger bond between the two materials. Another possibility is to form a blend with a highly adhesive polymer such as epoxy.

Along with the topic of corrosion, the area of environmentally friendly coatings for corrosion protection has been a growing area. This leads to another future work interest, which involves the preparation of non-isocyanate-based polyurethanes for anticorrosion applications.

References

- [1] ISOPA, “History.” <http://www.polyurethanes.org/en/what-is-it/history> [Date accessed: Feb. 3, 2014]
- [2] R. B. Seymour, G. B. Kauffman, Polyurethanes: A Class of Modern Versatile Materials. (1992) *Journal of Chemical Education*, 69, 909-910.
- [3] American Chemistry Council, “Introduction to Polyurethanes.” <http://polyurethane.americanchemistry.com/Introduction-to-Polyurethanes> [Date accessed: Feb. 3, 2014]
- [4] W. J. Choi, S. H. Kim, Y. J. Kim, S. C. Kim, Synthesis of chain-extended organifier and properties of polyurethane/clay nanocomposites. (2004) *Polymer*, 45, 6045–6057.
- [5] C. N. Ha Thuc, H. T. Cao, D. M. Nguyen, M. A. Tran, L. Duclaux, A.-C. Grillet, H. Ha Thuc, Preparation and characterization of polyurethane nanocomposites using Vietnamese montmorillonite modified by polyol surfactants. (2014) *Journal of Nanomaterials*, 2014, 11 pages.
- [6] C. Wang, J. Jia, Damping and mechanical properties of polyol cross-linked polyurethane/epoxy interpenetrating polymer networks. (2014) *High Performance Polymers*, 26, 240-244.
- [7] K. S. Huang, S. W. Chen, L. A. Lu, R. R. Min, Synthesis and applications of polyurethane/carboxymethyl cellulose blended polymers. I. Compatibility of the PU/CMC blended polymer. (2007) *Cellulose Chemistry and Technology*, 41, 113-117.
- [8] K.-S. Chen, Y.-S. Chen, T. L. Yu, C.-L. Tsai, Physical properties of tri-isocyanate crosslinked polyurethane. (2002) *Journal of Polymer Research*, 9, 119-128.
- [9] J. M. Herrera-Alonso, E. Marand, J. C. Little, S. S. Cox, Transport properties in polyurethane/clay nanocomposites as barrier materials: Effect of processing conditions. (2009) *Journal of Membrane Science*, 337, 208-214.
- [10] S. S. Liow, V.T. Lipik, L. K. Widjaja, S. S. Venkatraman, M. J. M. Abadie, Enhancing mechanical properties of thermoplastic polyurethane elastomers with 1,3-trimethylene carbonate, epsilon-caprolactone and L-lactide copolymers via soft segment crystallization. (2011) *eXPRESS Polymer Letters*, 5, 897-910.

- [11] X. Cao, L. J. Lee, T. Widya, C. Macosko, Polyurethane/clay nanocomposites foams: processing, structure and properties. (2005) *Polymer*, 46, 775-783.
- [12] M. Kayalvizhi, E. Vakees, J. Suresh, A. Arun, Synthesis and characterization of poly (urethane-urea) based on functionalized polystyrene and MDI. (2014) *IOSR Journal of Applied Chemistry*, 7, 41-51.
- [13] M. Nayani, S. Gunashekar, N. Abu-Zahra, Synthesis and characterization of polyurethane-nanoclay composites. (2013) *International Journal of Polymer Science*, 2013, 5 pages.
- [14] D. J. dos Santos, L. B. Tavares, G. F. Batalha, Mechanical and physical properties investigation of polyurethane material obtained from renewable natural source. (2012) *Journal of Achievements in Materials and Manufacturing Engineering*, 54, 211-217.
- [15] C. Prisacariu, E. Scortanu, B. Agapie, Insights into polyurethane elastomers obtained by changing the polyaddition procedures. (2011) *Proceedings of the World Congress on Engineering*, Vol. III, London, 6 pages.
- [16] C. S. Wong, K. H. Badri, Chemical analyses of palm kernel oil-based polyurethane prepolymer. (2012) *Materials Sciences and Applications*, 3, 78-86.
- [17] J. Dodge, M. E. Rogers (Ed.), T. E. Long (Ed.), 'Polyurethanes and polyureas' in *Synthetic Methods in Step-Growth Polymers*. (2003) John Wiley & Sons, Hoboken, New Jersey, 197-258.
- [18] M.J. Forrest (Ed.), 'Background' in "Chemical Characterisation of Polyurethanes." (1999) Rapra Technology, United Kingdom, 3-4.
- [19] P. Krol, Synthesis methods, chemical structures and phase structures of linear polyurethanes. Properties and applications of linear polyurethanes in polyurethane elastomers, copolymers and ionomers. (2007) *Progress in Materials Science*, 52, 915-1015.
- [20] M. Spirkova, K. Dusek, Extent of side reactions and gelation of polyether polyurethanes. (1989) *Polymer Bulletin*, 22, 191-198.
- [21] A. Lapprand, F. Boisson, F. Delolme, F. Mechin, J.-P. Pascault, Reactivity of isocyanates with urethanes: Conditions for allophanate formation. (2005) *Polymer Degradation and Stability*, 90, 363-373.

- [22] K. Dusek, M. Spirkova, I. Havlicek, Network formation of polyurethanes due to side reactions. (1990) *Macromolecules*, 23, 1774-1781.
- [23] Q.-W. Lu, T. R. Hoyer, C. W. Macosko, Reactivity of common functional groups with urethanes: Models for reactive compatibilization of thermoplastic polyurethane blends. (2002) *Journal of Polymer Science: Part A*, 40, 2310-2328.
- [24] K.-L. Noble, Waterborne polyurethanes. (1997) *Progress in Organic Coatings*, 32, 131-136.
- [25] M. Spirkova, M. Kubin, K. Dusek, Side reactions in the formation of polyurethanes: Model reactions between phenylisocyanate and 1-butanol. (1987) *Journal of Macromolecular Science: Part A – Chemistry*, 24, 1151-1166.
- [26] H. Kothandaraman, K. Venkatarao, B. C. Thanoo, Preparation, properties, and crosslinking studies on polyurethane elastomers. (1989) *Polymer Journal*, 21, 829-839.
- [27] T. Tsonev, M. Herzog, S. Nenkova, Shape memory polyurethanes based on recycled polyvinyl butyral. I. Synthesis and morphology. (2013) *Central European Journal of Chemistry*, 11, 2058-2065.
- [28] H. Xia, M. Song, Z. Zhang, M. Richardson, Microphase separation, stress relaxation, and creep behavior of polyurethane nanocomposites. (2007) *Journal of Applied Polymer Science*, 103, 2992-3002.
- [29] M. Song, H. S. Xia, K. J. Yao, D. J. Hourston, A study on phase morphology and surface properties of polyurethane/organoclay nanocomposite. (2005) *European Polymer Journal*, 41, 259-266.
- [30] G. Gorrasi, M. Tortora, V. Vittoria, Synthesis and physical properties of layered silicates/polyurethane nanocomposites. (2005) *Journal of Polymer Science: Part B: Polymer Physics*, 43, 2454-2467.
- [31] Y. Berezkin, M. Urick, A. Patil ‘Modern Polyurethanes: Overview of structure property relationship’ in “Polymers for Personal Care and Cosmetics.” (2013) ACS Symposium Series, Washington, DC, 65-81.
- [32] C. P. Buckley, C. Prisacariu, A. Caraculacu, Novel triol-crosslinked polyurethanes and their thermorheological characterization as shape-memory materials. (2007) *Polymer*, 48, 1388-1396.
- [33] C. Liang, L. Li, C. Mao, N. Zhou, J. Zhang, J. Shen, ‘Synthesis and characterization of shape-memory polyurethane films with blood compatibility’ in “Proceedings of the

Second International Conference on Smart Materials and Nanotechnology in Engineering.” (2009) 7493, Weihai, China, 6 pages.

[34] B.-S. Chiou, P. E. Schoen, Effects of crosslinking on thermal and mechanical properties of polyurethanes. (2002) *Journal of Applied Polymer Science*, 83, 212-223.

[35] – D.-K. Lee, H.-B. Tsai, J. L. Standford, Phase separation and phase inversion of polyurethane networks. (1996) *Journal of Polymer Research*, 3, 159-163.

[36] M. Joulazadeh, A. H. Navarchian, Study on elastic modulus of crosslinked polyurethane/organoclay nanocomposites. (2011) *Polymer Advanced Technologies*, 22, 2022-2031.

[37] N. Kebir, I. Campistron, A. Laguerre, J.-F. Pilard, C. Bunel, New crosslinked polyurethane elastomers with various physical properties from natural rubber derivatives. (2011) *Journal of Applied Polymer Science*, 122, 1677-1687.

[38] D. K. Chattopadhyay, B. Sreedhar, K. V. S. N. Raju, Thermal stability of chemically crosslinked moisture-cured polyurethane coatings. (2005) *Journal of Applied Polymer Science*, 95, 1509-1518.

[39] K. Grigoriadi, A. Giannakas, A. Ladavos, N.-M. Barkoula, Thermomechanical behavior of polymer/layered silicate clay nanocomposites based on unmodified low density polyethylene. (2012) *Polymer Engineering and Science*, 53, 301-308.

[40] M. Kedzierski, P. Penczek, Unsaturated polyester/montmorillonite nanocomposites prepared by in situ intercalative copolyaddition. (2004) *Polimery*, 49, 801-805.

[41] T.-K. Chen, Y.-I. Tien, K.-H. Wei, Synthesis of novel segmented polyurethane/clay nanocomposites. (2000) *Polymer*, 41, 1345-1353.

[42] S. Y. Moon, J.-K. Kim, C. Nah, Y.-S. Lee, Polyurethane/montmorillonite nanocomposites prepared from crystallite polyols, using 1,4-butanediol and organoclay hybrid as chain extenders. (2004) *European Polymer Journal*, 40, 1615-1621.

[43] S. S. Ray, M. Okamoto, Polymer/layered silicate nanocomposites: A review from preparation to processing. (2003) *Progress in Polymer Science*, 28, 1539-1641.

[44] C. E. Corcione, P. Prinari, D. Cannoletta, G. Mensitieri, A. Maffezzoli, Synthesis and characterization of clay-nanocomposite solvent-based polyurethane adhesives. (2008) *International Journal of Adhesion and Adhesives*, 28, 91-100.

- [45] P. H. C. Camargo, K. G. Satyanarayana, F. Wypych, Nanocomposites: Synthesis, structure, properties and new application opportunities. (2009) *Materials Research*, 1, 1-39.
- [46] M. Joshi, K. Banerjee, R. Prasanth, and V. Thakare, Polymer/clay nanocomposite based coatings for enhanced gas barrier property. (2006) *Indian Journal of Fibre & Textile Research*, 31, 202-214.
- [47] S. SolarSKI, S. Benali, M. Rochery, E. Devaux, M. Alexandre, F. Monteverde, P. Dubois, Synthesis of a polyurethane/clay nanocomposite used as coating: Interactions between the counterions of clay and the isocyanate and incidence on the nanocomposite structure. (2005) *Journal of Applied Polymer Science*, 95, 238-244.
- [48] M. Strankowski, J. Strankowska, M. Gazda, L. Piszczyk, G. Nowaczyk, S. Jurga, Thermoplastic polyurethane/(organically modified montmorillonite) nanocomposites produced by in situ polymerization. (2012) *eXPRESS Polymer Letters*, 6, 610-619.
- [49] R. Xu, E. Manias, A. J. Snyder, J. Runt, Low permeability biomedical polyurethane nanocomposites. (2003) *Journal of Biomedical Materials Research Part A*, 64A, 114-119.
- [50] I. V. Khudyakov, R. D. Zopf, N. J. Turro, Polyurethane nanocomposites. (2009) *Designed Monomers and Polymers*, 12, 279-290.
- [51] H.-C. Kuan, W.-P. Chuang, C.-C. M. Ma, Synthesis and characterization of a clay/waterborne polyurethane nanocomposite. (2005) *Journal of Materials Science*, 40, 179-185.
- [52] M. J. Factor, S. Lee, 'Supercritical carbon dioxide processing of polymer-clay nanocomposites' in "Particle Technology and Applications." (2012) CRC Press, Florida, 235-238.
- [53] G.-L. Yuan, W.-M. Li, S. Yin, F. Zou, K.-C. Long, Z.-F. Yang, Nanocomposites of urethane and montmorillonite clay in emulsion: *In situ* preparation and characterization. (2009) *Journal of Applied Polymer Science*, 114, 1964-1969.
- [54] M. Abareshi, S. M. Zebarjad, E. K. Goharshadi, Effect of milling time and clay content on the thermal stability of polyethylene-clay nanocomposite. (2014) *Journal of Vinyl and Additive Technology*, Online Access DOI:10.1002/vnl.21443
- [55] Z. Wang and T. J. Pinnavaia, Nanolayer Reinforcement of elastomeric polyurethane. (1998) *Chemistry of Materials*, 10, 3769-3771.

- [56] J.-M. Yeh, C.-T. Yao, C.-F. Hsieh, L.-H. Lin, P.-L. Chen, J.-C. Wu, H.-C. Yang, C.-P. Wu, Preparation, characterization and electrochemical corrosion studies on environmentally friendly waterborne polyurethane/Na⁺-MMT clay nanocomposite coatings. (2008) *European Polymer Journal*, 44, 3046-3056.
- [57] A. Pegoretti, A. Dorigato, M. Brugnara, A. Penati, Contact angle measurements as a tool to investigate the filler matrix interactions in polyurethane-clay nanocomposites from blocked prepolymer. (2008) *European Polymer Journal*, 44, 1662-1672.
- [58] X. Dai, J. Xu, X. Guo, Y. Lu, D. Shen, N. Zhao, X. Luo, X. Zhang, Study on the structure and orientation action of polyurethane nanocomposites. (2004) *Macromolecules*, 37, 5615-5623.
- [59] C. Saha, T. K. Chaki, N. K. Singha, Synthesis and characterization of elastomeric polyurethane and PU/clay nanocomposites based on an aliphatic Diisocyanate. (2013) *Journal of Applied Polymer Science*, 130, 3328-3334.
- [60] M. Heidarian, M. R. Shishesaz, S. M. Kassiriha, Study on the effect of ultrasonication time on transport properties of polyurethane/organoclay nanocomposite coatings. (2011) *Journal of Coatings Technology and Research*, 8, 265-274.
- [61] B. C. Chun, T. K. Cho, M. H. Chong, Y.-C. Chung, J. Chen, D. Martin, R. C. Cieslinski, Mechanical properties of polyurethane/montmorillonite nanocomposite prepared by melt mixing. (2007) *Journal of Applied Polymer Science*, 106, 712-721.
- [62] W. Huang, C. D. Han, Dispersion characteristics and rheology of organoclay nanocomposites based on a segmented main-chain liquid-crystalline polymer having side-chain azopyridine with flexible spacer. (2006) *Polymer*, 47, 4400-4410.
- [63] K. C. Pradhan, P. L. Nayak, Synthesis and characterization of polyurethane nanocomposite from castor oil- hexamethylene diisocyanate (HMDI). (2012) *Advances in Applied Science Research*, 3, 3045-3052.
- [64] C. H. Dan, M. H. Lee, Y. D. Kim, B. H. Min, J. H. Kim, Effect of clay modifiers on the morphology and physical properties of thermoplastic polyurethane/clay nanocomposites. (2006) *Polymer*, 47, 6718-6730.
- [65] L. Pizzatto, A. Lizot, R. Fiorio, C. L. Amorim, G. Machado, M. Giovanela, A. J. Zattera, J. S. Crespo, Synthesis and characterization of thermoplastic polyurethane/nanoclay composites. (2009) *Materials Science and Engineering: C*, 29, 474-478.

- [66] A. Kaushik, D. Ahuja, V. Salwani, Synthesis and characterization of organically modified clay/castor oil based chain extended polyurethane nanocomposites. (2011) *Composites Part A: Applied Science and Manufacturing*, 42, 1534-1541.
- [67] S. Ashhari, A. A. Sarabi, S. M. Kasiriha, D. Zaarei, Aliphatic polyurethane-montmorillonite nanocomposite coatings: Preparation, characterization, and anticorrosive properties. (2011) *Journal of Applied Polymer Science*, 119, 523-529.
- [68] B. A. Shaw, R. G. Kelly, *What is Corrosion? The Electrochemical Society Interface*, Spring 2006, 24–26.
- [69] P. A. Sorensen, S. Kiil, K. Dam-Johansen, C. E. Weinell, Anticorrosive coatings: A review. (2009) *Journal of Coatings Technology and Research*, 6, 135–176.
- [70] C. G. Soares, Y. Garbatov, A. Zayed, G. Wang, Influence of environmental factors on corrosion of ship structures in marine atmosphere. (2009) *Corrosion Science*, 51, 2014–2026
- [71] NDT Resource Center, Corrosion. https://www.nde-ed.org/EducationResources/CommunityCollege/Materials/Physical_Chemical/Corrosion.htm [Date accessed: Feb. 3, 2015]
- [72] A. Foyet, T. H. Wu, L. van der Ven, A. Kodentsov, G. de With, R. van Benthem, Influence of mixing ratio on the permeability of water and the corrosion performance of epoxy/amine coated un-pretreated Al-2024 evaluated by impedance spectroscopy. (2009) *Progress in Organic Coatings*, 64, 138-141.
- [73] Y. Gonzalez-Garcia, S. Gonzalez, R. M. Souto, Electrochemical and structural properties of a polyurethane coating on steel substrates for corrosion protection. (2007) *Corrosion Science*, 49, 3514-3526.
- [74] M. C. L. de Oliveira, R. A. Antunes, I. Costa, Positron annihilation spectroscopy and electrochemical impedance spectroscopy studies of polyurethane-urea hybrid coatings. (2013) *International Journal of Electrochemical Science*, 8, 7656-7668.
- [75] K.-C. Chang, S.-T. Chen, H.-F. Lin, C.-Y. Lin, H.-H. Huang, J.-M. Yeh, Y.-H. Yu, Effect of clay on the corrosion protection efficiency of PMMA/Na⁺-MMT clay nanocomposite coatings evaluated by electrochemical measurements. (2008) *European Polymer Journal*, 44, 13-23.
- [76] M. O'Donoghue, R. Garrett, V. Datta, P. Roberts, T. Aben, 'Electrochemical impedance spectroscopy: Testing coatings for rapid immersion service' in "Materials Performance." (Sept. 2003) NACE International, Houston, Texas, 36-41.

- [77] M. Behzadnasab, S. M. Mirabedini, M. Esfandef, Corrosion protection of steel by epoxy nanocomposite coatings containing various combinations of clay and nanoparticulate zirconia. (2013) *Corrosion Science*, 75, 134-141.
- [78] S. R. Taylor, Assessing the Moisture Barrier Properties of Polymeric coatings using electrical and electrochemical methods. (1989) *Electrical Insulation, IEEE Transactions on*, 24, 787-806.
- [79] N. Abacha, M. Kubouchi, K. Tsuda, T. Sakai, Performance of epoxy-nanocomposite under corrosive environment. (2007) *eXPRESS Polymer Letters*, 1, 364-369.
- [80] J.-M. Yeh, C.-P. Chin, S. Chang, Enhanced corrosion protection coatings prepared from soluble electronically conductive polypyrrole-clay nanocomposite materials. (2003) *Journal of Applied Polymer Science*, 88, 3264-3272.
- [81] A. M. Slavutsky, M. A. Bertuzzi, M. Armada, Water barrier properties of starch-clay nanocomposite films. (2012) *Brazilian Journal of Food Technology*, 15, 208-218.
- [82] M. Pannirselvam, A. Genovese, M. C. Jollands, S. N. Bhattacharya, R. A. Shanks, Oxygen barrier property of polypropylene-polyether treated clay nanocomposite. (2008) *eXPRESS Polymer Letters*, 2, 429-439.
- [83] O. Gain, E. Espuche, E. Pollet, M. Alexandre, P.H. Dubois, Gas barrier properties of poly(ϵ -caprolactone)/clay nanocomposite: Influence of the morphology and polymer/clay interactions. (2005) *Journal of Polymer Science: Part B: Polymer Physics*, 43, 205-214.
- [84] N. Jiratumnukul, P. Manowanna, N. Premmag, Modified bentonite clay in UV curable coating applications. (2010) *Engineering Journal*, 16, 13-18.
- [85] Brookfield Engineering Laboratories, Inc., 'More solutions to sticky problems' in "Brookfield Digital Viscometer Model DV-I+." Manual No: M/92-021-A-892, pp. 18.
- [86] CAHN Instruments, DCA Applications Software Manual. (1991) Cerritos, CA, 40 pages.
- [87] J. A. Hiltz, J. P. Szabo, FT-IR study of poly(ether)urethanes. (2001) Defence R&D Canada, DREA TM 2001-073
- [88] C. GunaSingh, S. Soundararajan, K. Palanivelu, Studies on mechanical, thermal properties and characterization of nanocomposites of nylon-6-thermoplastics poly urethane rubber [TPUR] blend. (2013) *IOSR-Journal of Applied Chemistry*, 4, 65-75.

- [89] S. Spoljaric, A. Salminen, N. D. Luong, P. Lahtinen, J. Vartiainen, T. Tammelin, J. Seppala, Nanofibrillated cellulose, poly(vinyl alcohol) montmorillonite clay hybrid nanocomposites with superior barrier and thermomechanical properties. (2014) *Polymer Composites*, 35, 1117-1131.
- [90] N. Erdman, R. Campbell, S. Asahina, Precise SEM cross section polishing via argon beam milling. (May 2006) *Microscopy Today*, 22-25.
- [91] Y. Yuan, T. R. Lee, 'Contact angle and wetting properties' in "Surface Science Technologies." (2013) *Springer Series in Surface Sciences*, 51, 3-34.
- [92] V. A. Agubra, P. S. Owuor, M. V. Hosur, Influence of Nanoclay Dispersion Methods in the Mechanical Behavior of E-Glass/Epoxy Nanocomposites. (2013) *Nanomaterials*, 3, 550-563.
- [93] D. Salomon, H. Zhai, Ranking Asphalt Binders by Activation Energy for Flow. (2002) *Journal of Applied Asphalt Binder Technology*, 2, 9 pages.
- [94] D. M. Price and P. J. Haines (Ed.), *Principles of Thermal Analysis and Calorimetry*. (2002) Royal Society of Chemistry, London, 94-105.
- [95] L. Feng, J. O. Iroh, Novel polyimide-b-polyurea supramacromolecule with remarkable thermomechanical and dielectric properties. (2013) *European Polymer Journal*, 49, 1811-1822.
- [96] S. Rooj, A. Das, K. W. Stockelhuber, D.-Y. Wang, V. Galiatsatos, G. Heinrich, Understanding the reinforcing behavior of expanded clay particles in natural rubber compounds, (2013) *Soft Matter*, 9, 3798-3808.
- [97] P. J. Jandas, S. Mohanty, S. K. Nayak, Rheological and mechanical characterization of renewable resource based high molecular weight PLA nanocomposites, (2013) *Journal of Polymers*, 2013, 11 pages.
- [98] J. Samaniuk, D. Litchfield, D. Baird, Improving the exfoliation of layered silicate in a poly(ethylene terephthalate) matrix using supercritical carbon dioxide, (2009) *Polymer engineering and science*, 2329-2341
- [99] J. Xiong, Z. Zheng, H. Jiang, S. Ye, X. Wang, Reinforcement of polyurethane composites with an organically modified montmorillonite. (2007) *Composites Part A: Applied Science and Manufacturing*, 38, 132-137.
- [100] J. Singh-Beemat, J. O. Iroh, The effect of morphology on the corrosion inhibition and mechanical properties of hybrid polymer coatings. (2013) *Journal of Applied Polymer Science*, 128, 1616-1624.

- [101] A. Ganash, Anticorrosive properties of poly(o-phenylenediamine)/ZnO nanocomposites coated stainless steel. (2014) *Journal of Nanomaterials*, 2014, 8 pages.
- [102] Metrohm Autolab, Corrosion part 3–Measurement of polarization resistance. Autolab Application Note COR03, July 2011, 2 pages.
- [103] D. Rajamani, Processing and properties of environmentally-friendly corrosion resistant hybrid nanocomposite coatings for aluminum alloy AA2024. (2005) MSc. Thesis, University of Cincinnati, 162 pages.
- [104] P. C. Okafor, X. Liu, Y. G. Zheng, Corrosion inhibition of mild steel by ethylamino imidazoline derivative in CO₂-saturated solution. (2009) *Corrosion Science*, 51, 761-768.
- [105] J. K. Saha, P. K. Mitra, S. Paul, D. D. N. Singh, Performance of different organic coatings on steel substrate by accelerated and in atmospheric exposure tests. (2010) *Indian Journal of Chemical Technology*, 17, 102-110.
- [106] R. C. Bacon, J. J. Smith, F. M. Rugg, Electrolytic resistance in evaluating protective merit of coatings on metals. (1948) *Industrial and Engineering Chemistry*, 40, 161-167.
- [107] G. Bierwagen, J. Li, L. He, D. Tallman and J. Martin (Ed.), ‘Fundamentals of the measurement of corrosion protection and the prediction of its lifetime in organic coatings’ in “In Service Life Prediction.” (2001) ACS Symposium Series; Washington, 316-333.

Figures

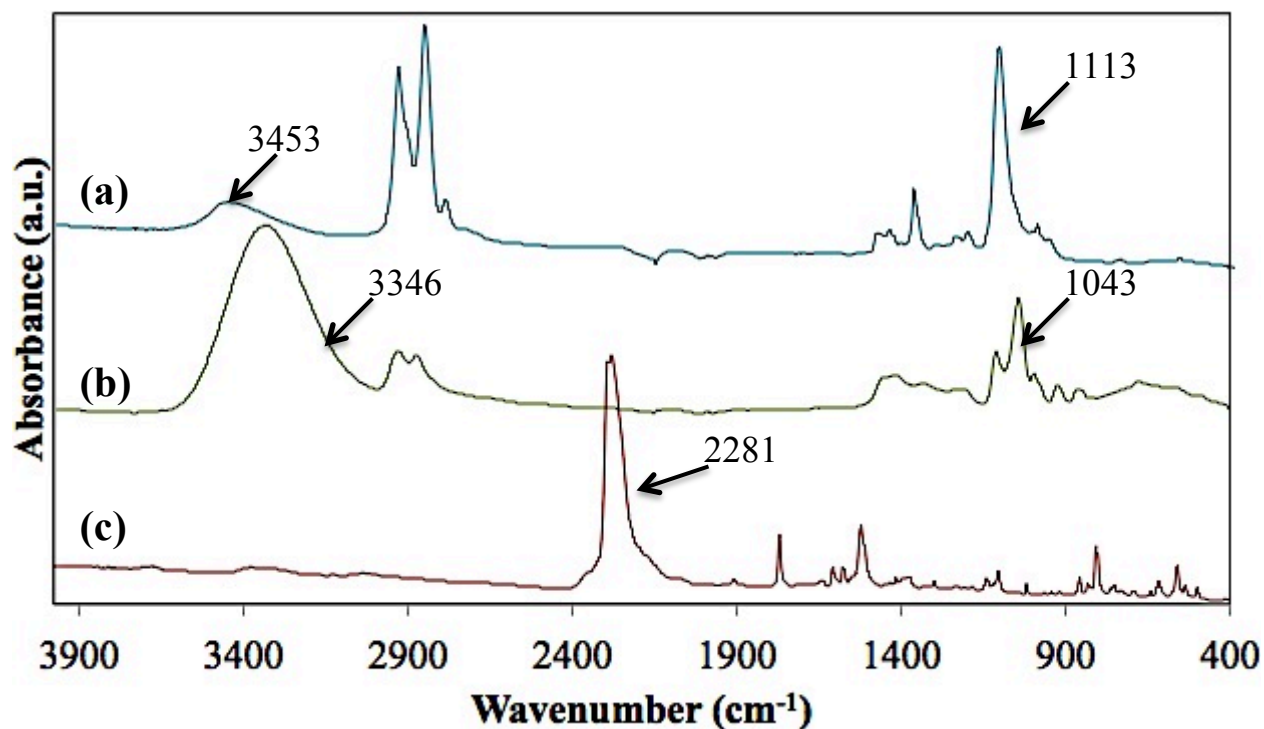


Figure 3.1-1: FTIR of (a) PTHF, (b) glycerin, (c) MDI

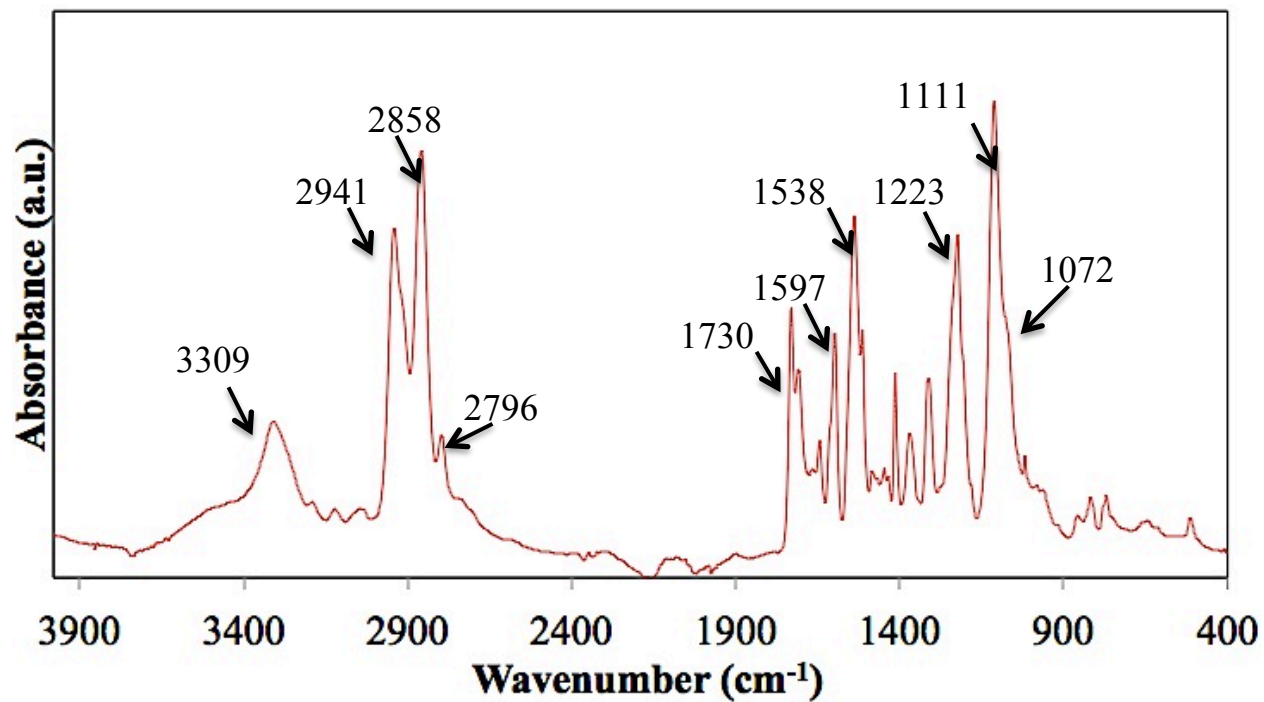


Figure 3.1-2: FTIR spectrum of neat PU

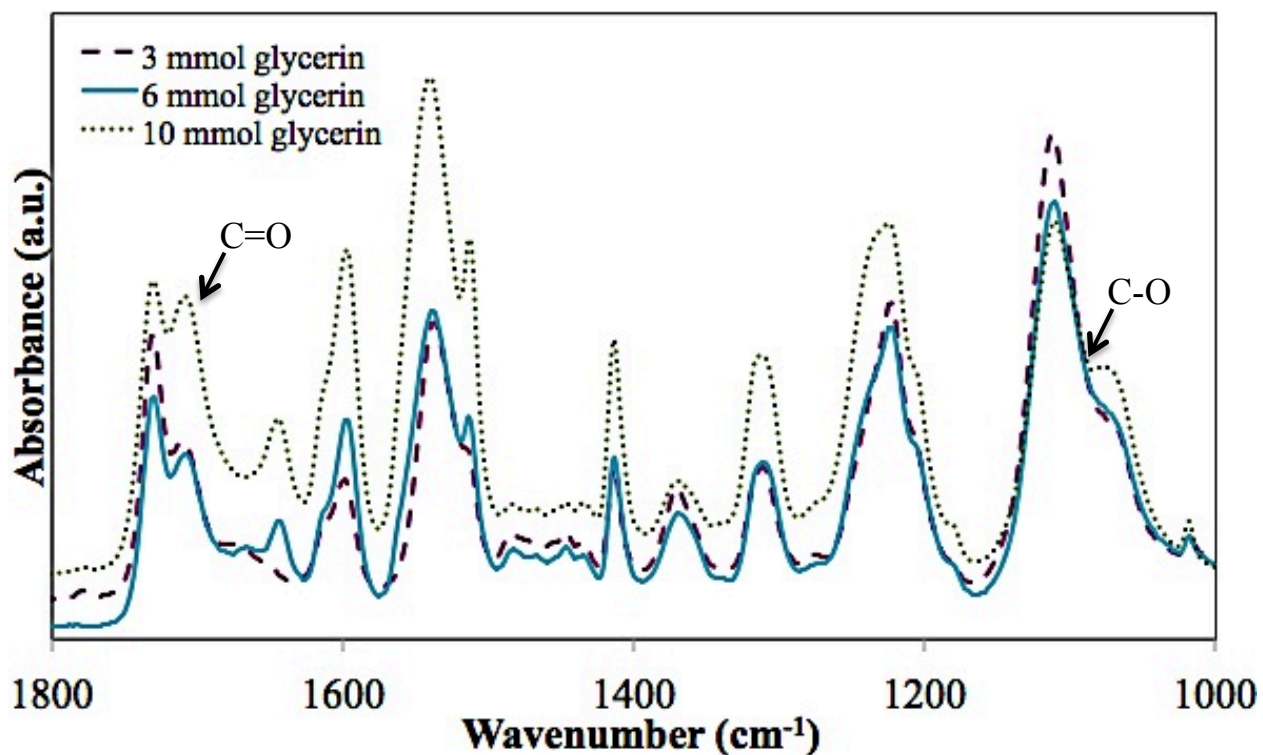


Figure 3.1-4: FTIR of PU crosslinked with varied concentrations of glycerin at low wavenumbers

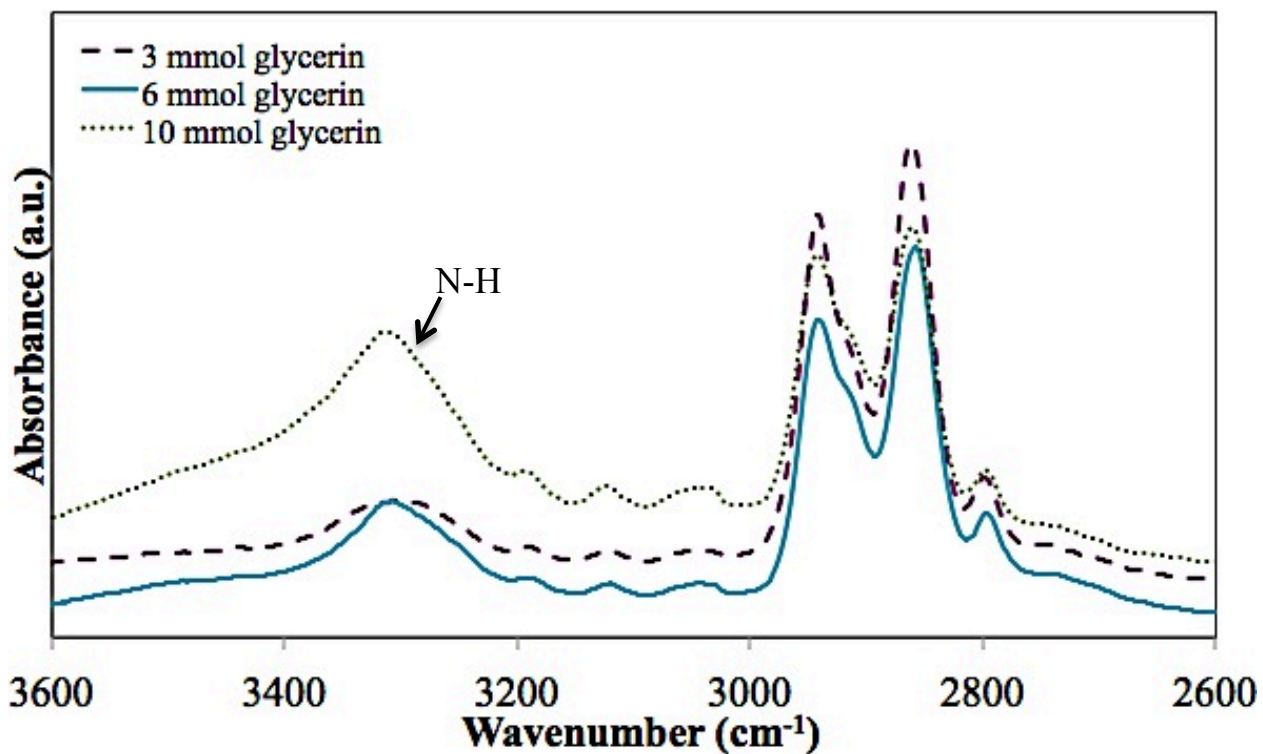


Figure 3.1-5: FTIR of PU crosslinked with varied concentrations of glycerin at high wavenumbers

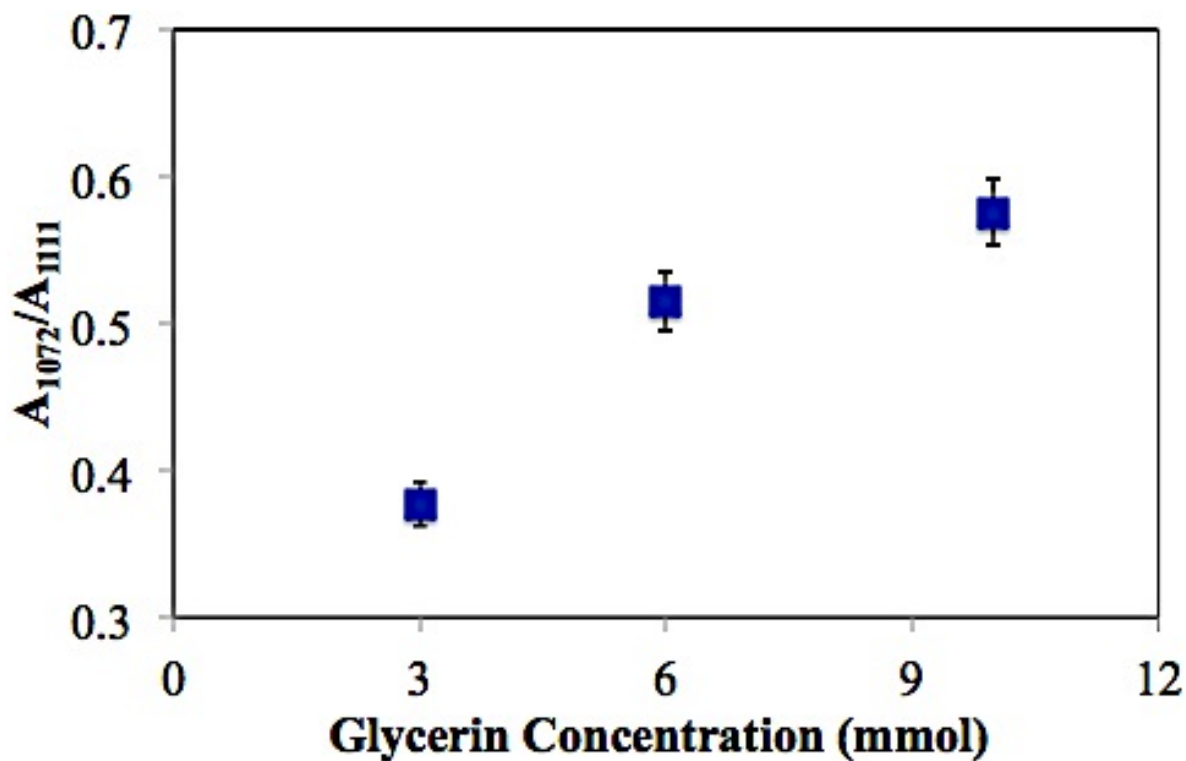


Figure 3.1-6: Effect of glycerin concentration on hard/crosslinking segment C-O peak

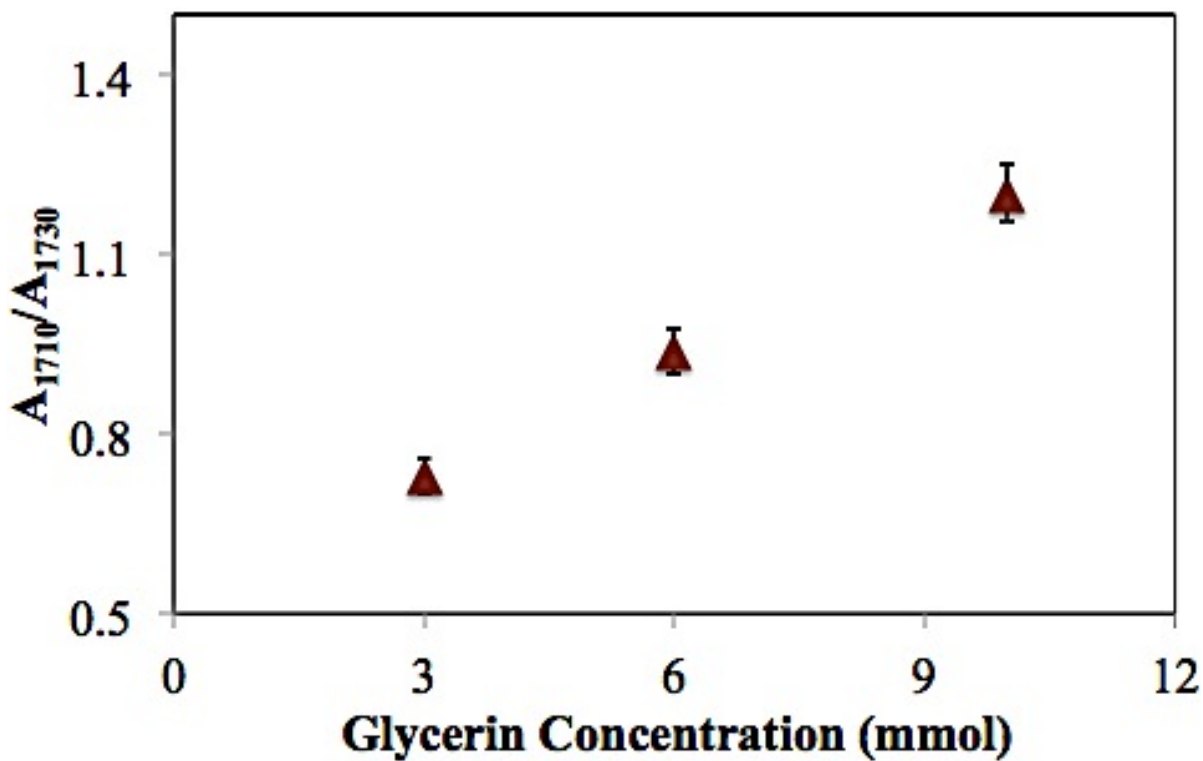


Figure 3.1-7: Effect of glycerin concentration on hard/crosslinking segment C=O (H-bonded) peak

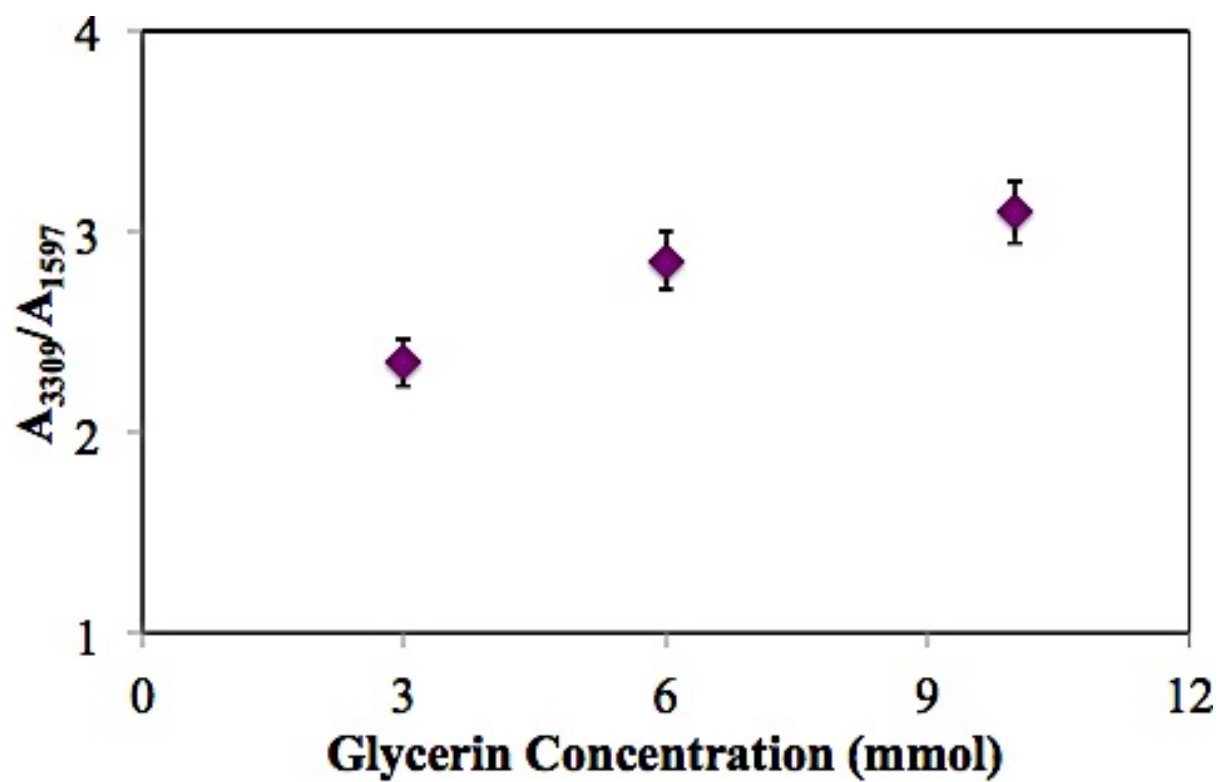


Figure 3.1-8: Effect of glycerin concentration on urethane N-H peak

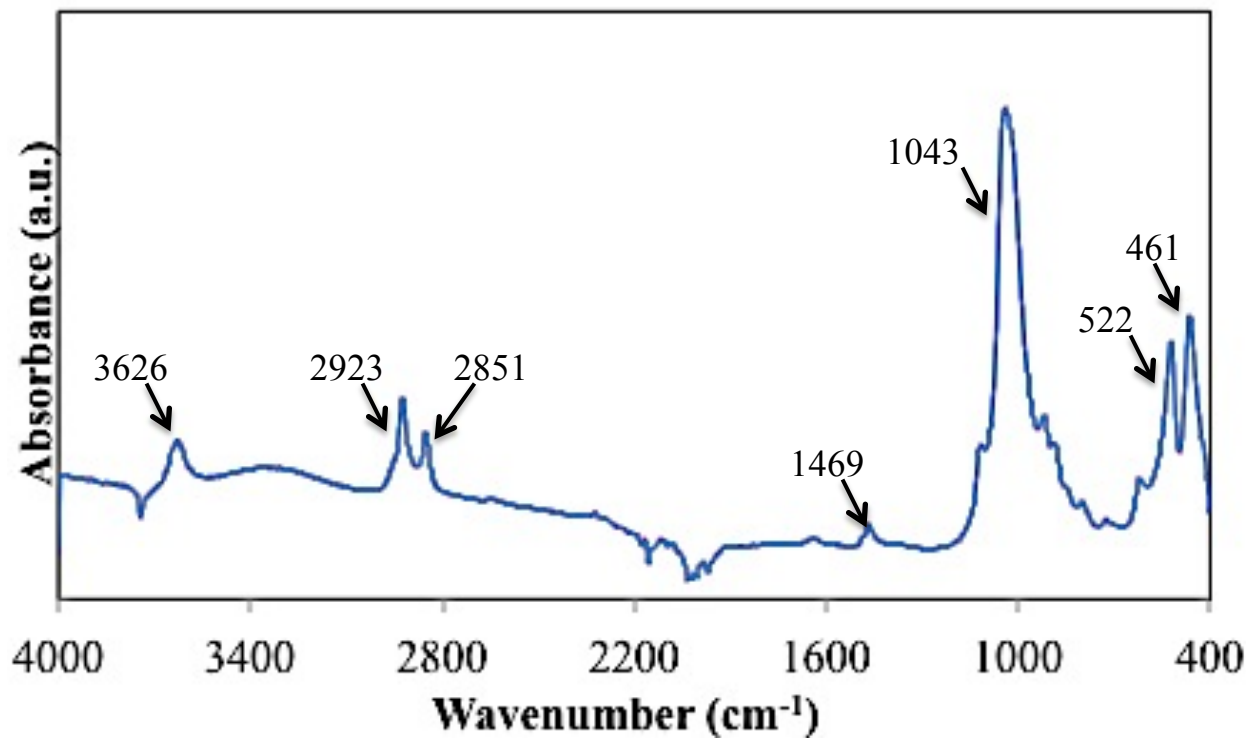


Figure 3.1-9: FTIR spectra of Cloisite 30B clay

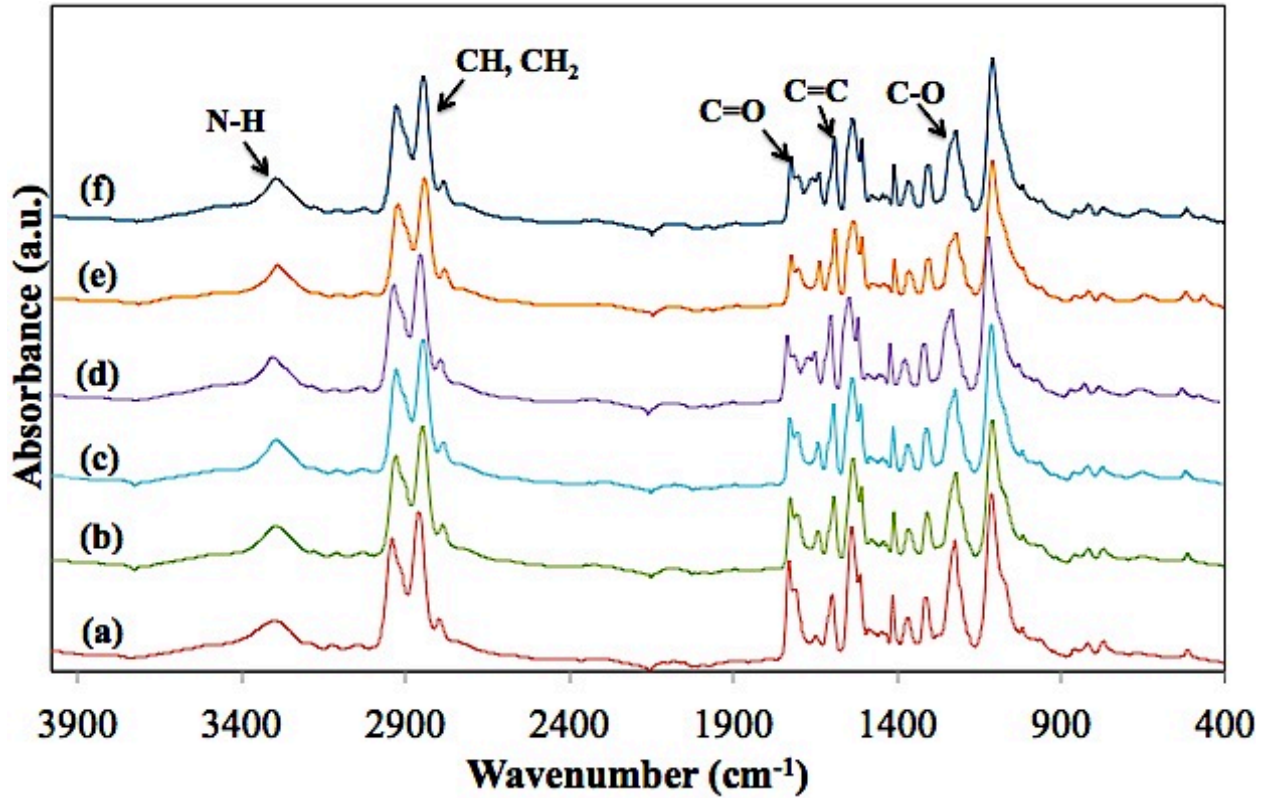


Figure 3.1-10: FTIR spectra of PU nanocomposites with clay loading at (a) 0.25 wt%, (b) 0.5 wt%, (c) 1 wt%, (d) 2 wt%, (e) 5 wt% and (f) 10 wt%

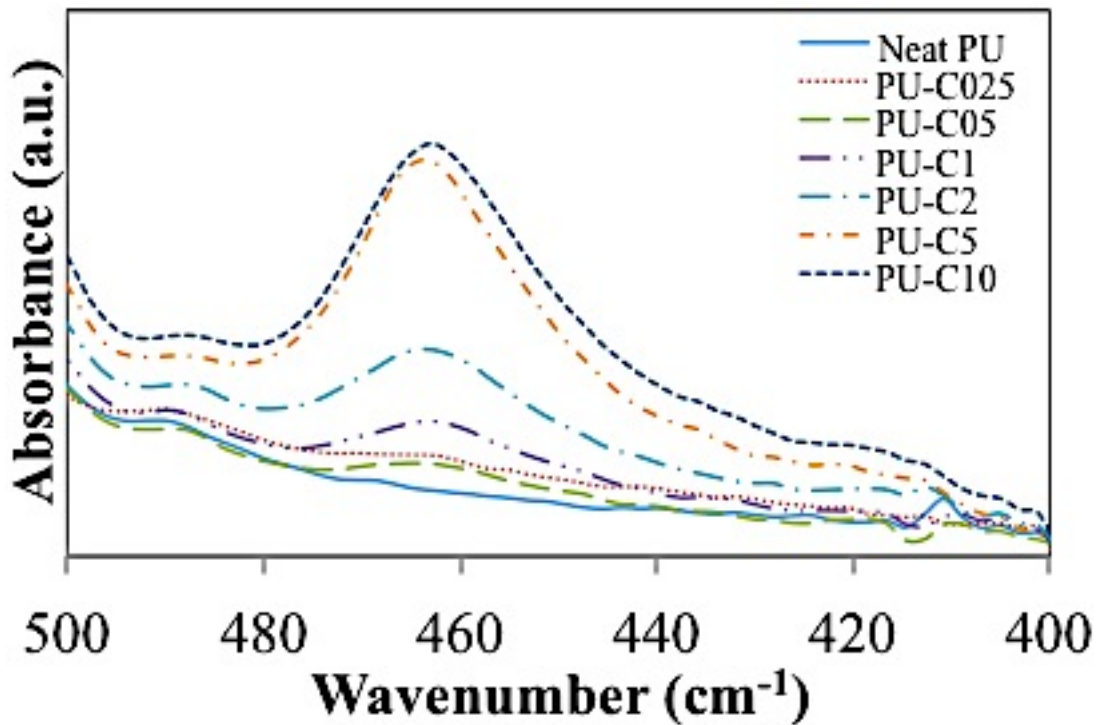


Figure 3.1-11: Close-up of organic moiety clay peak at 461 cm^{-1}

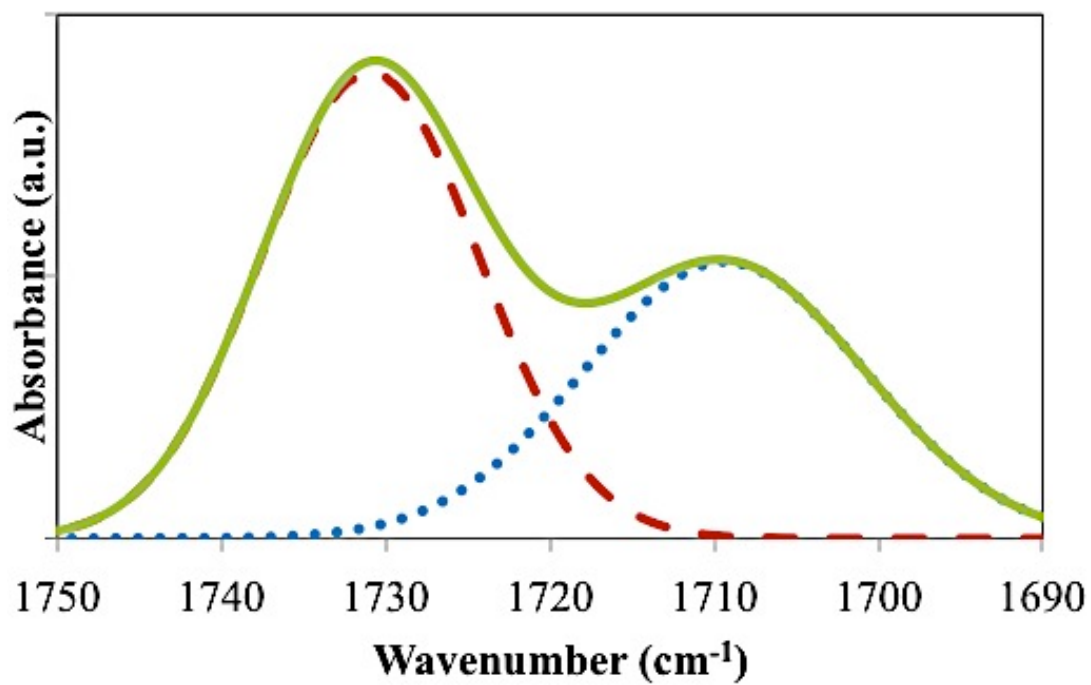


Figure 3.1-12: Deconvolution of 1730 cm⁻¹ (free C=O group) and 1709 cm⁻¹ (H-bonded C=O) peaks

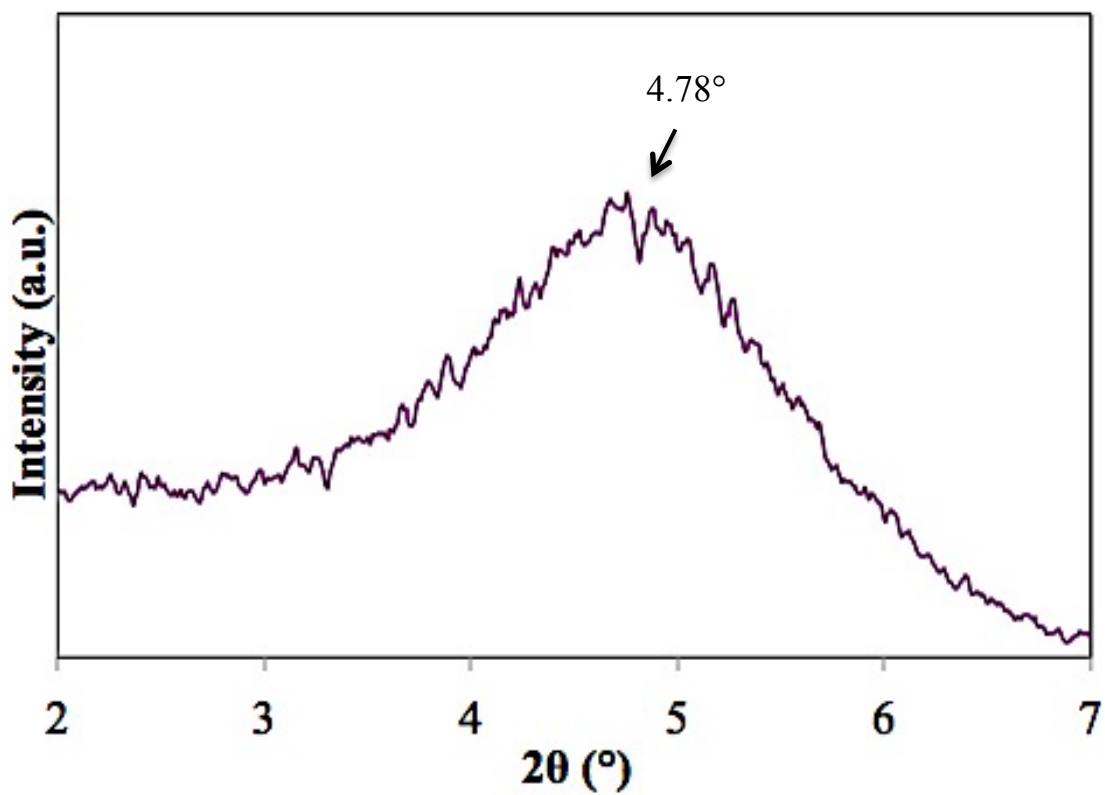


Figure 3.1-13: Diffractogram of Cloisite 30B clay

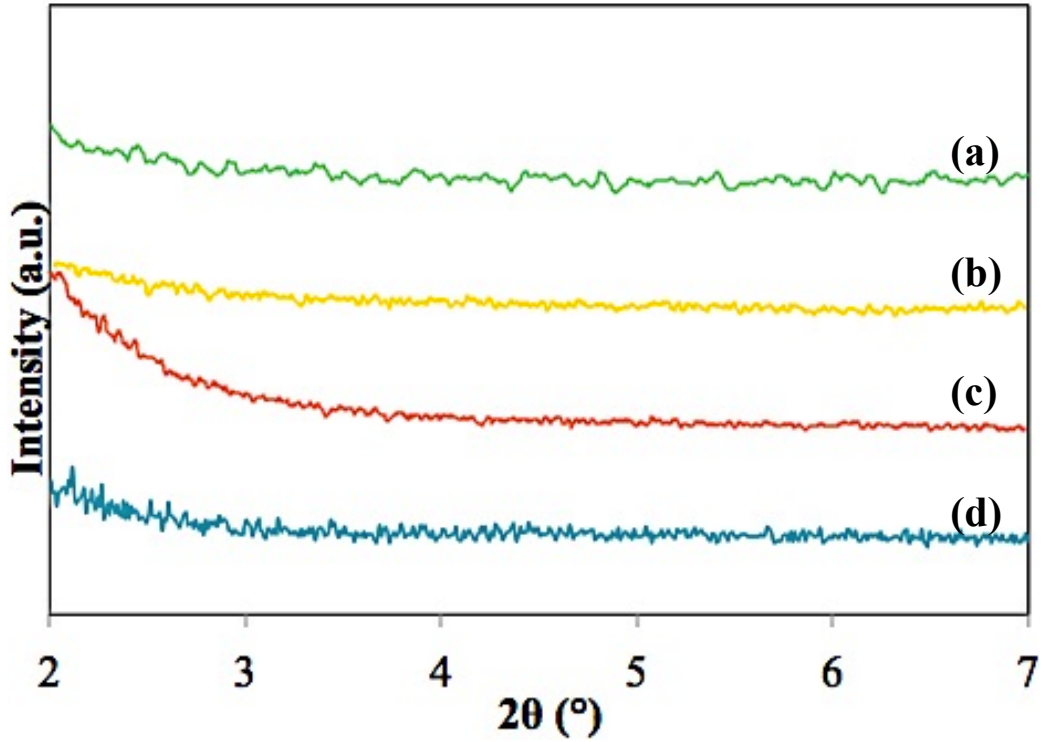


Figure 3.1-14: Diffractogram of (a) neat PU, (b) PU-C025, (c) PU-C05 and (d) PU-C1

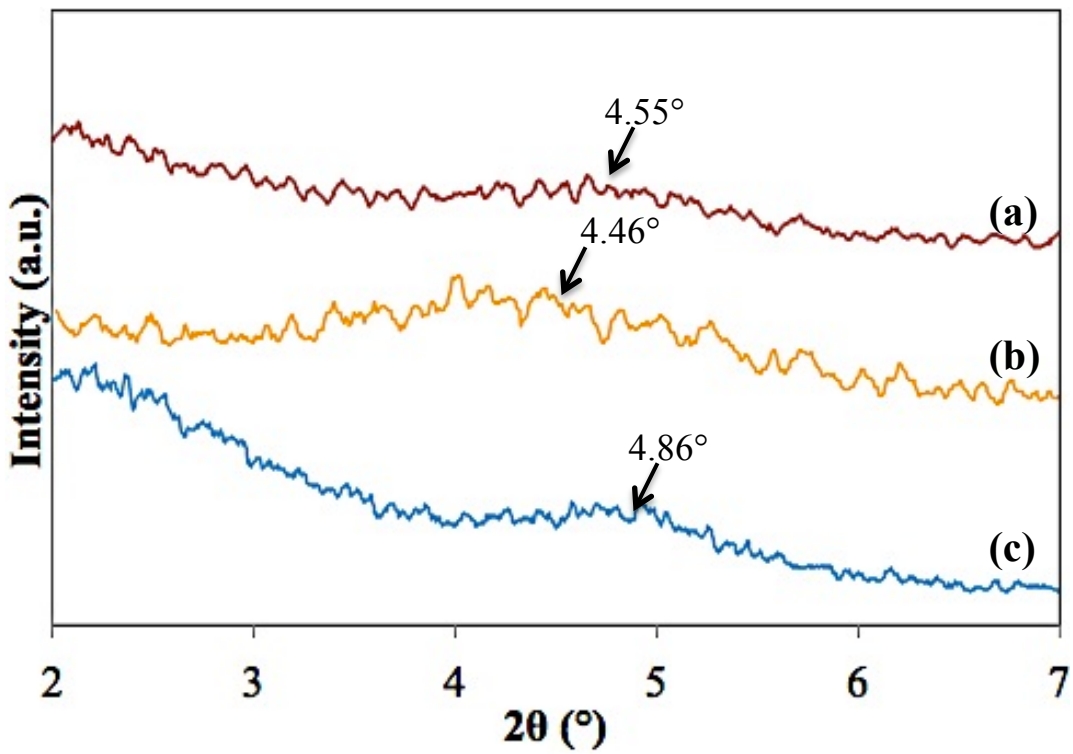


Figure 3.1-15: Diffractogram of (a) PU-C2 (b) PU-C5 and (c) PU-C10

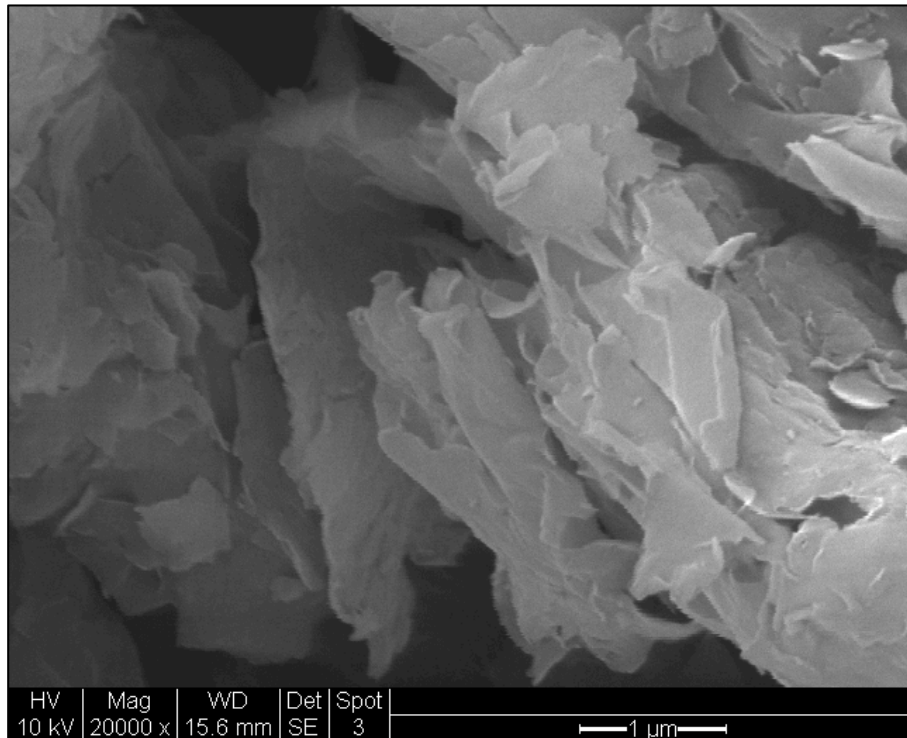
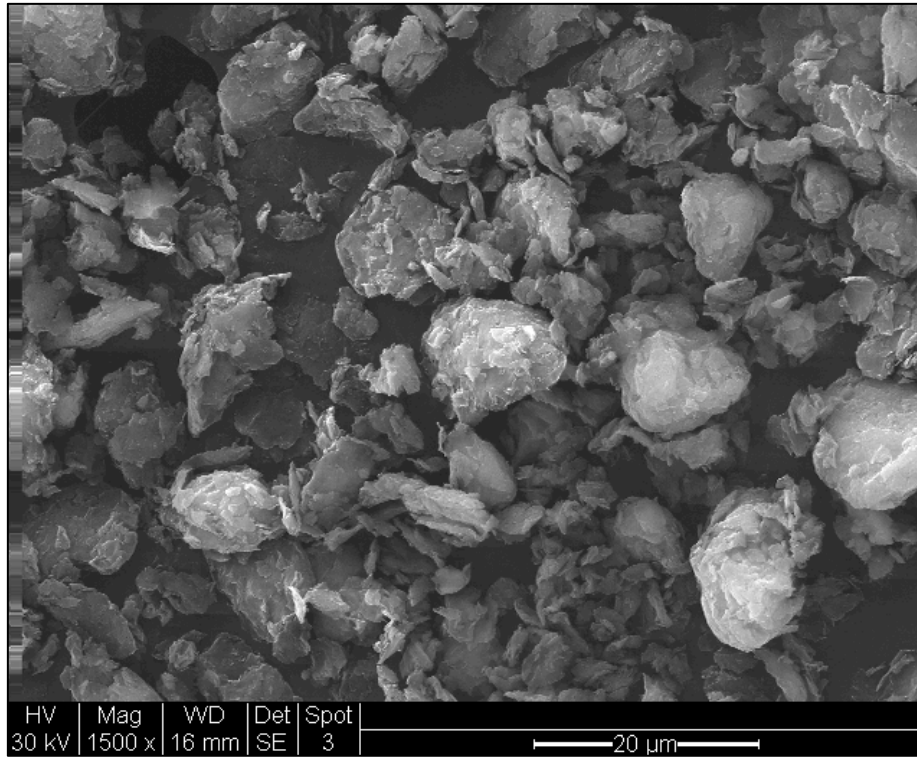


Figure 3.1-16: SEM image of C30B powder at (a) 1500x and (b) 20kx

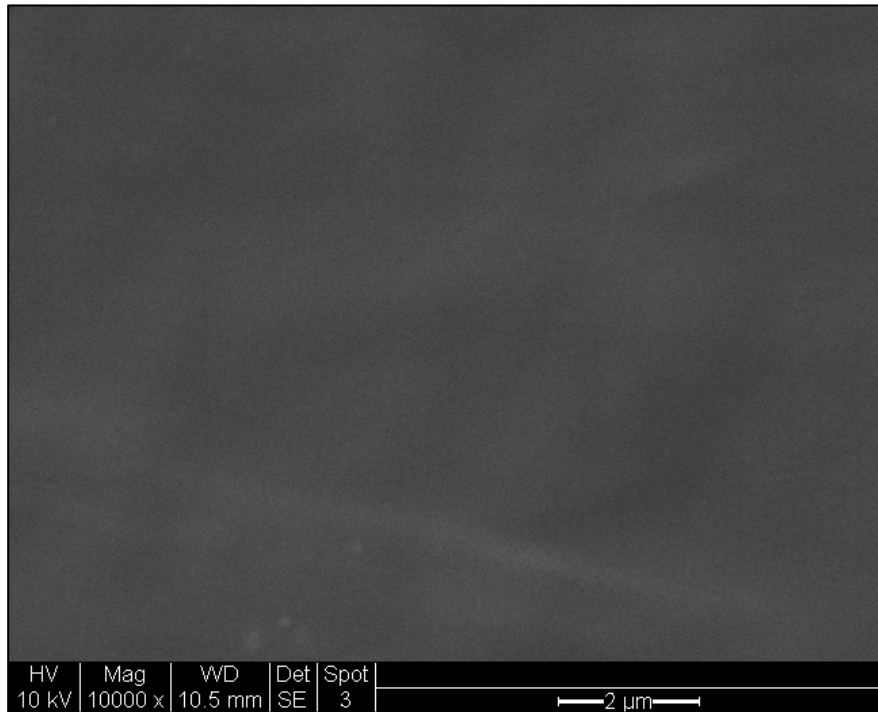
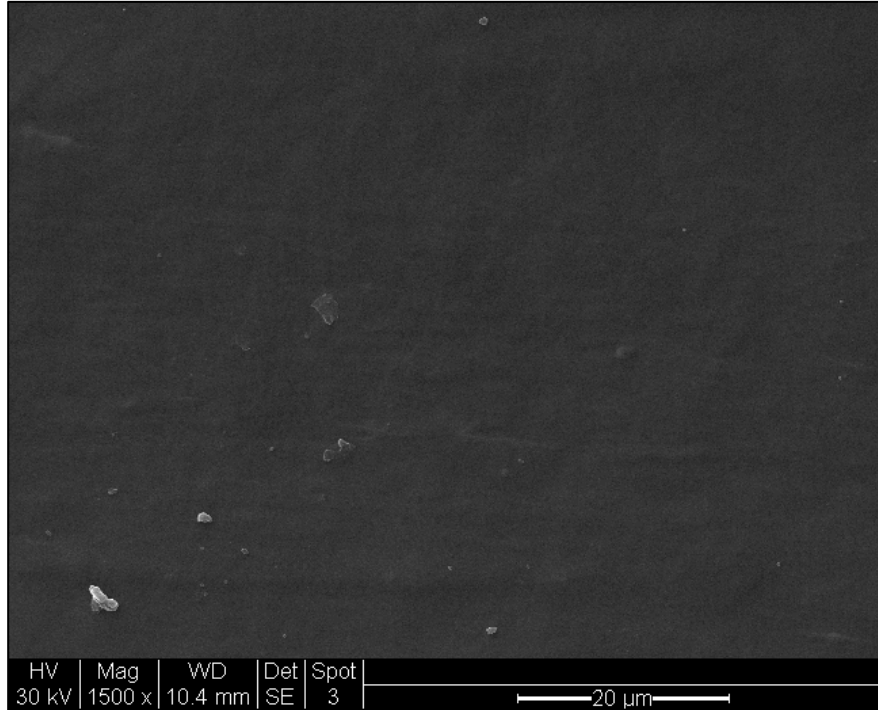


Figure 3.1-17: Cross-sectional SEM image of neat PU at (a) 1500x and (b) 10kx

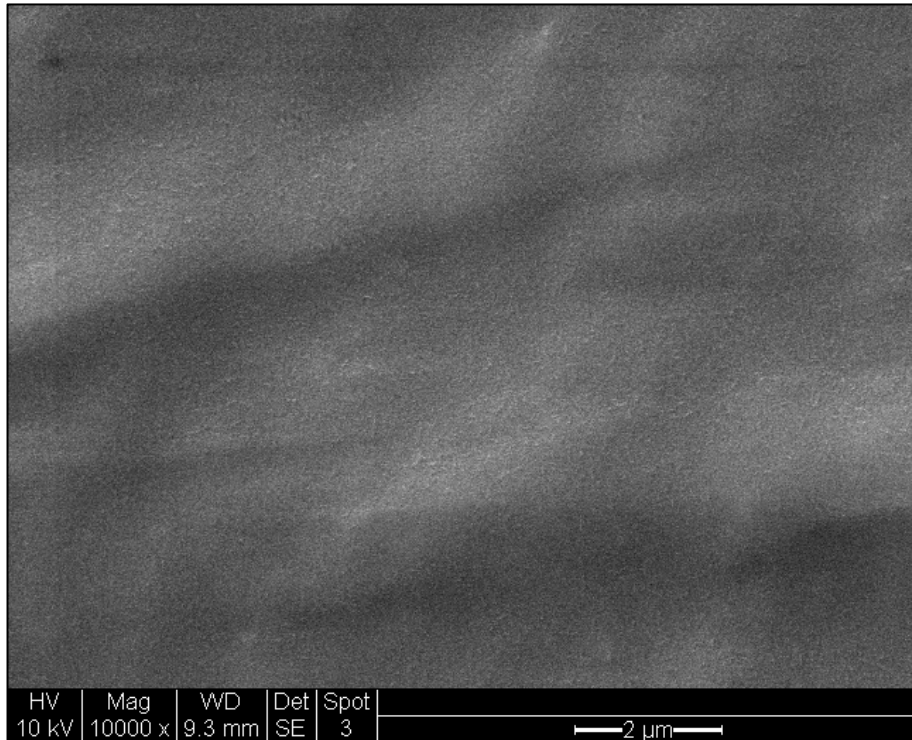
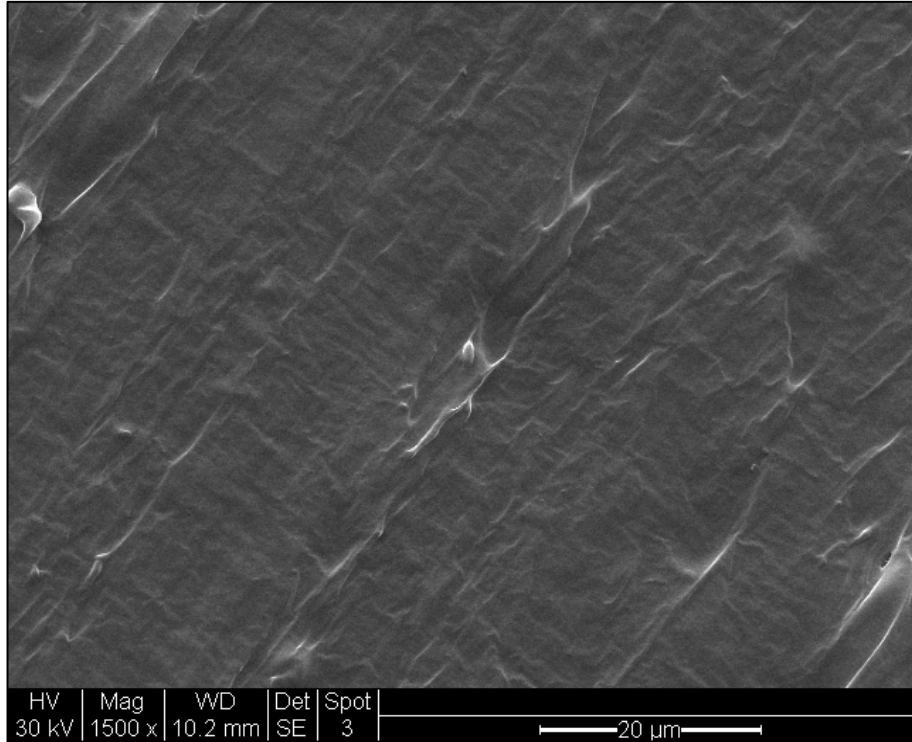


Figure 3.1-18: Cross-sectional SEM images of PU-C025 at (a) 1500x and (b) 10kx

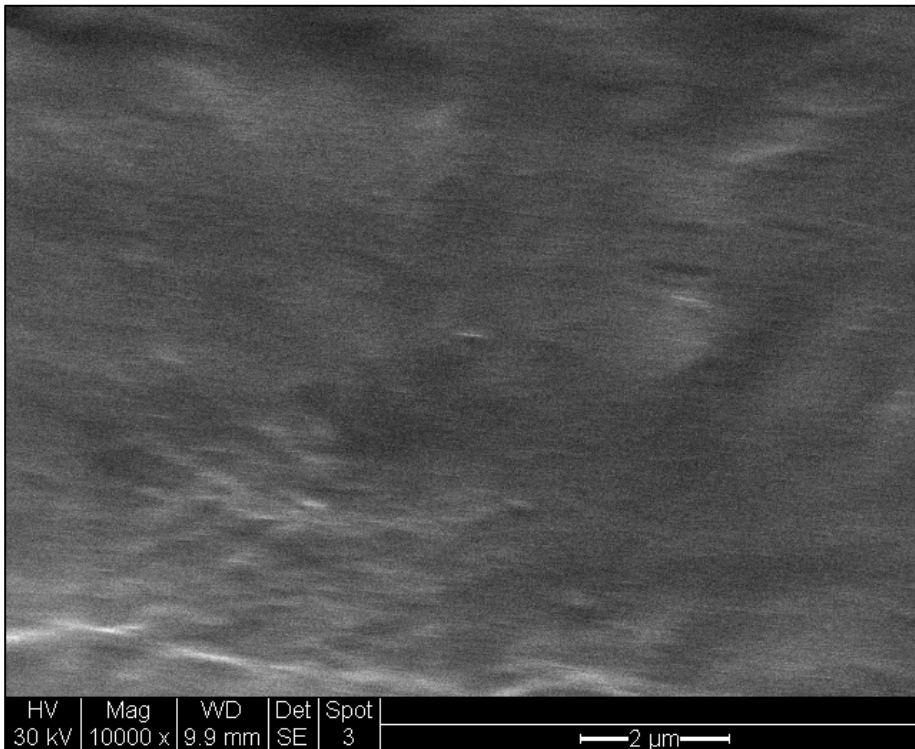
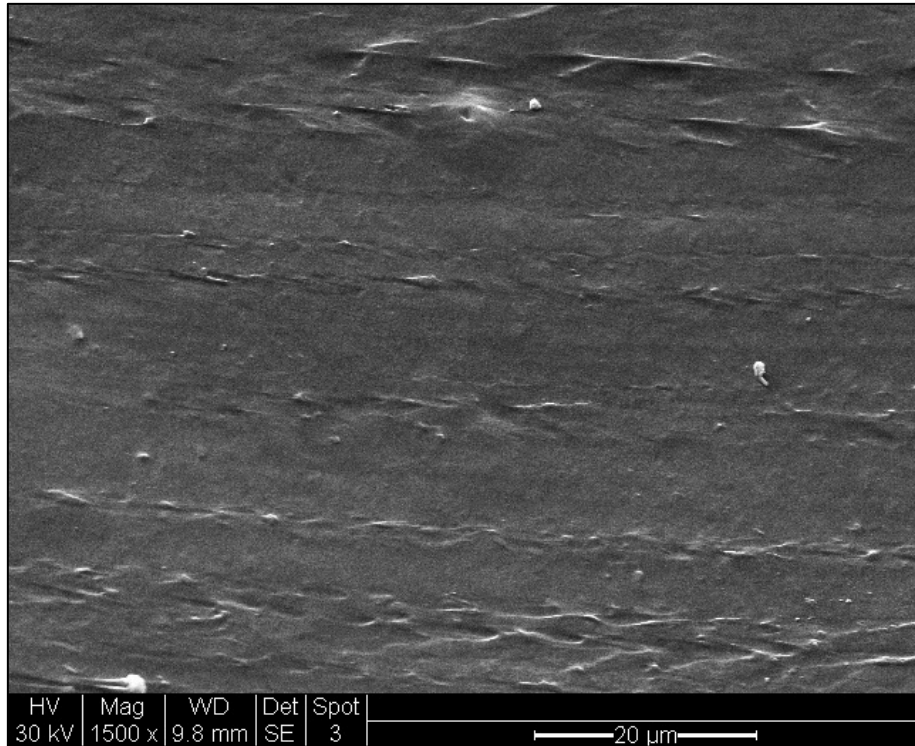


Figure 3.1-19: Cross-sectional SEM images of PU-C05 at (a) 1500x and (b) 10kx

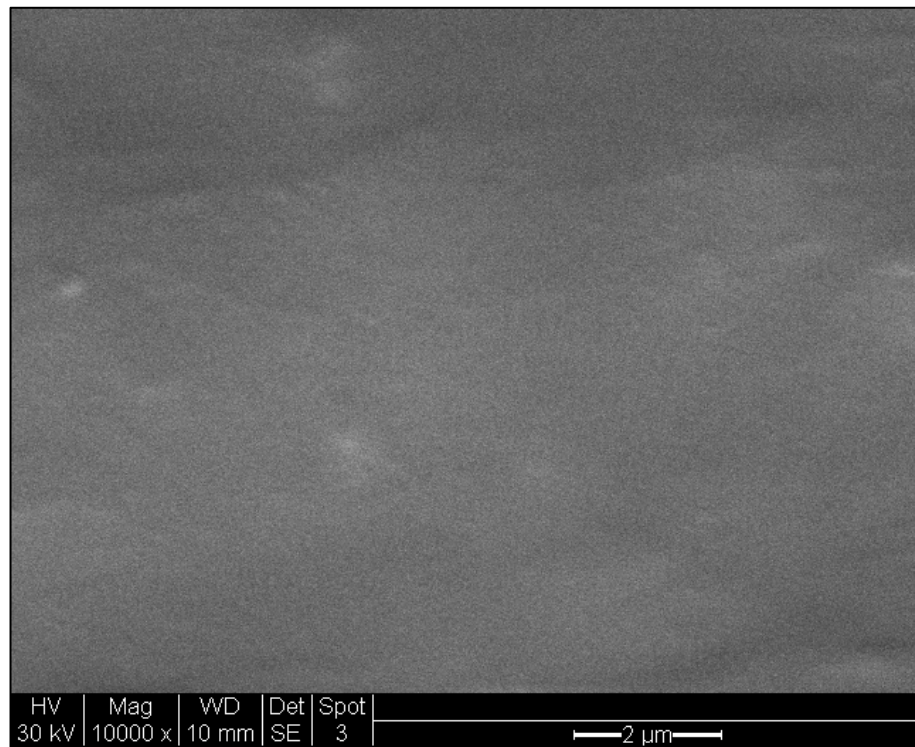
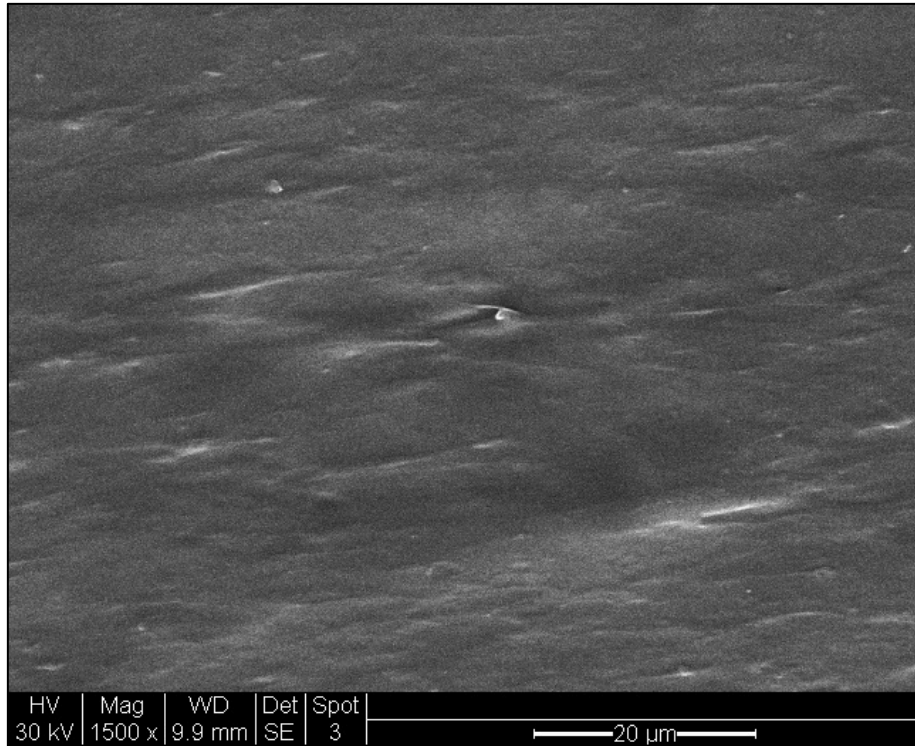


Figure 3.1-20: Cross-sectional SEM images of PU-C1 at (a) 1500x and (b) 10kx

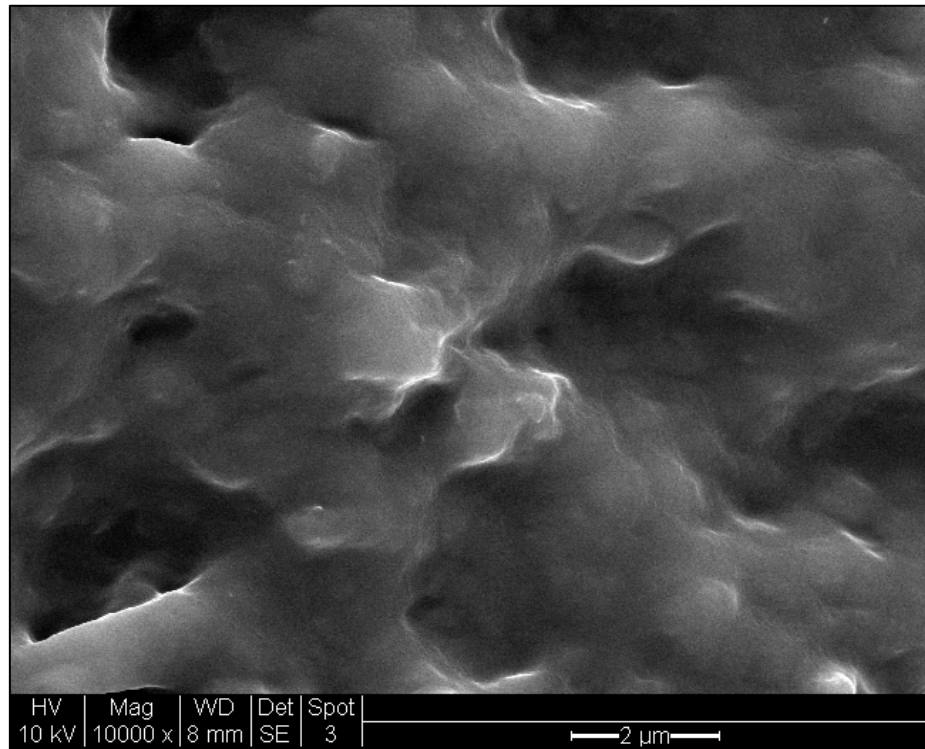
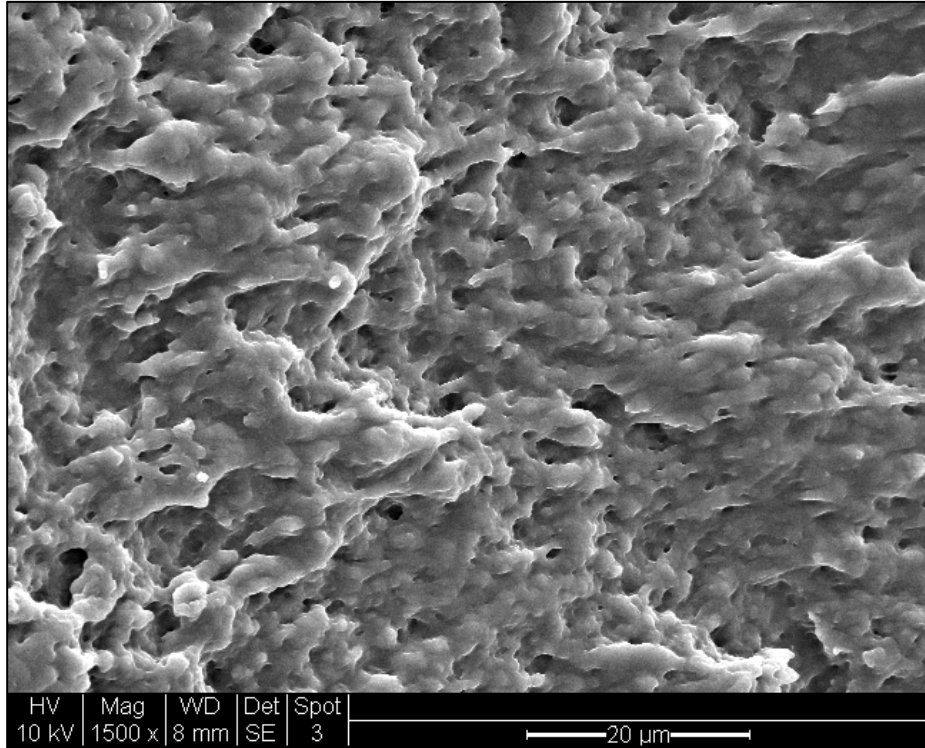


Figure 3.1-21: Cross-sectional SEM images of PU-C2 at (a) 1500x and (b) 10kx

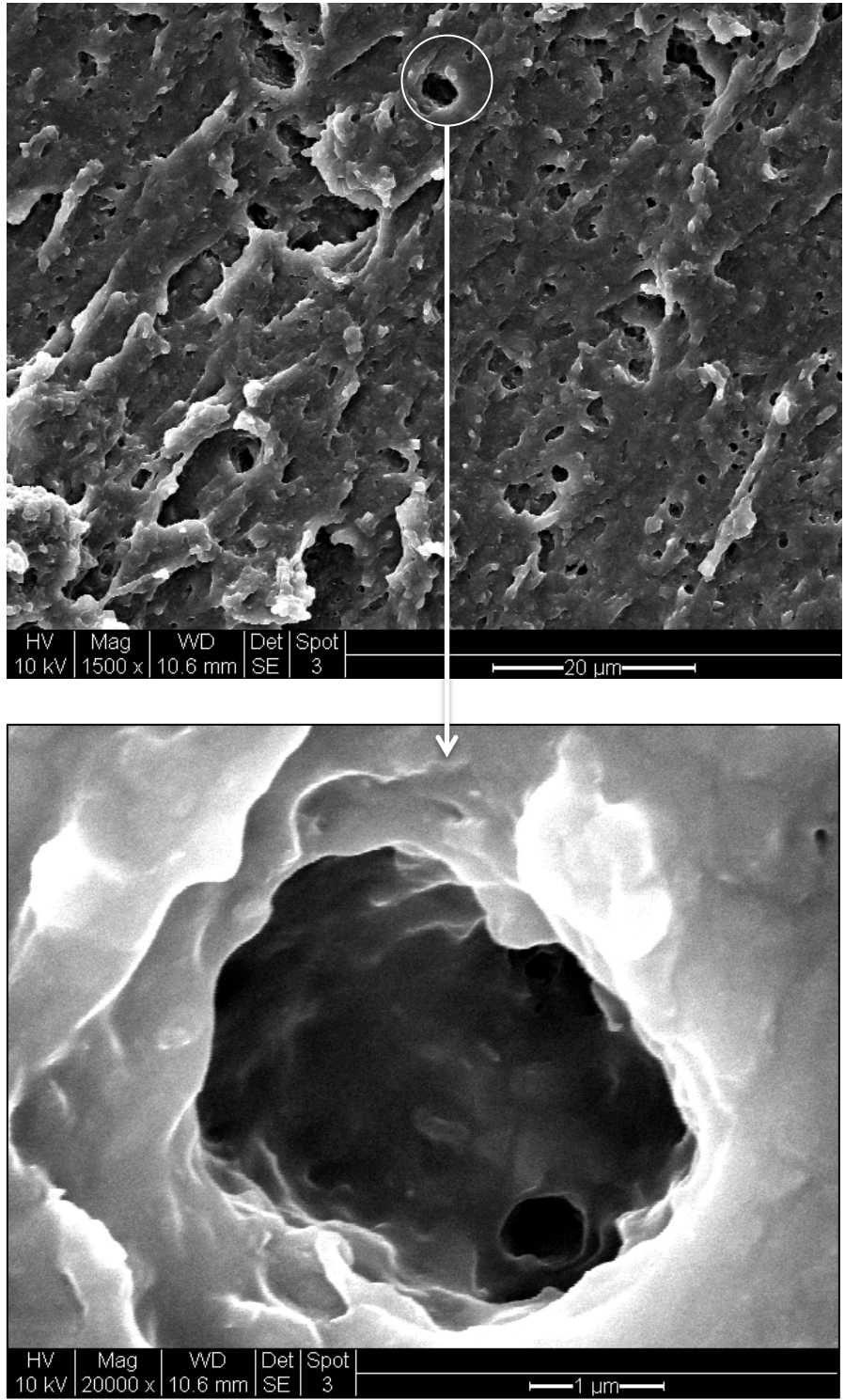


Figure 3.1-22: Cross-sectional SEM images of PU-C5 at (a) 1500x and (b) 20kx

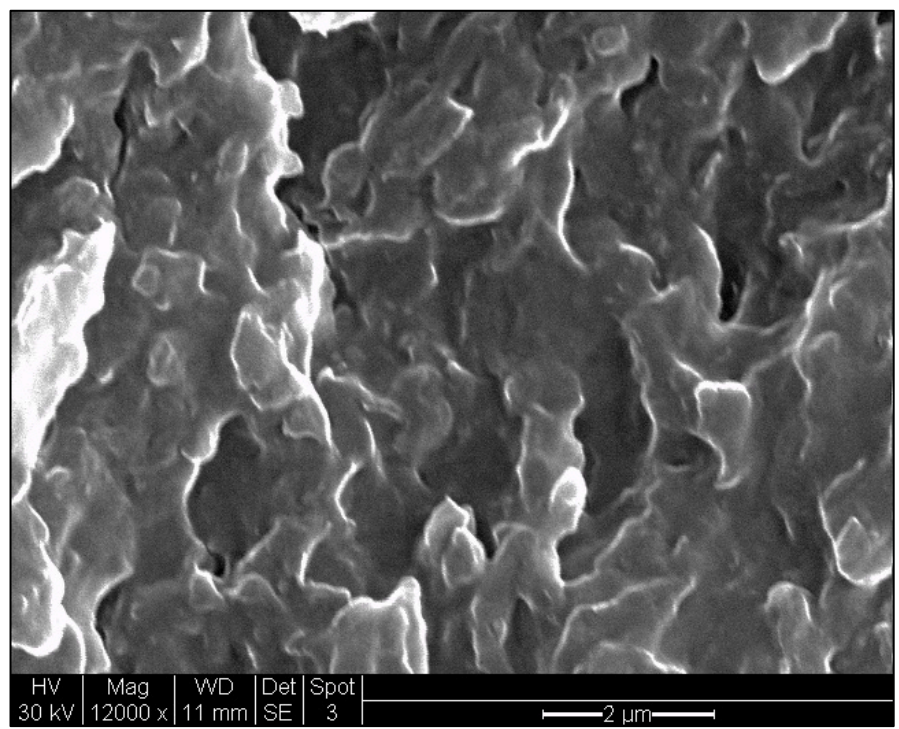
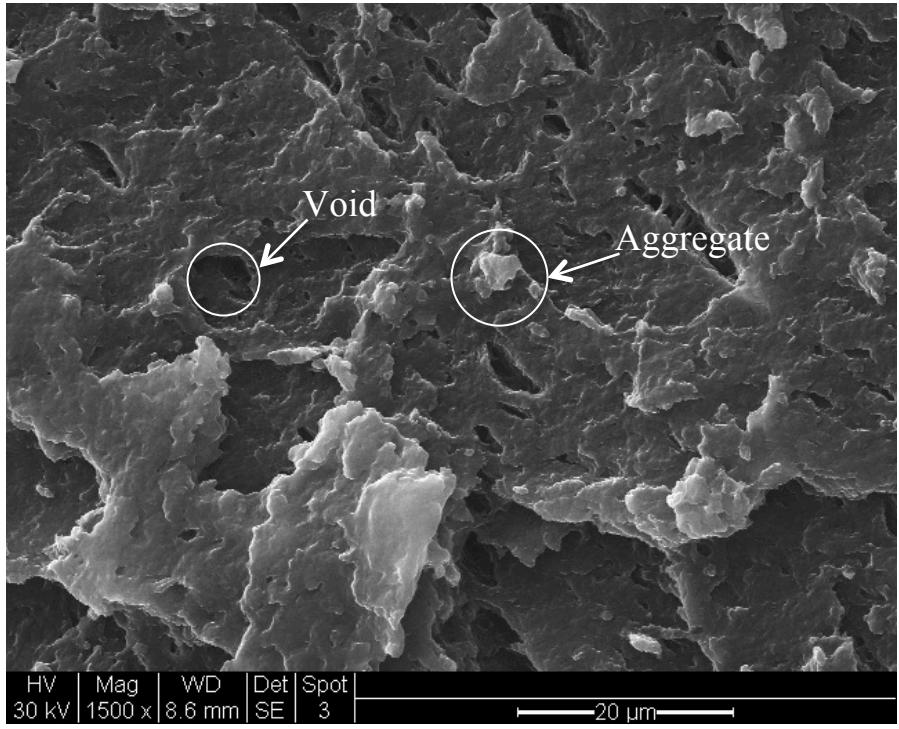


Figure 3.1-23: Cross-sectional SEM images of PU-C10 at (a) 1500x and (b) 12kx

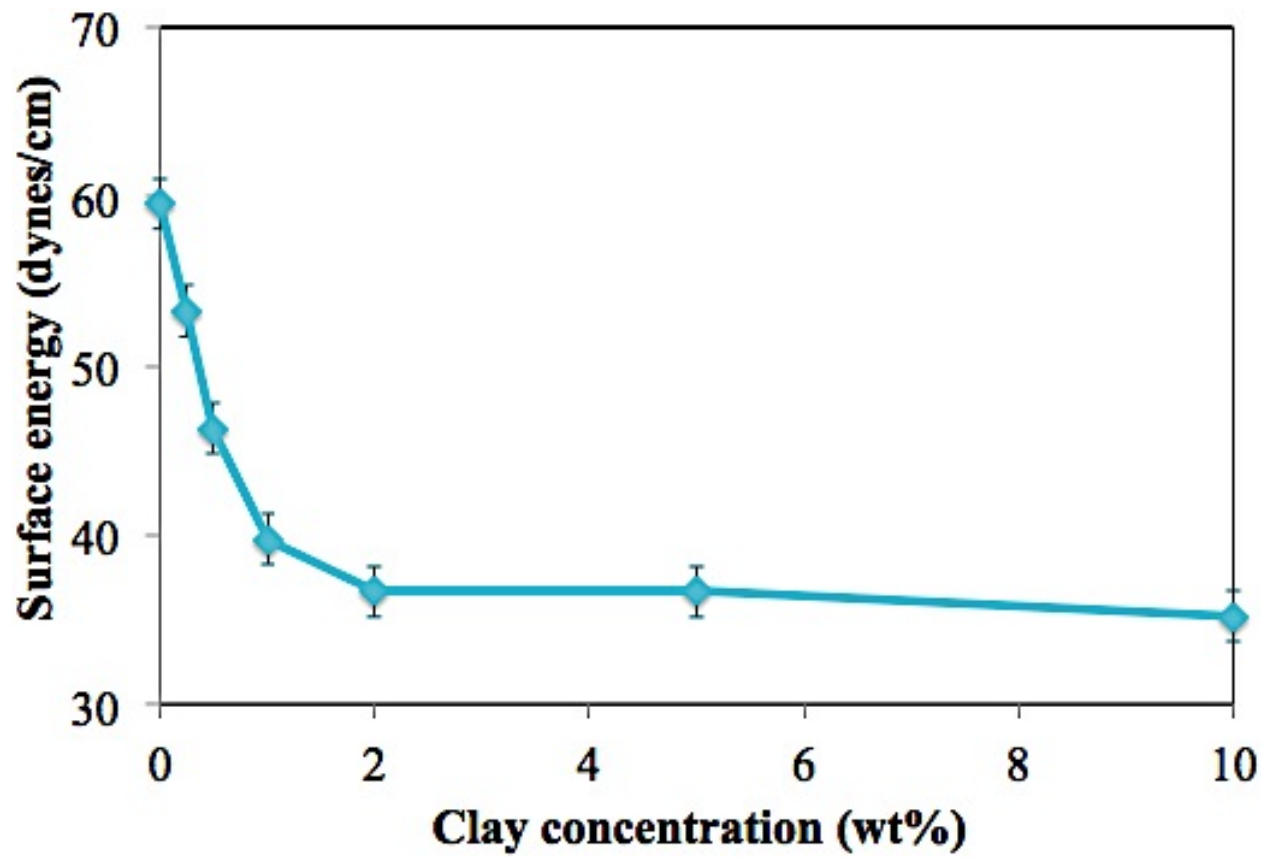


Figure 3.1-24: Surface energy of PU as clay concentration is increased

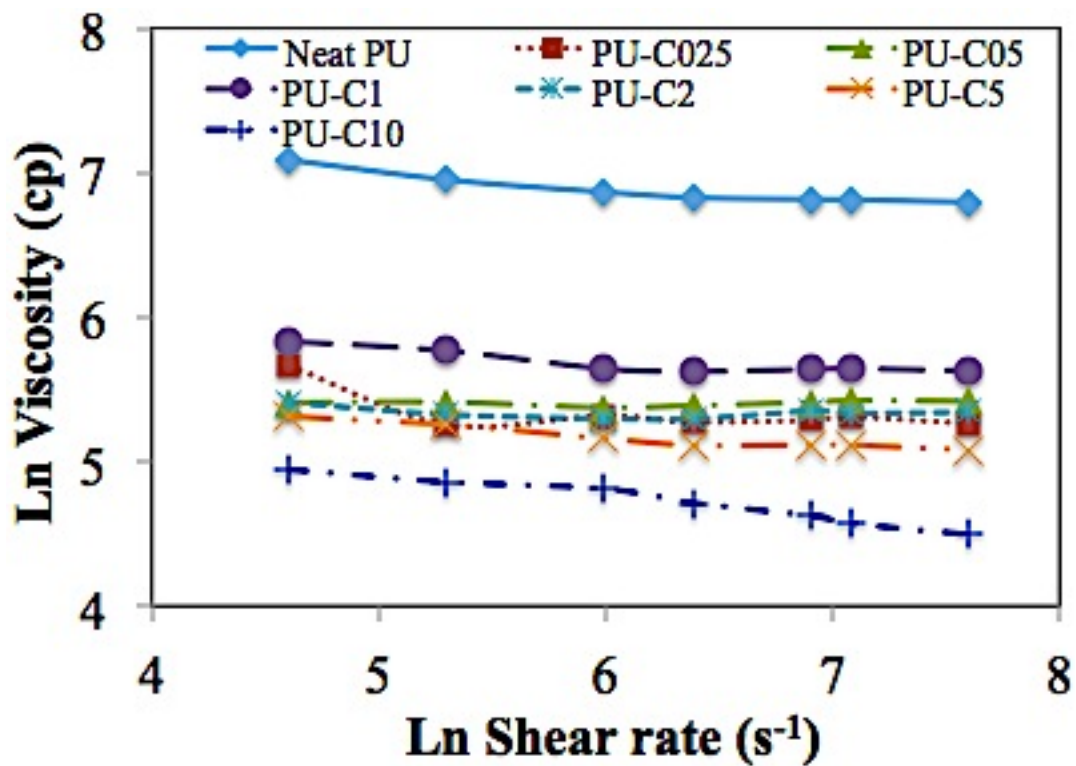


Figure 3.2-1: Effect of clay and shear rate on the viscosity of PU at 25°C

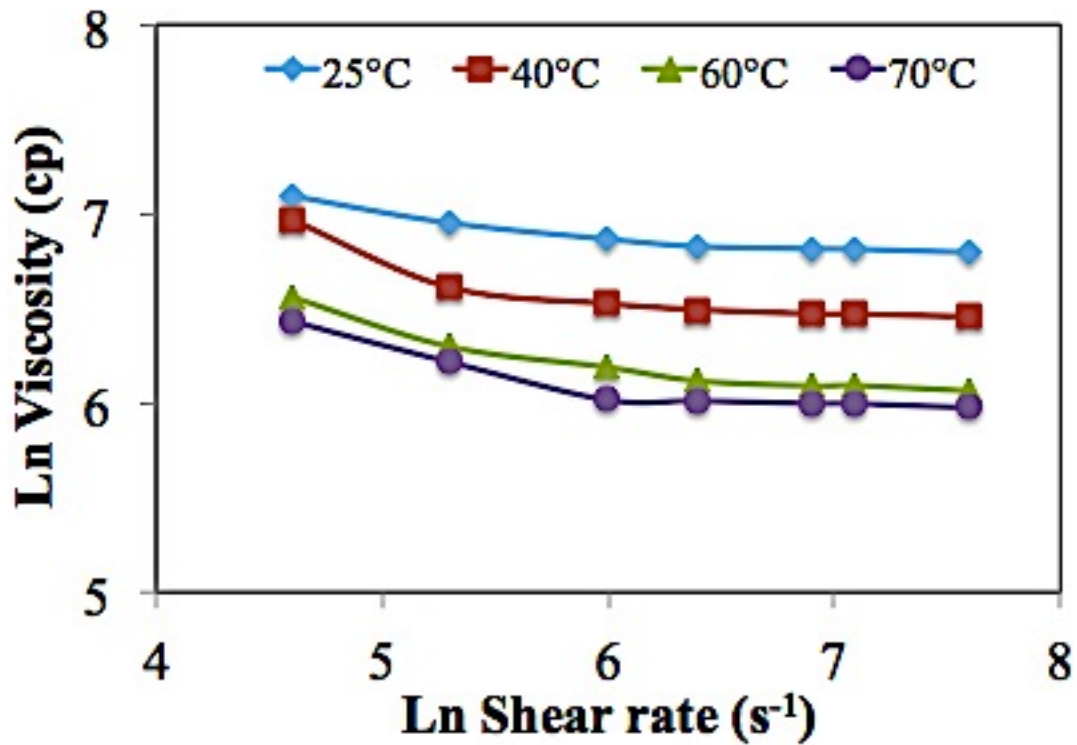


Figure 3.2-2: Viscosity of neat PU as a function of temperature and shear rate

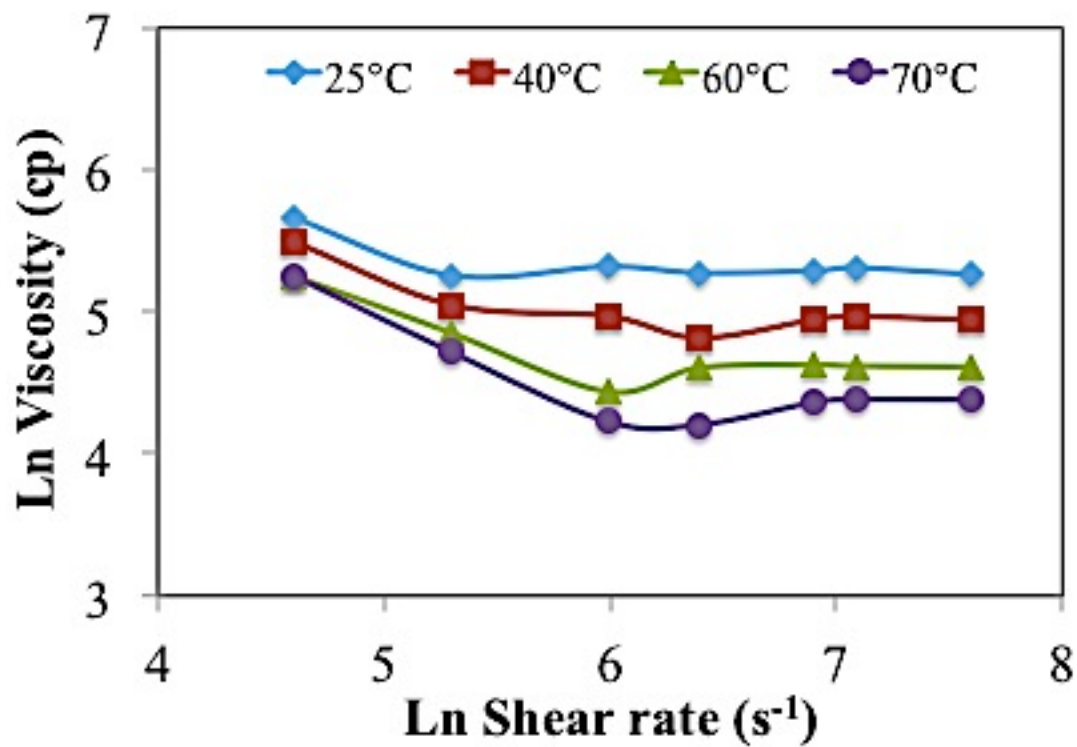


Figure 3.2-3: Viscosity of PU-C025 as a function of temperature and shear rate

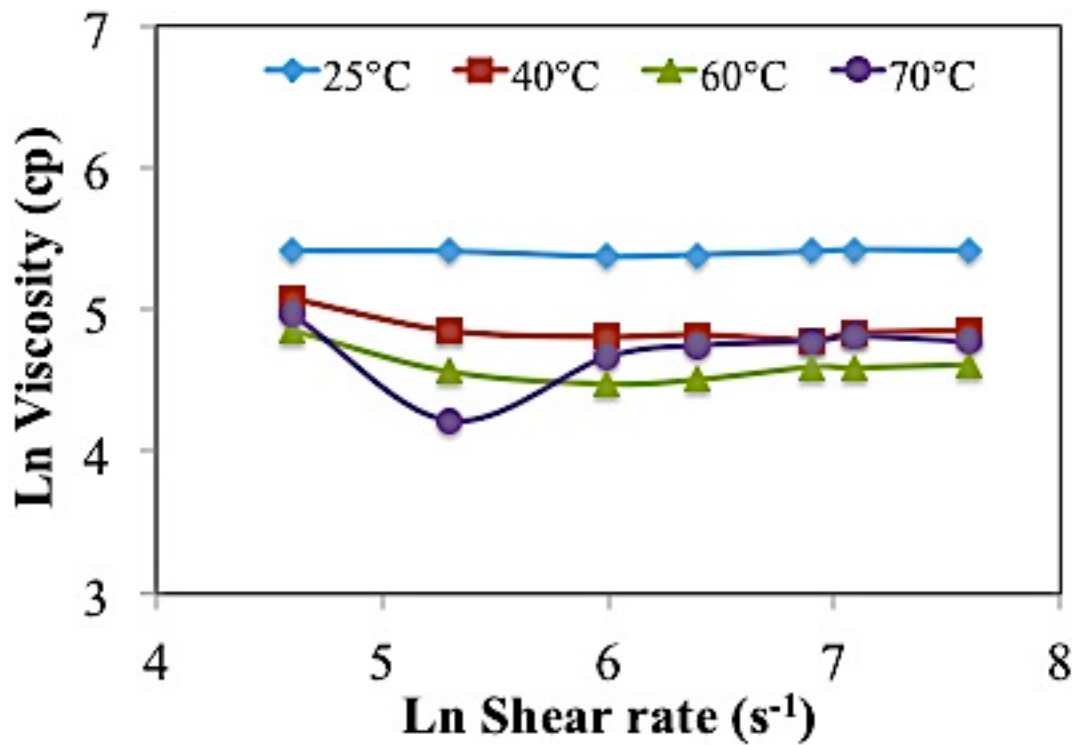


Figure 3.2-4: Viscosity of PU-C05 as a function of temperature and shear rate

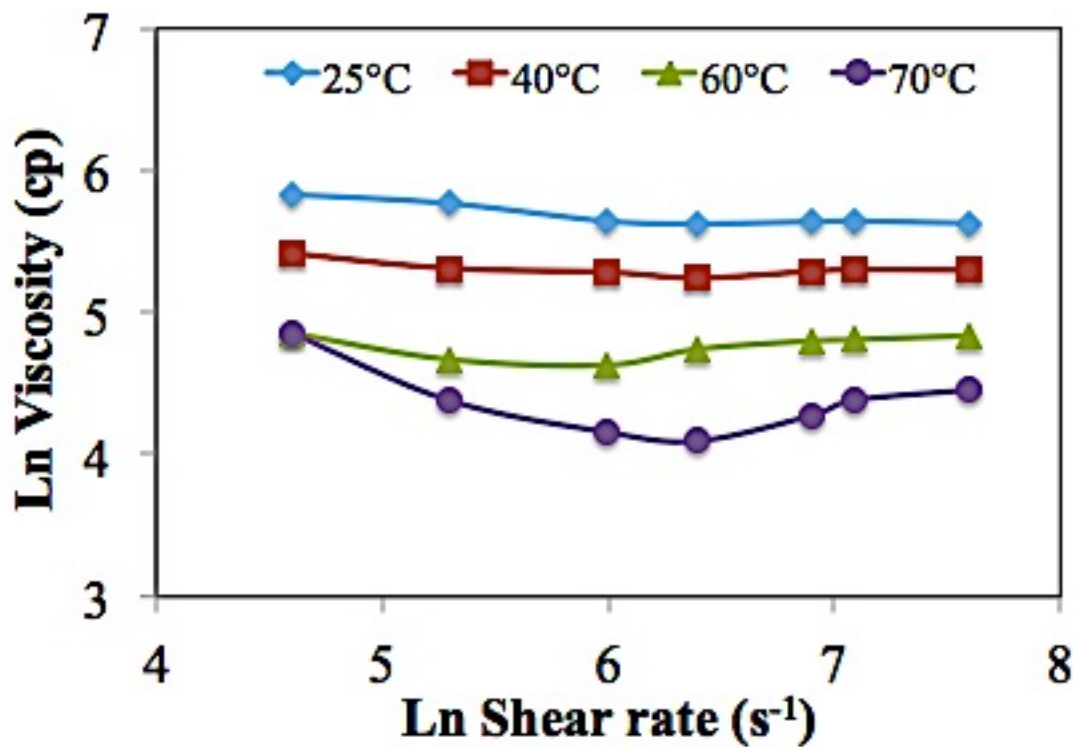


Figure 3.2-5: Viscosity of PU-C1 as a function of temperature and shear rate

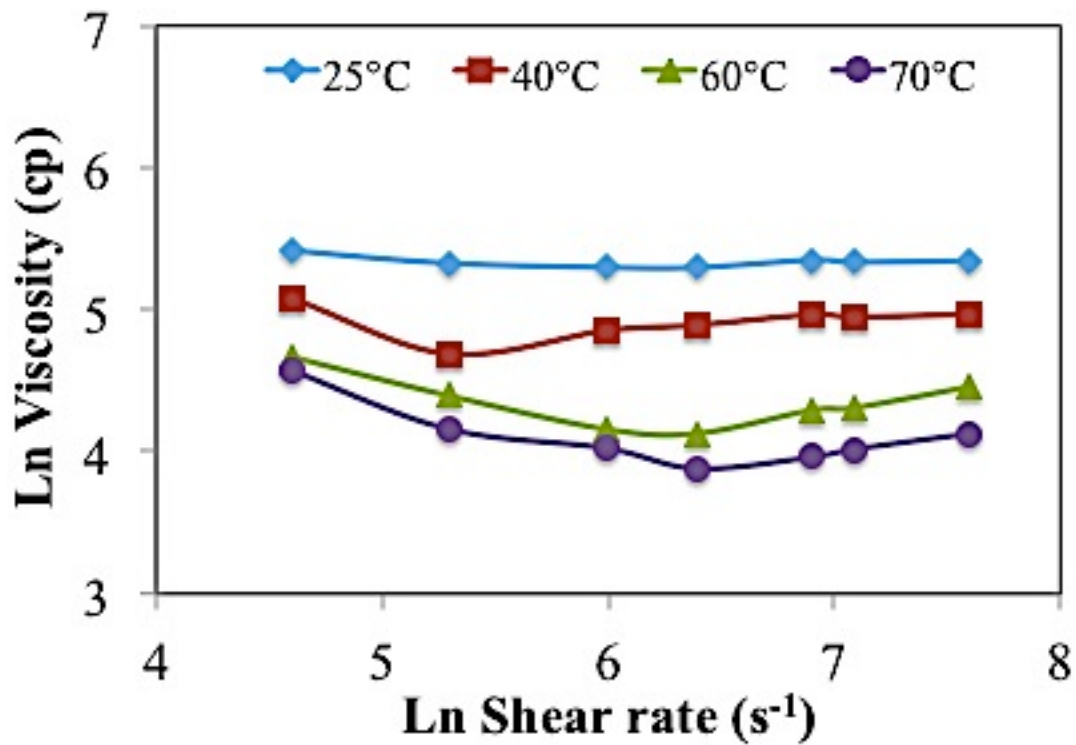


Figure 3.2-6: Viscosity of PU-C2 as a function of temperature and shear rate

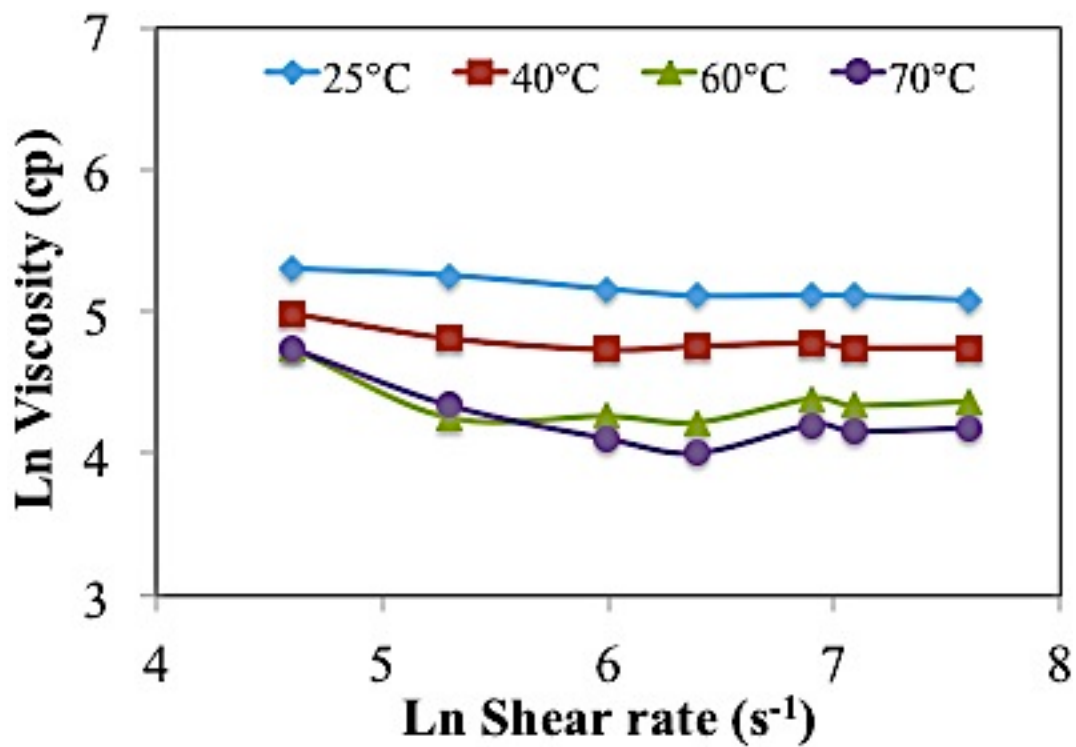


Figure 3.2-7: Viscosity of PU-C5 as a function of temperature and shear rate

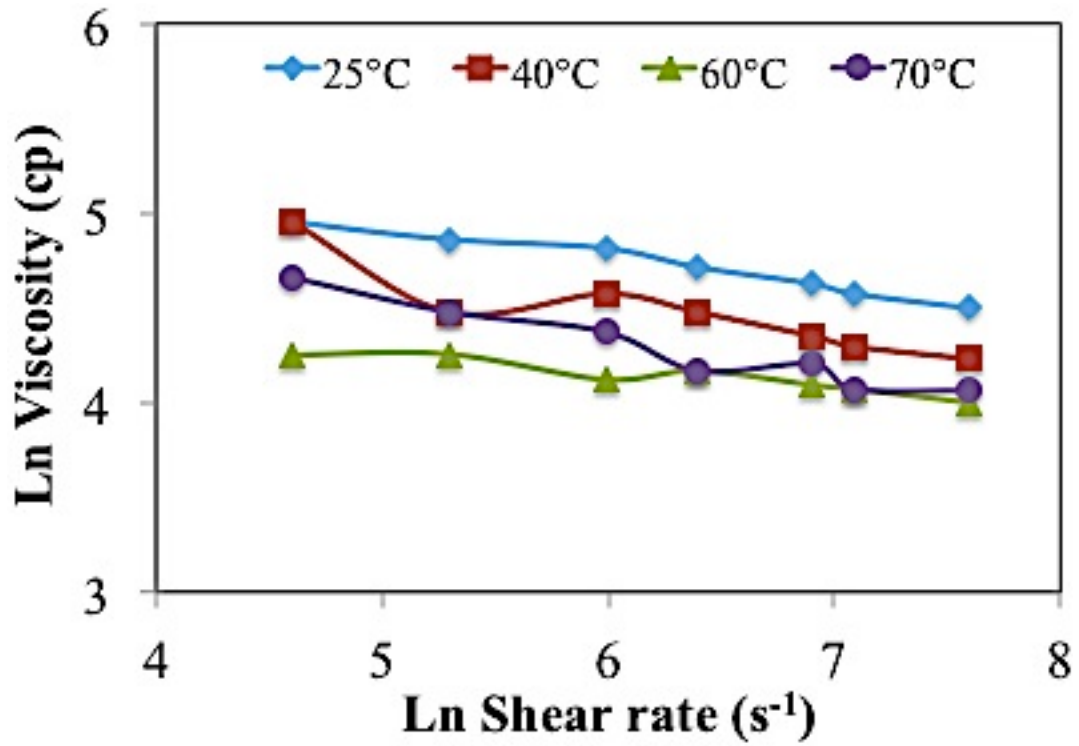


Figure 3.2-8: Viscosity of PU-C10 as a function of temperature and shear rate

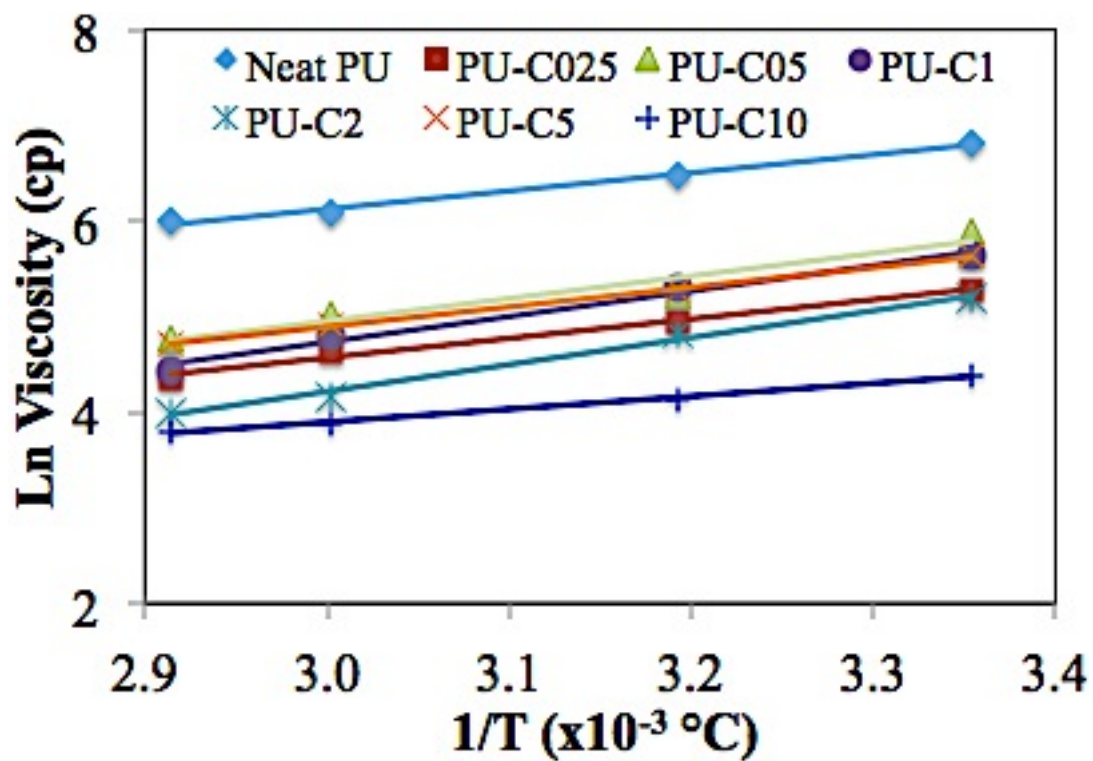


Figure 3.2-9: Change in viscosity at constant shear rate as a function of temperature

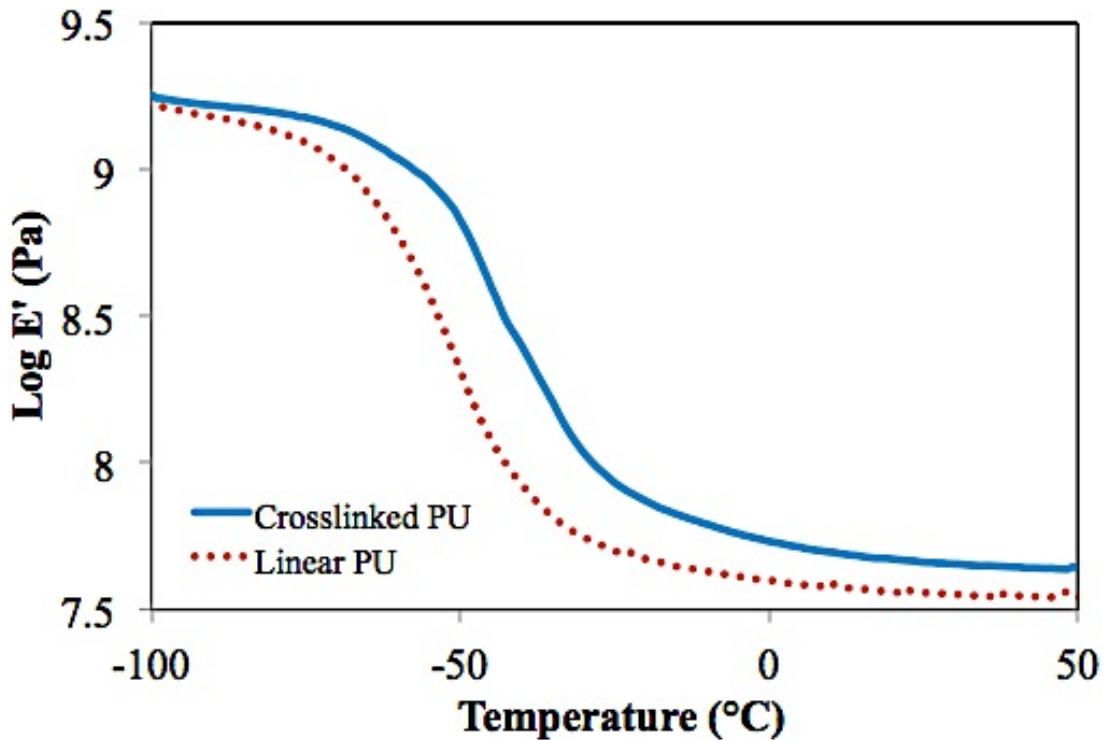


Figure 3.3-1: Storage modulus curve of PU synthesized with glycerin (crosslinked) and PU synthesized with butanediol (linear)

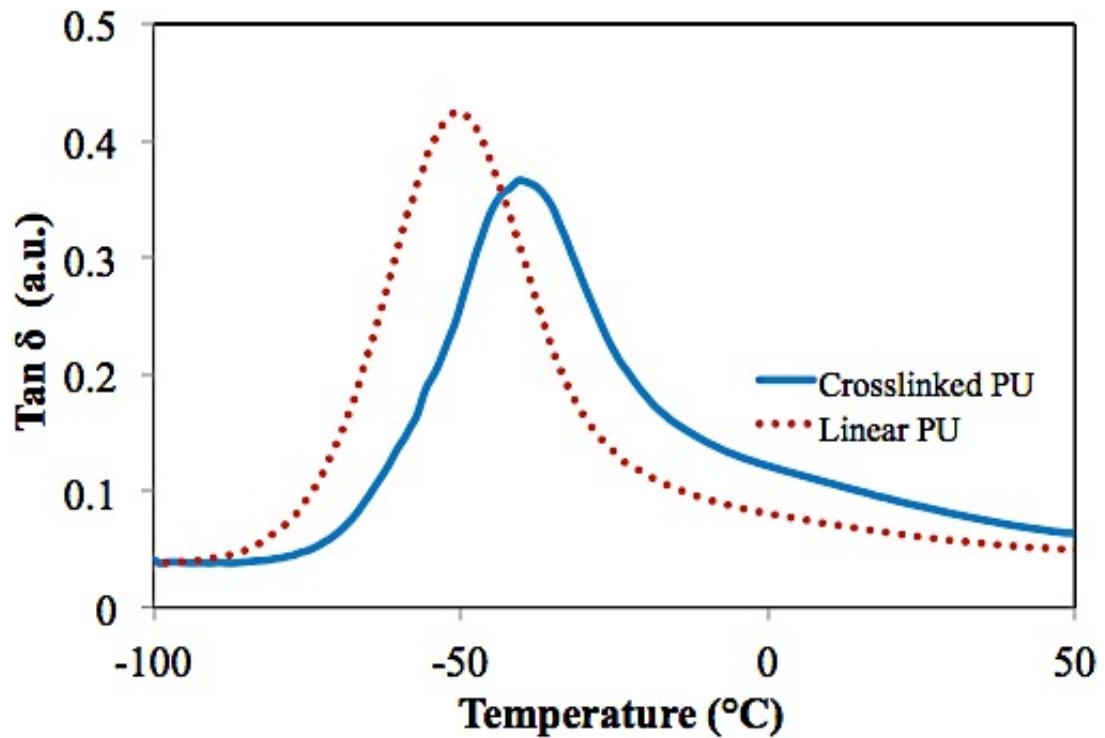


Figure 3.3-2: Tan δ curve of PU synthesized with glycerin (crosslinked) and PU synthesized with butanediol (linear)

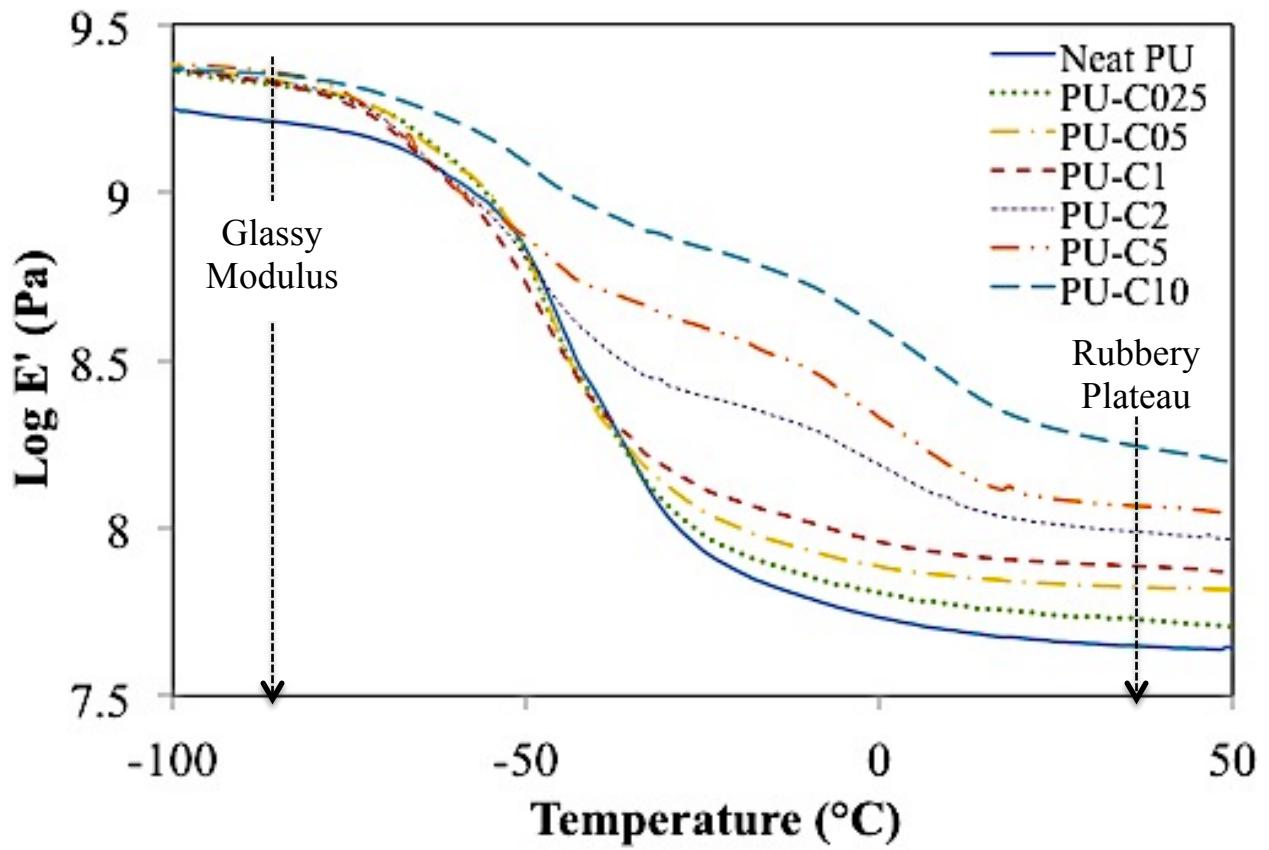


Figure 3.3-3: Storage modulus of neat PU and PU nanocomposites

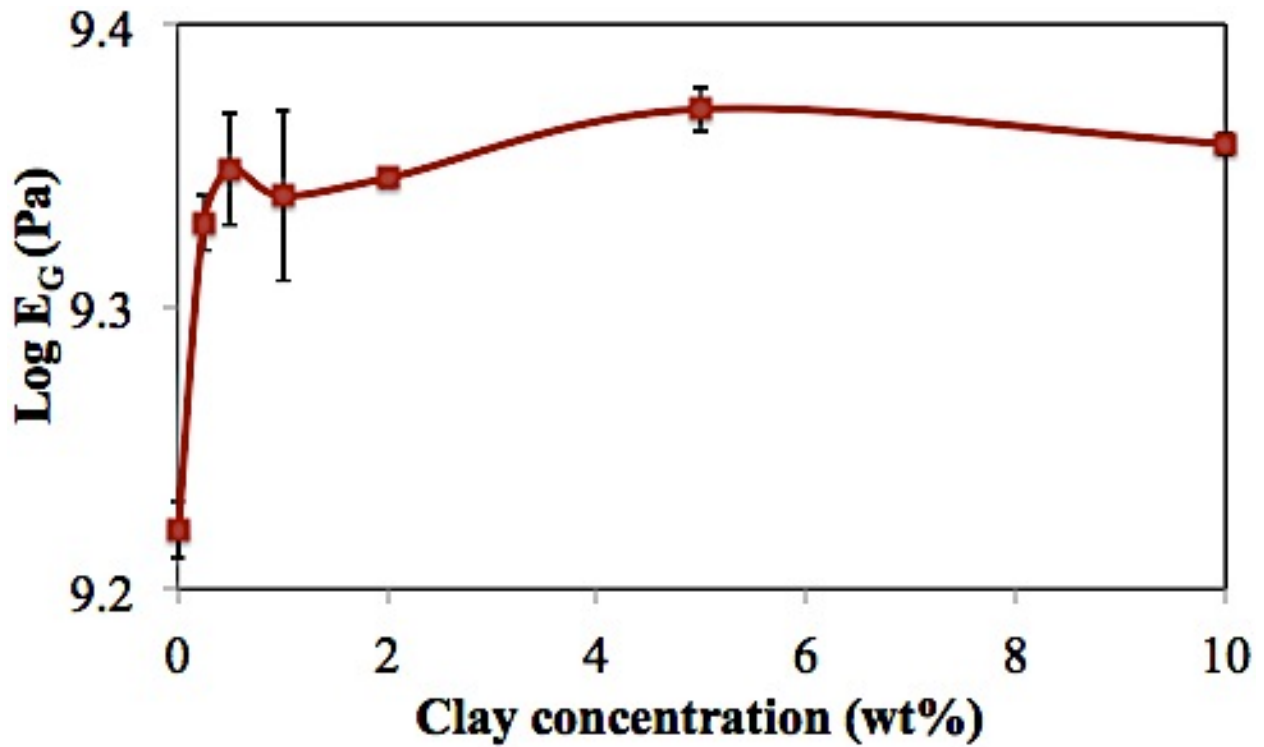


Figure 3.3-4: Change in E_G at -90°C as a function of clay concentration

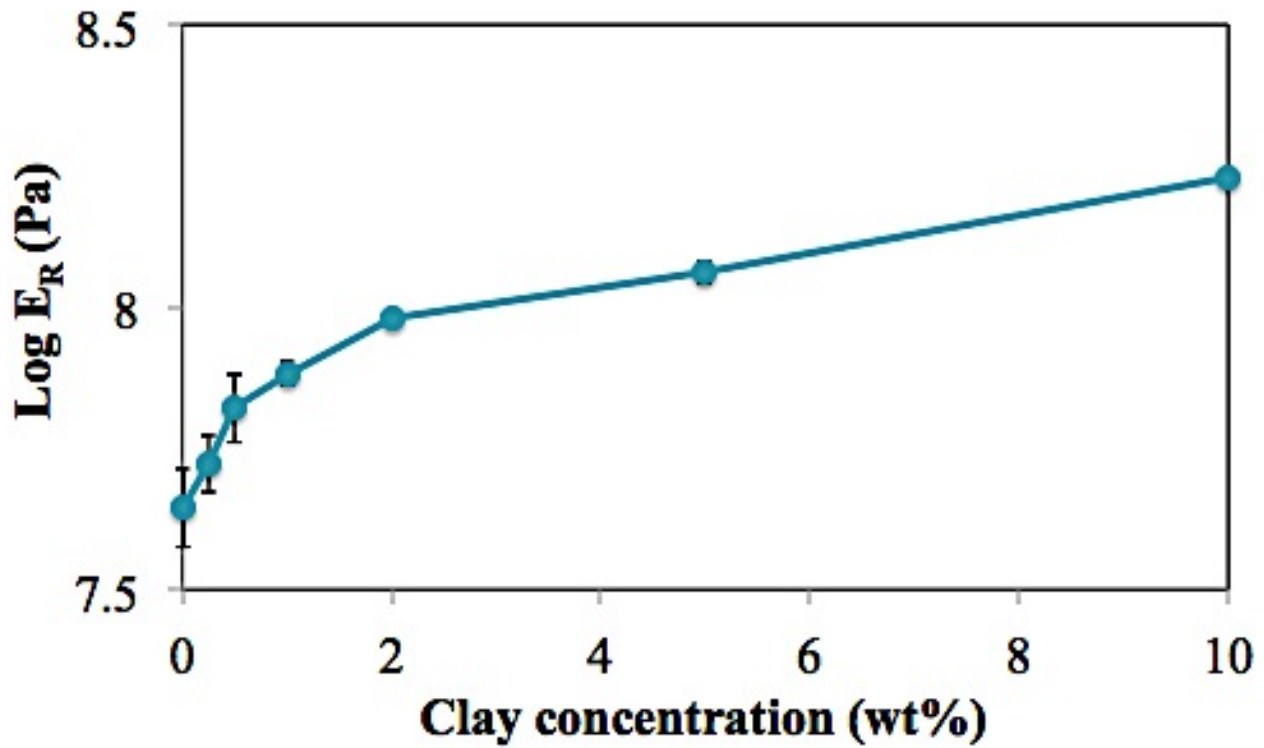


Figure 3.3-5: Change in E_R at 40°C as a function of clay concentration

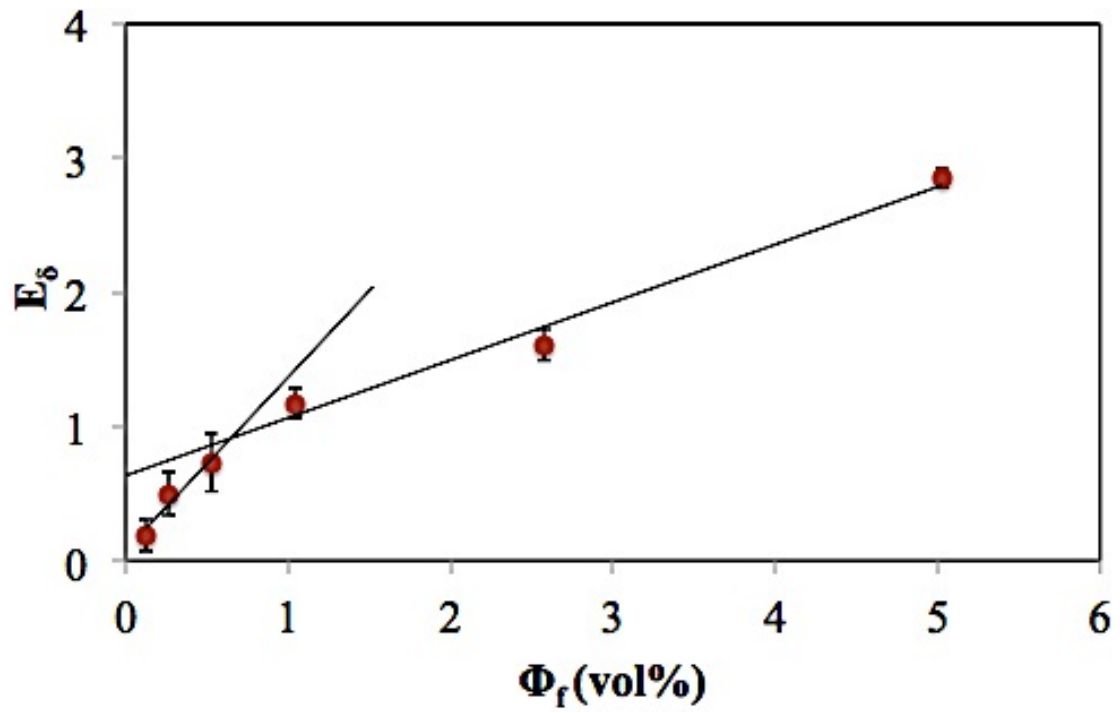


Figure 3.3-6: Modulus enhancement as a function of clay volume fraction

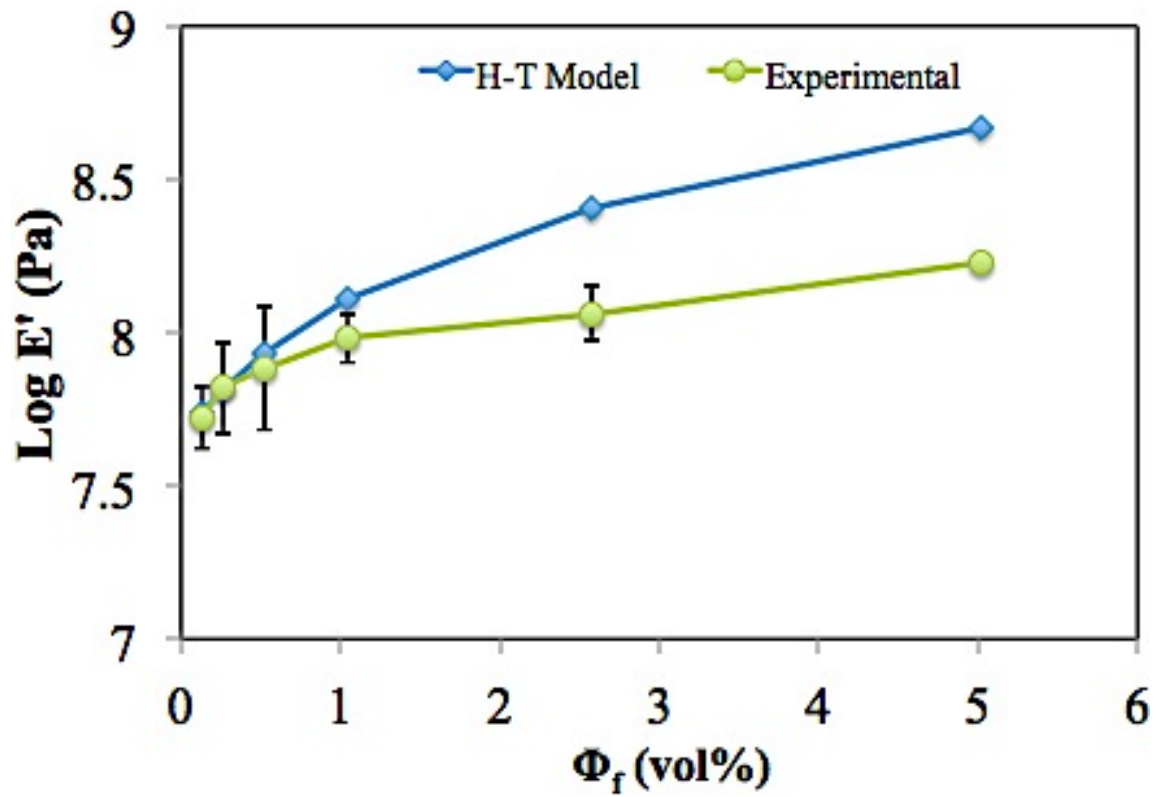


Figure 3.3-7: Comparison of experimental modulus with the Halpin-Tsai model

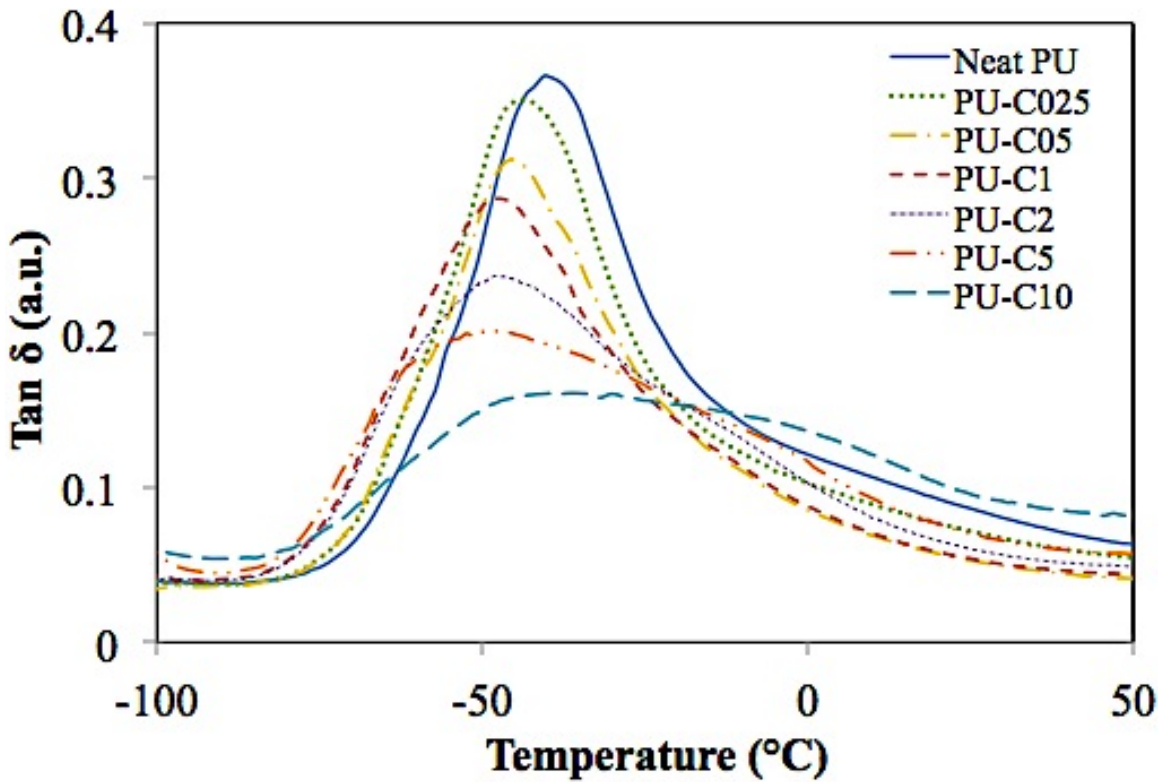


Figure 3.3-8: Tan δ of neat PU and PU nanocomposites

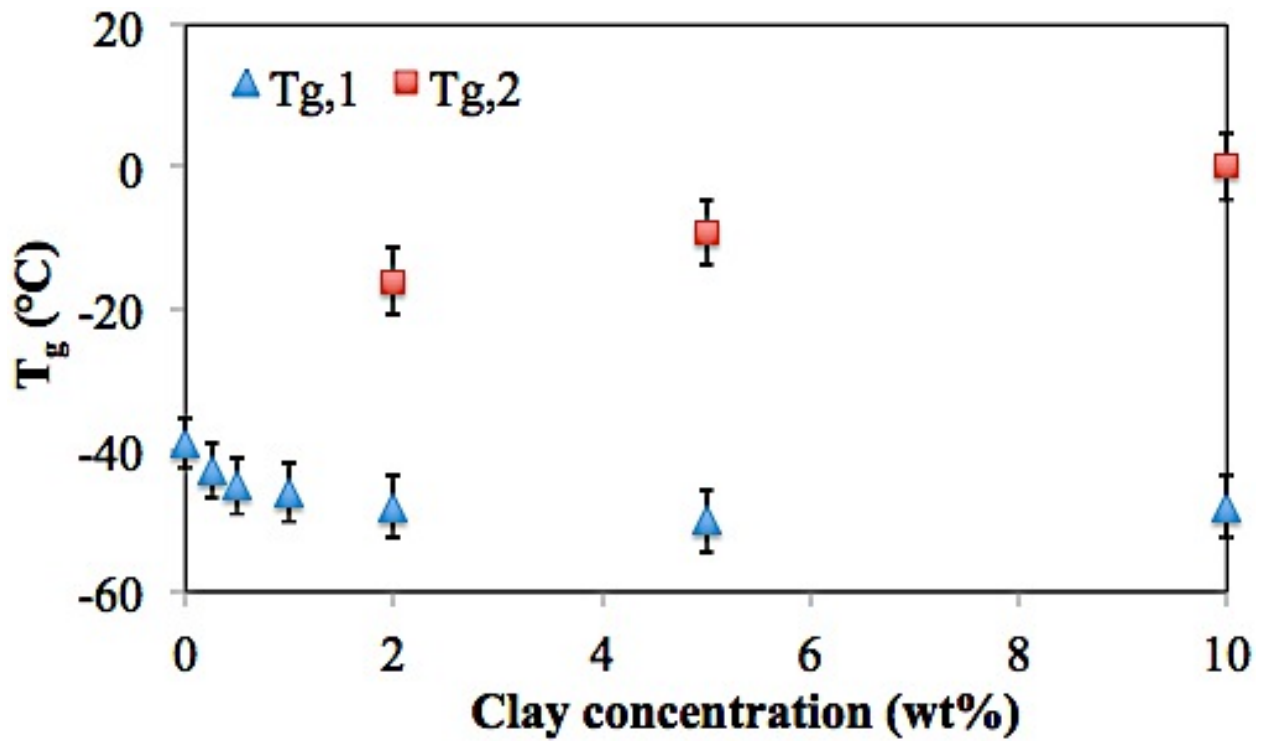


Figure 3.3-9: Glass-transition temperatures as a function of clay concentration

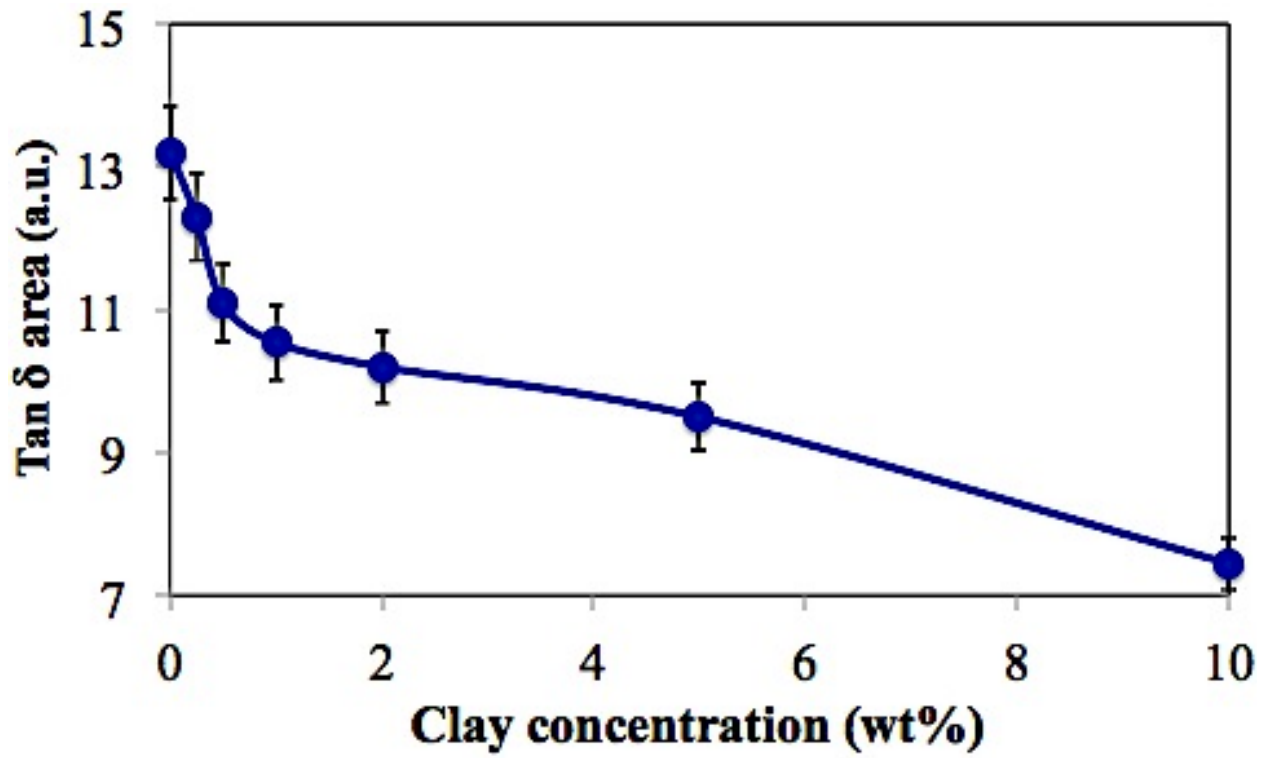


Figure 3.3-10: Damping properties as a function of clay concentration

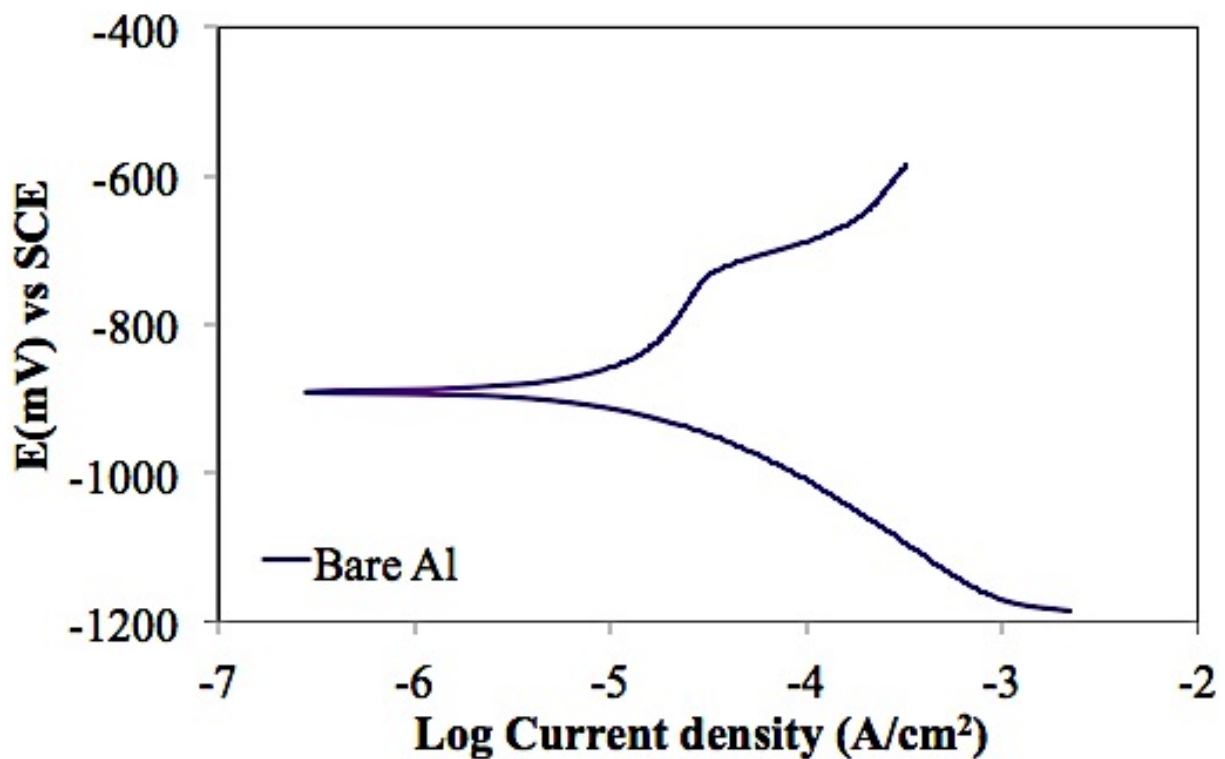


Figure 3.4-1: Tafel polarization curve of bare aluminum alloy

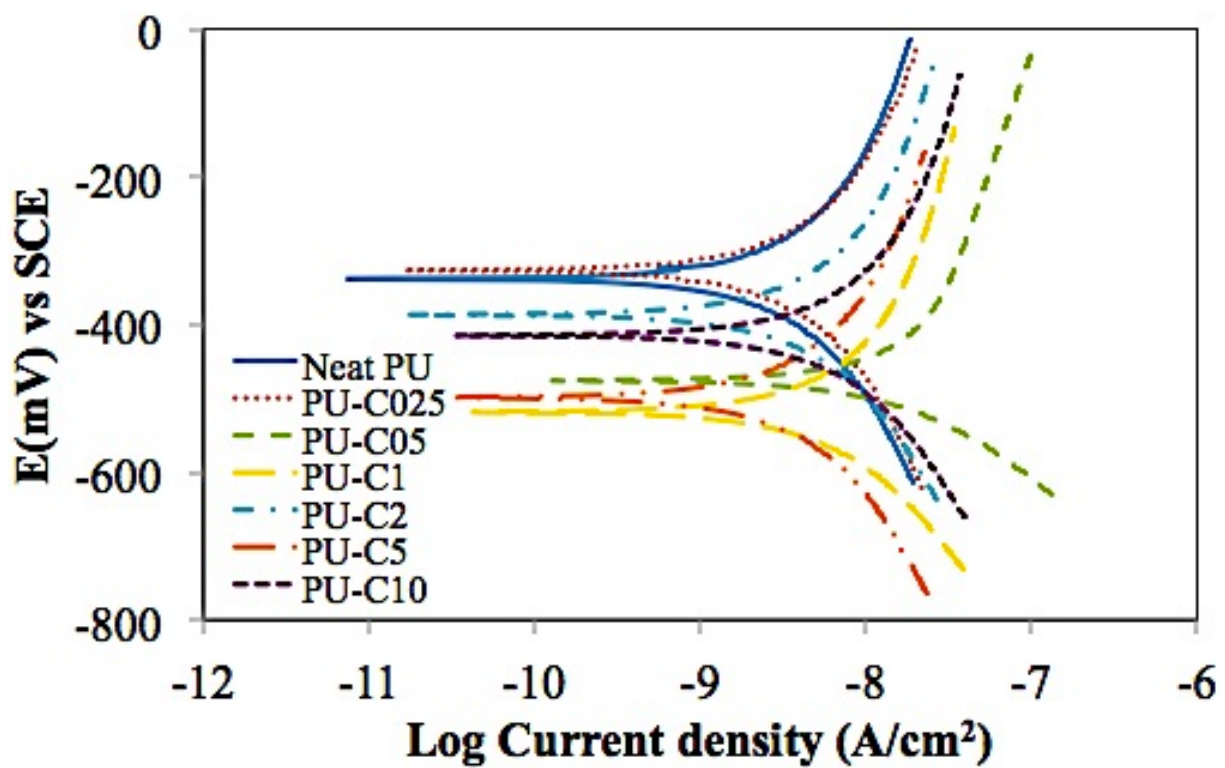


Figure 3.4-2: Tafel polarization curve of neat PU and PU nanocomposites after 7 days exposure

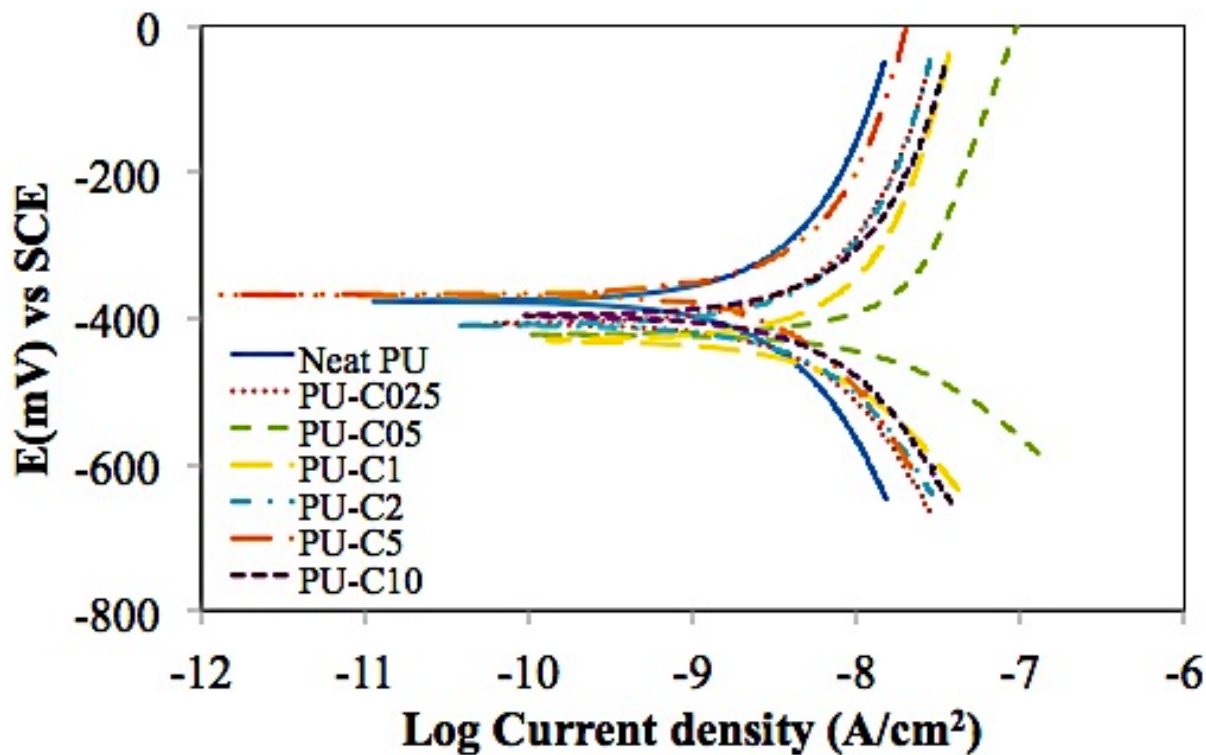


Figure 3.4-3 Tafel polarization curve of neat PU and PU nanocomposites after 14 days exposure

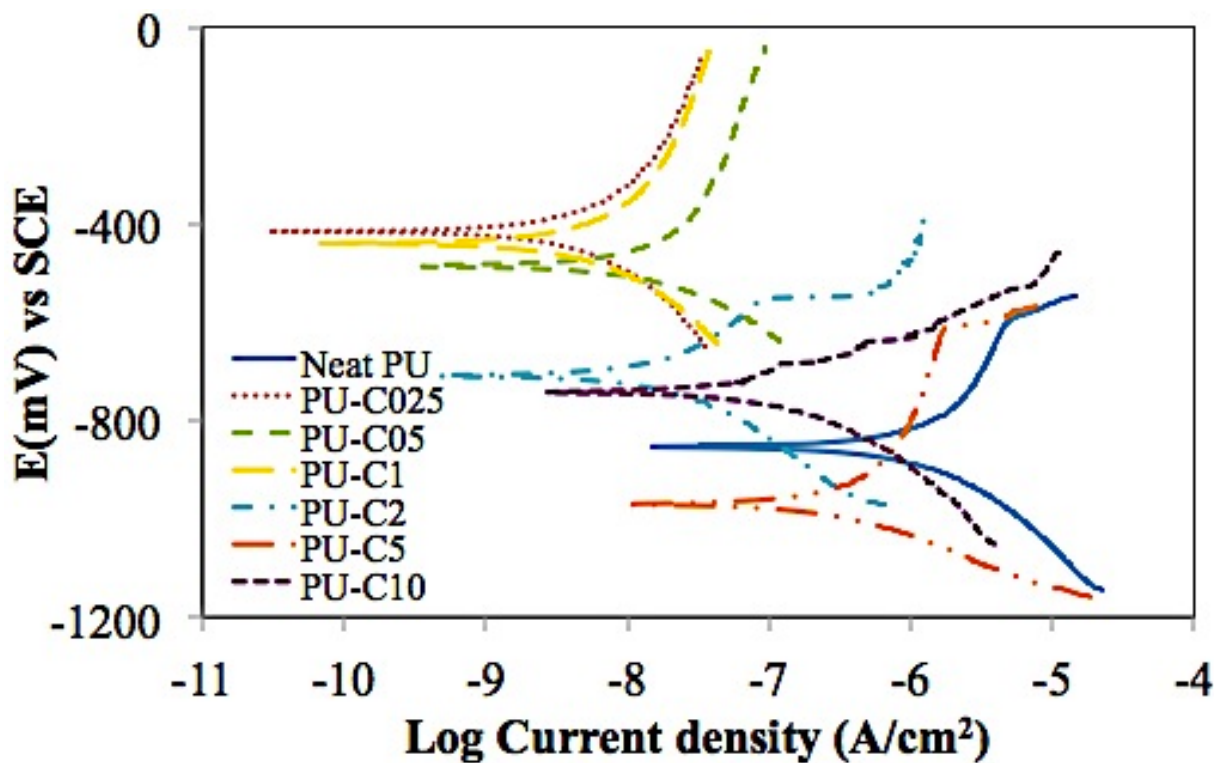


Figure 3.4-4 Tafel polarization curve of neat PU and PU nanocomposites after 30 days exposure

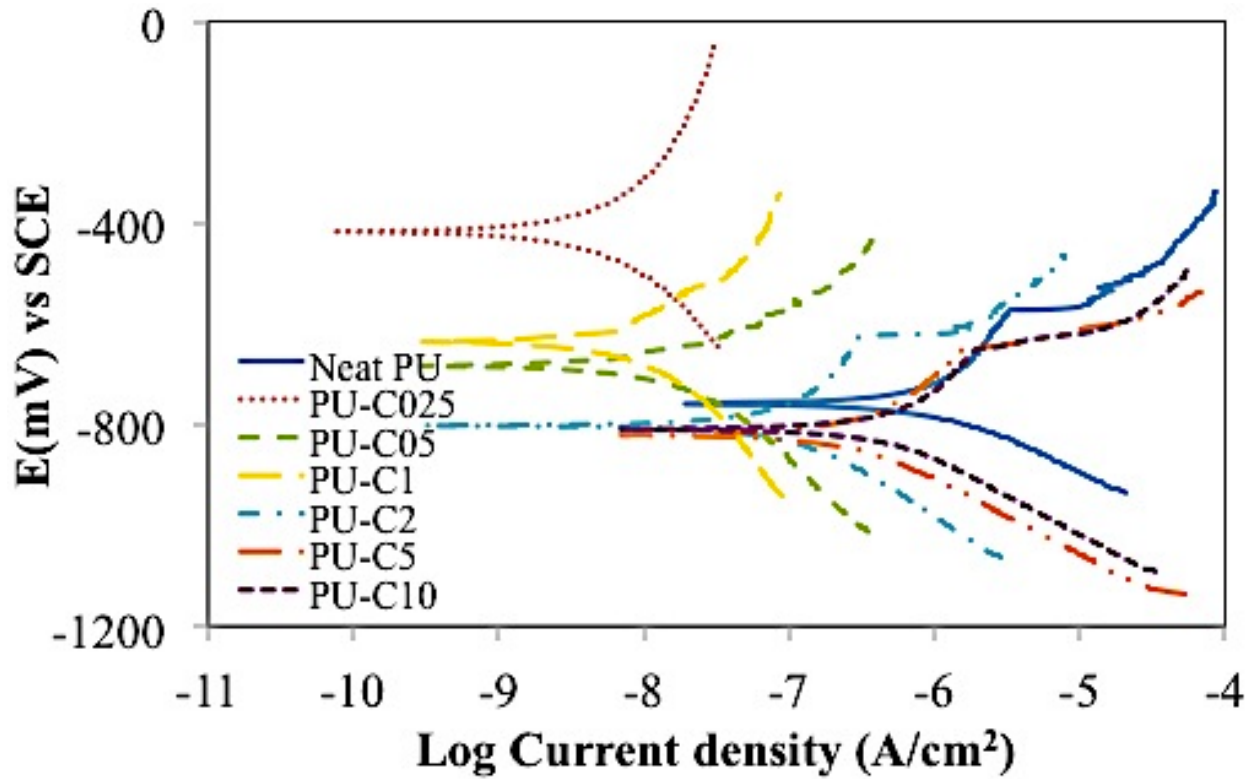


Figure 3.4-5: Tafel polarization curve of neat PU and PU nanocomposites after 60 days exposure

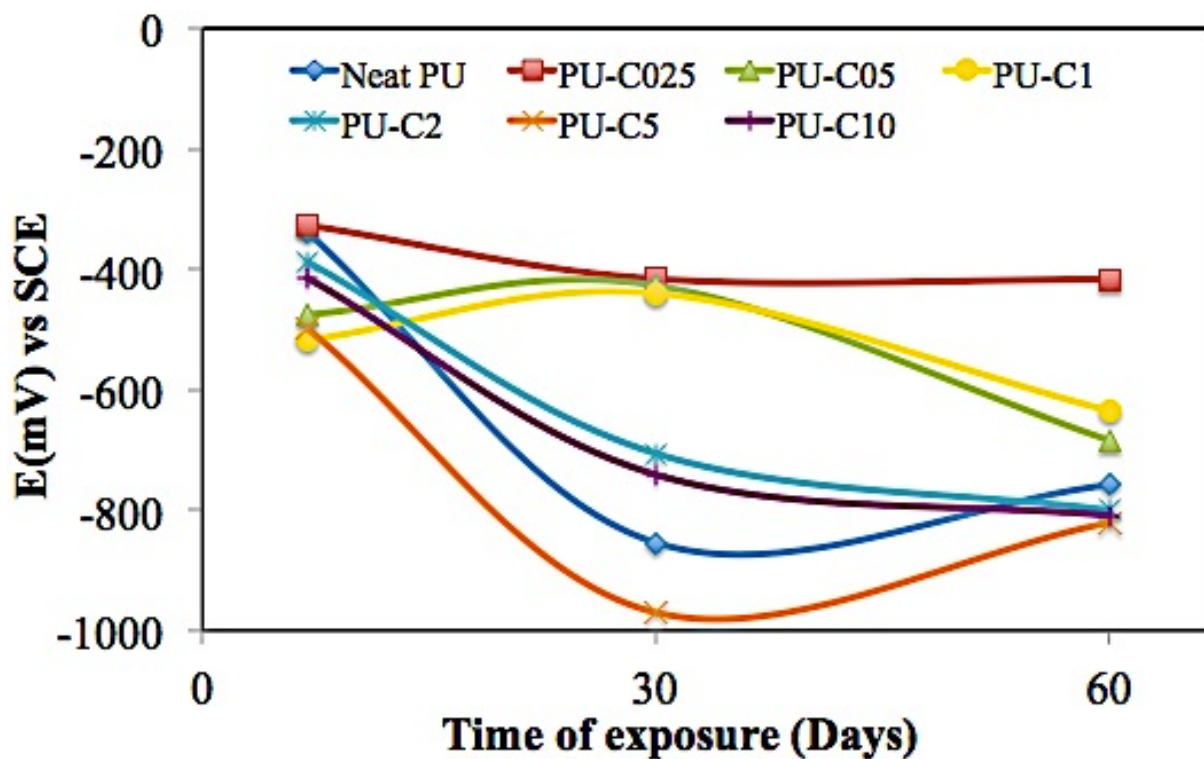


Figure 3.4-6: E_{corr} of neat PU and PU nanocomposites over 60 days exposure to salt water

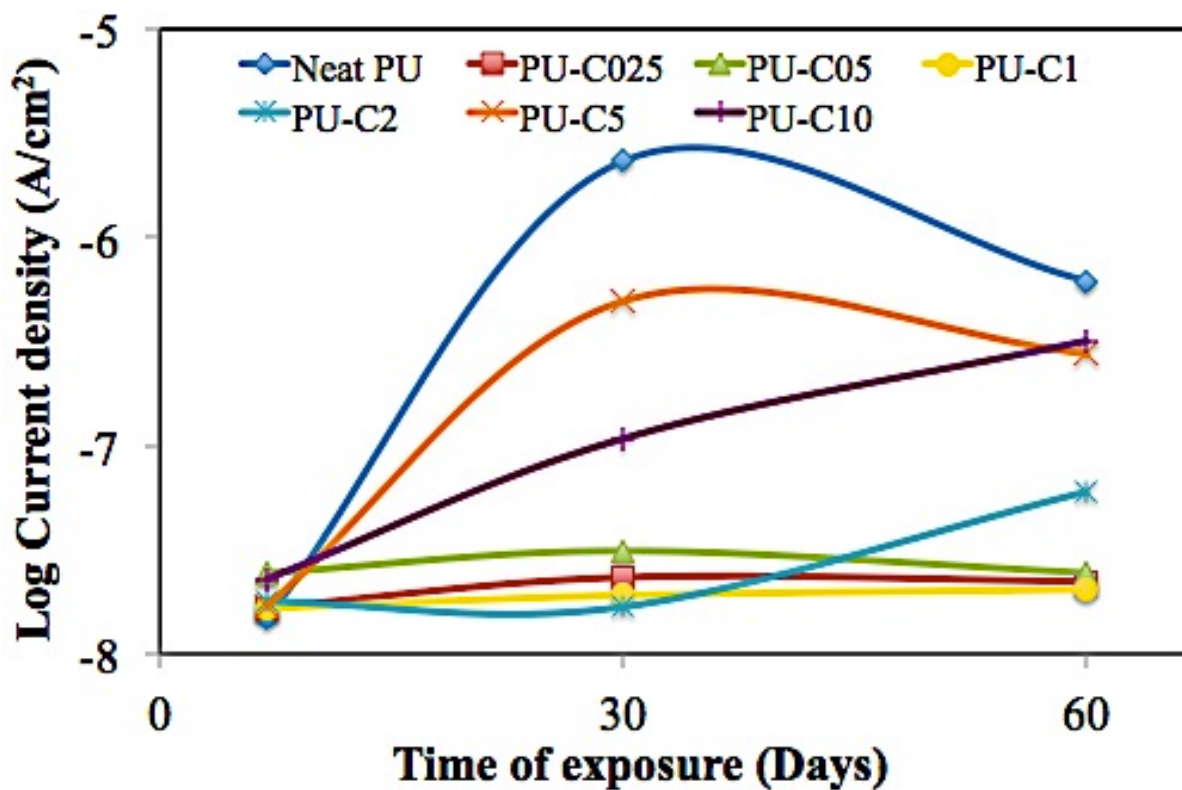


Figure 3.4-7: I_{corr} of neat PU and PU nanocomposites over 60 days exposure to salt water

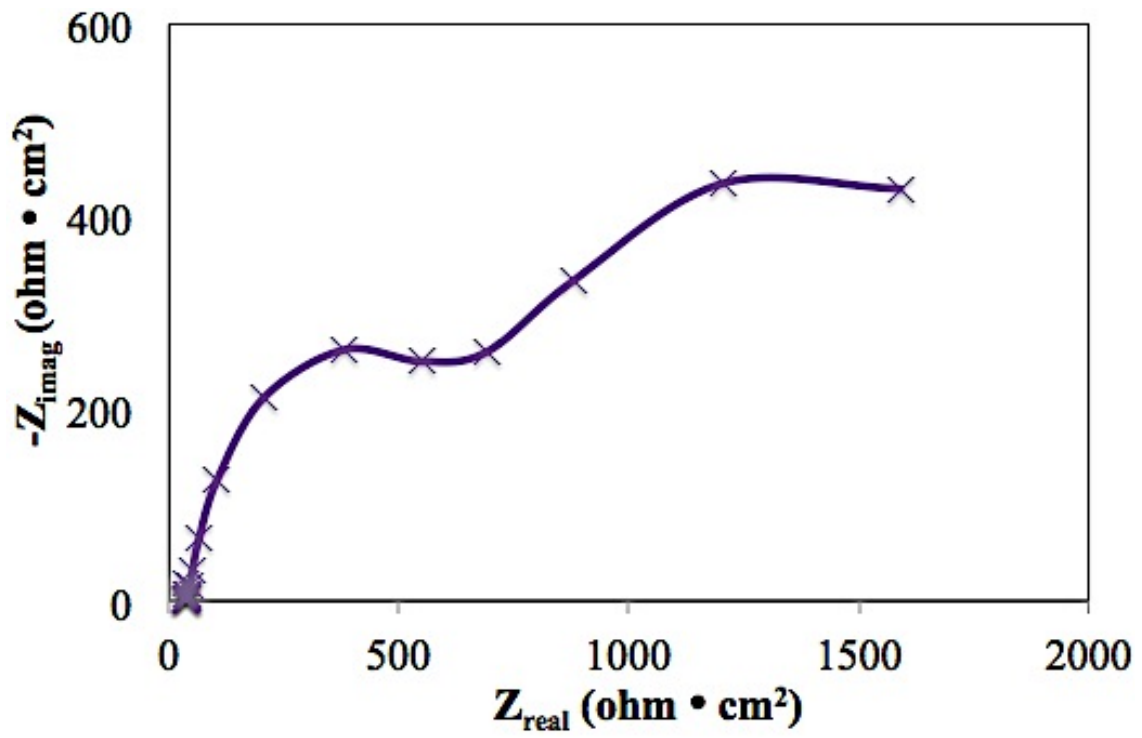


Figure 3.4-8: Nyquist plot of bare aluminum alloy

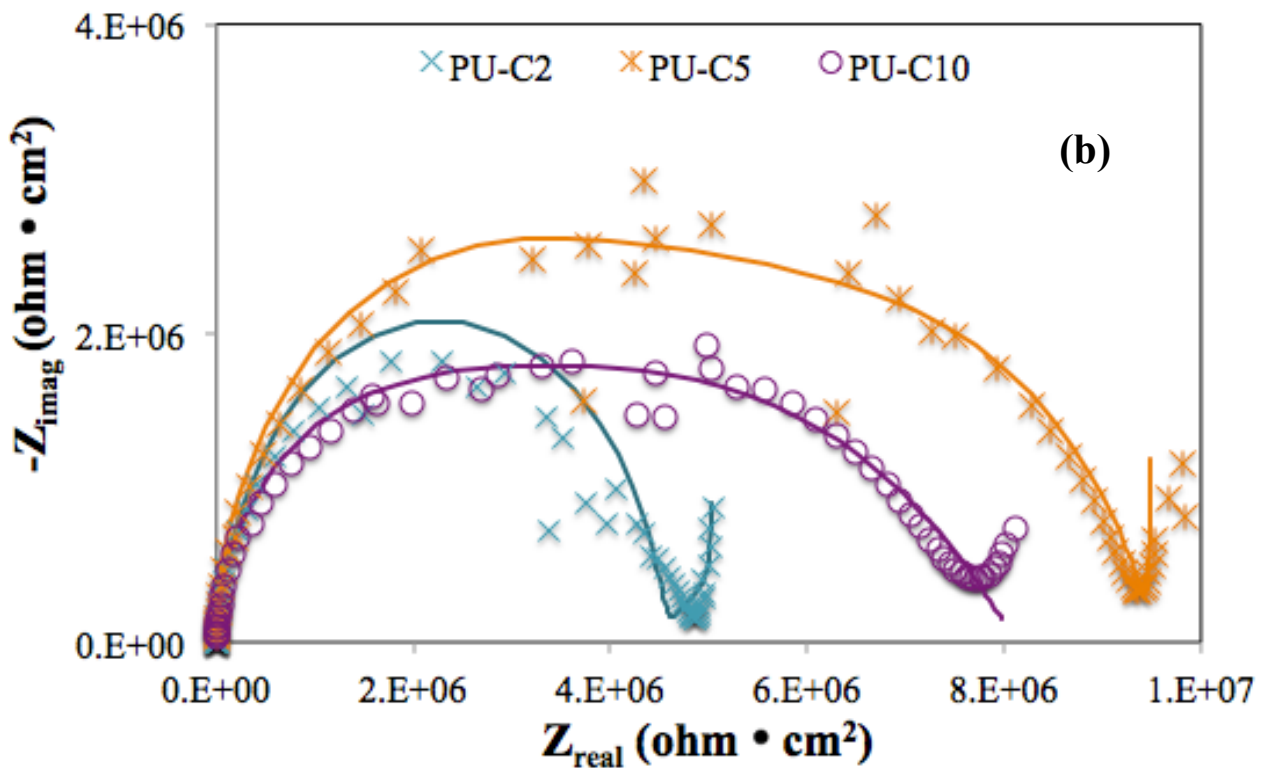
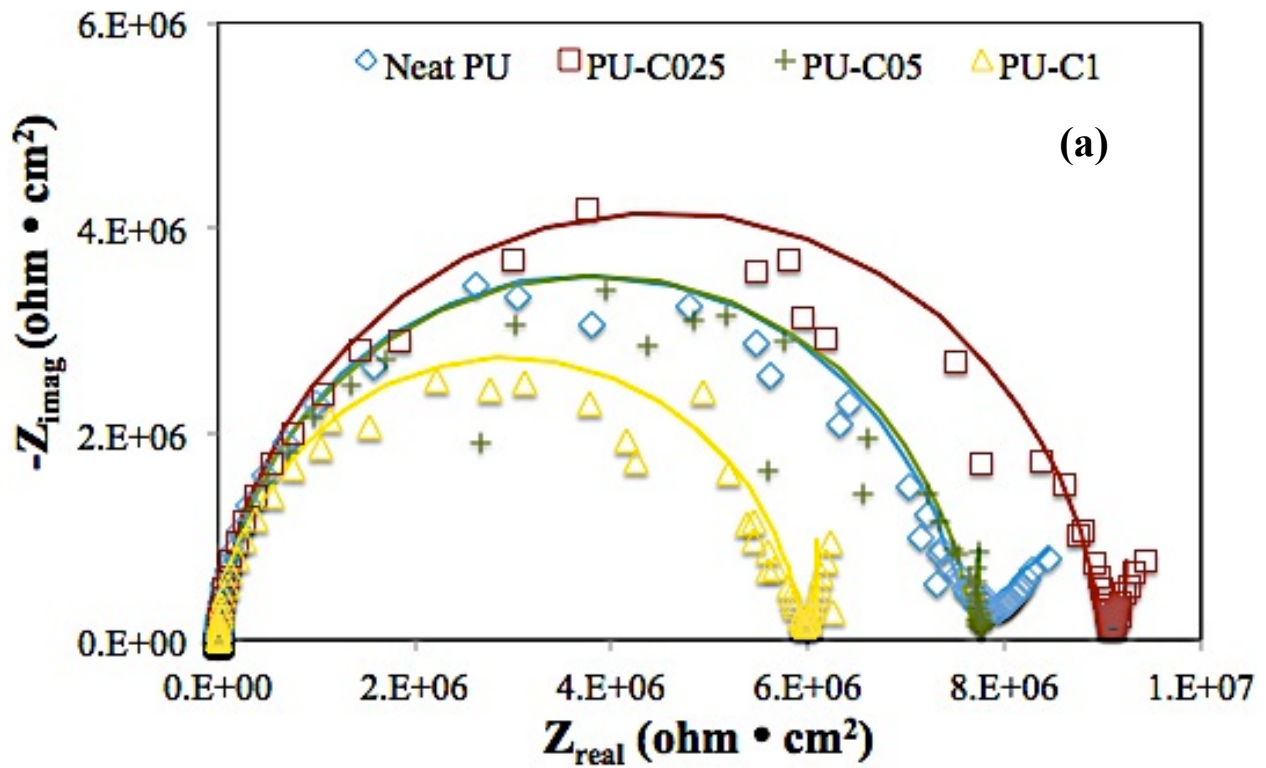
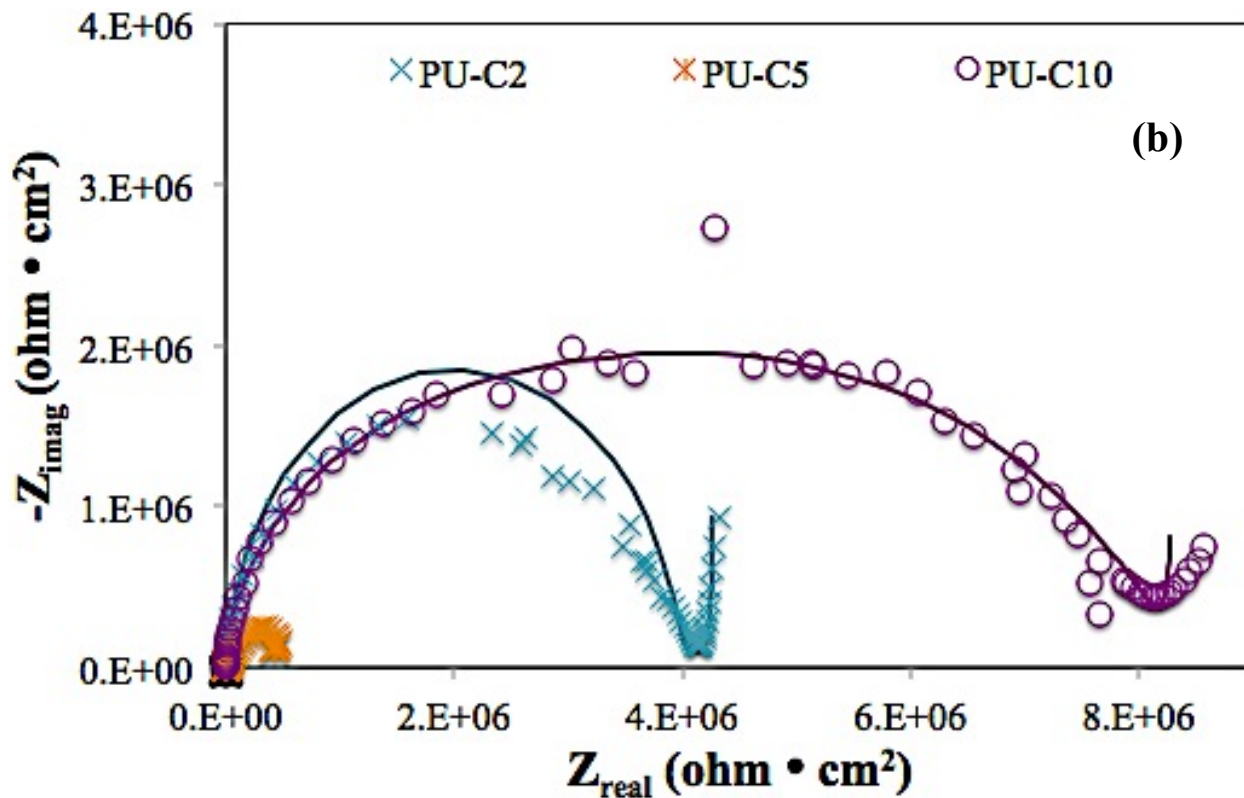
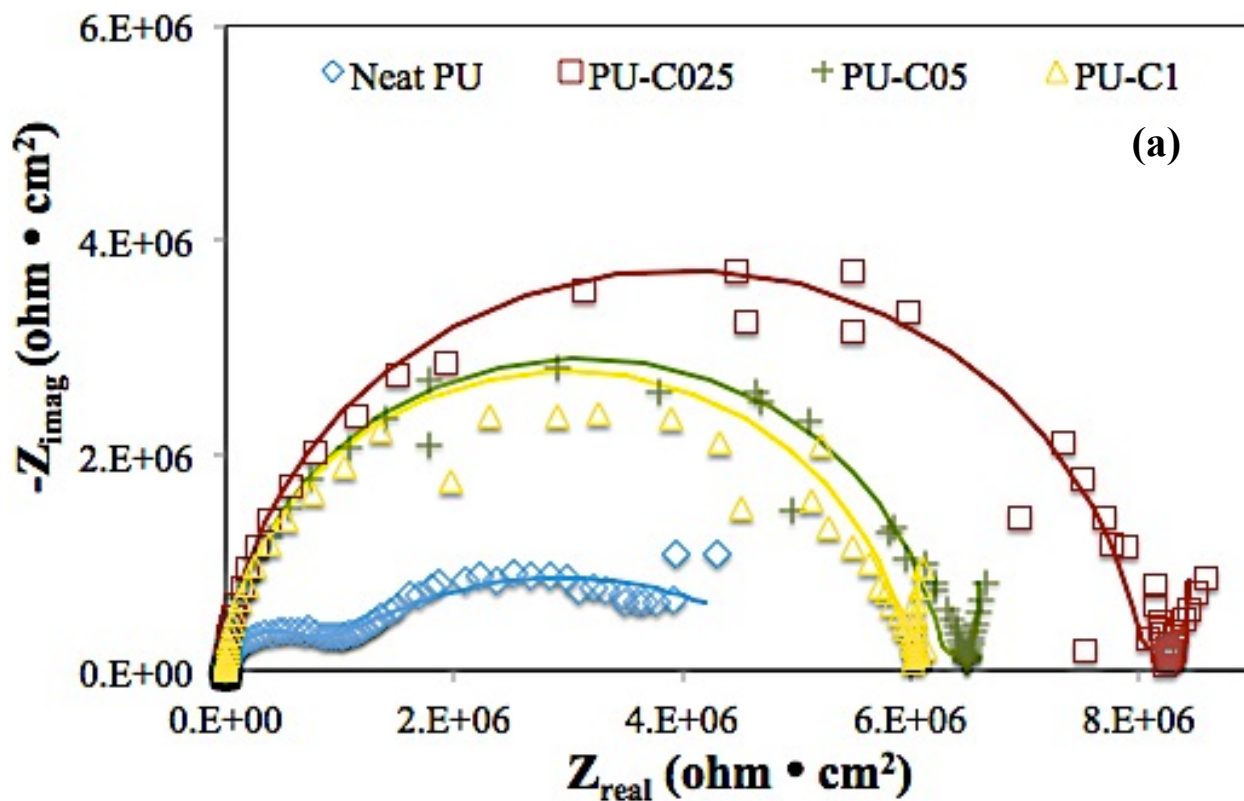


Figure 3.4-9: Nyquist plot of (a) neat PU, PU-C025, PU-C05, PU-C1 (b) PU-C2, PU-C5 and PU-C10 after 7 days exposure to salt water



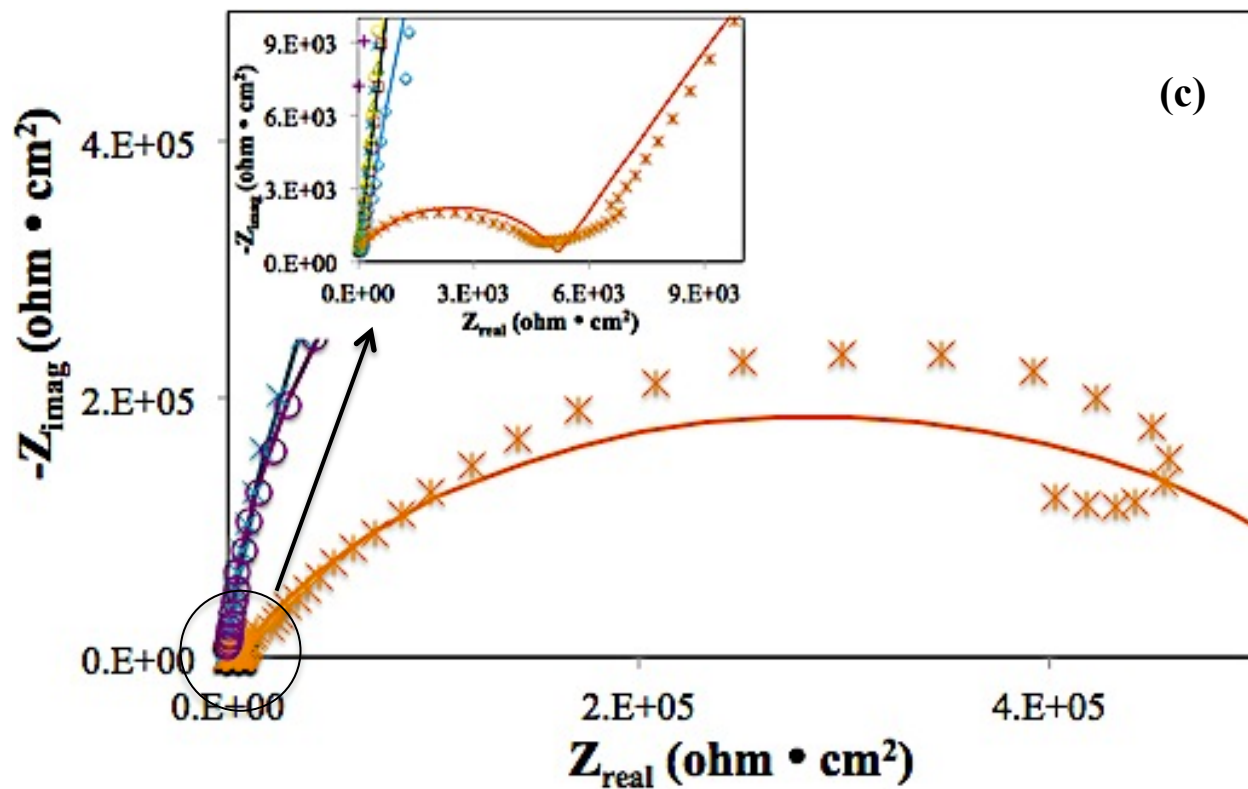


Figure 3.4-10: Nyquist plot of (a) neat PU, PU-C025, PU-C05, PU-C1 (b) PU-C2, PU-C5 PU-C10 and (c) close-up of corroded PU-C5 after 14 days exposure to salt water

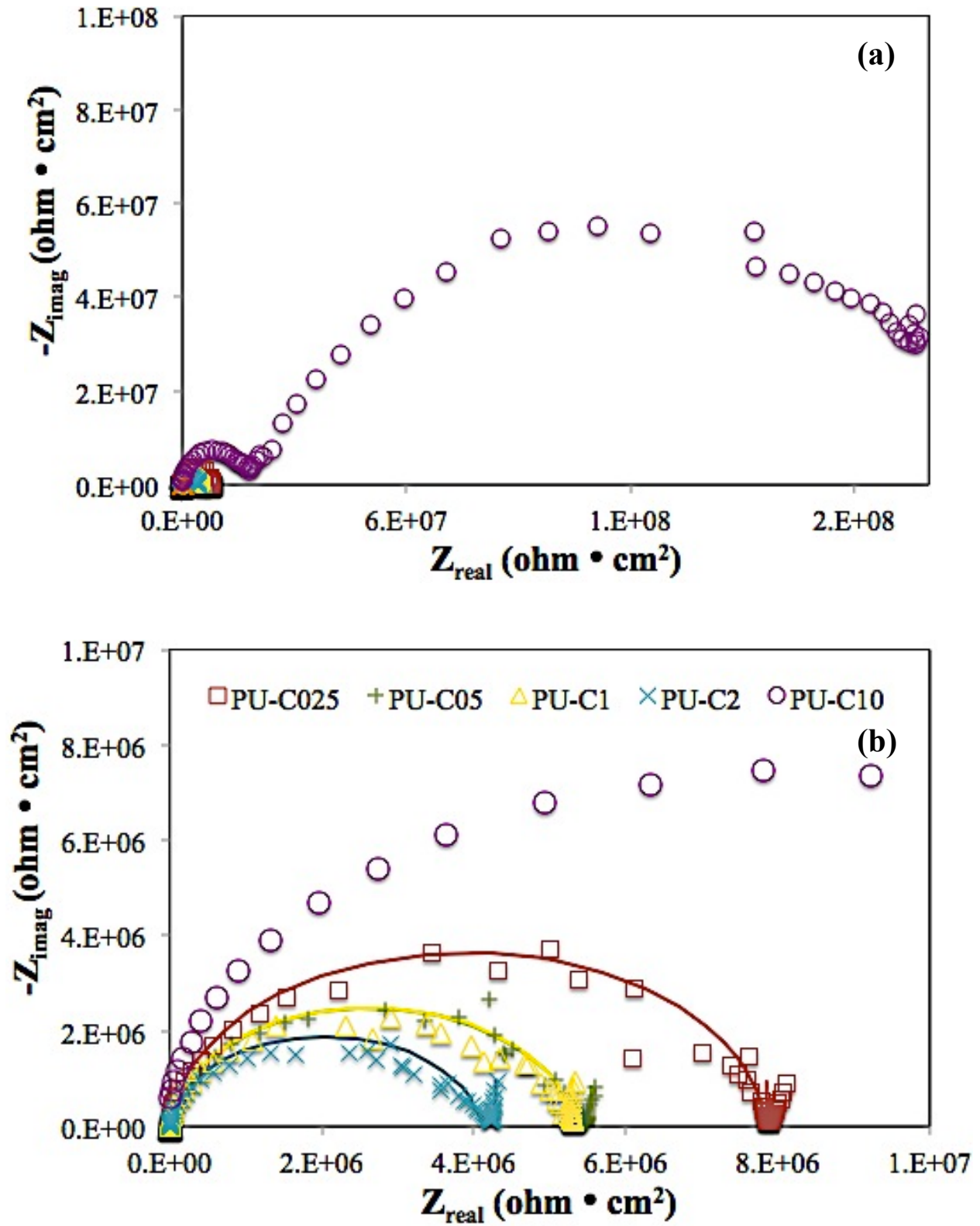


Figure 3.4-11: Nyquist plot of (a) corroded PU-C10 close-up and (b) non-corroded PU nanocomposites after 30 days exposure

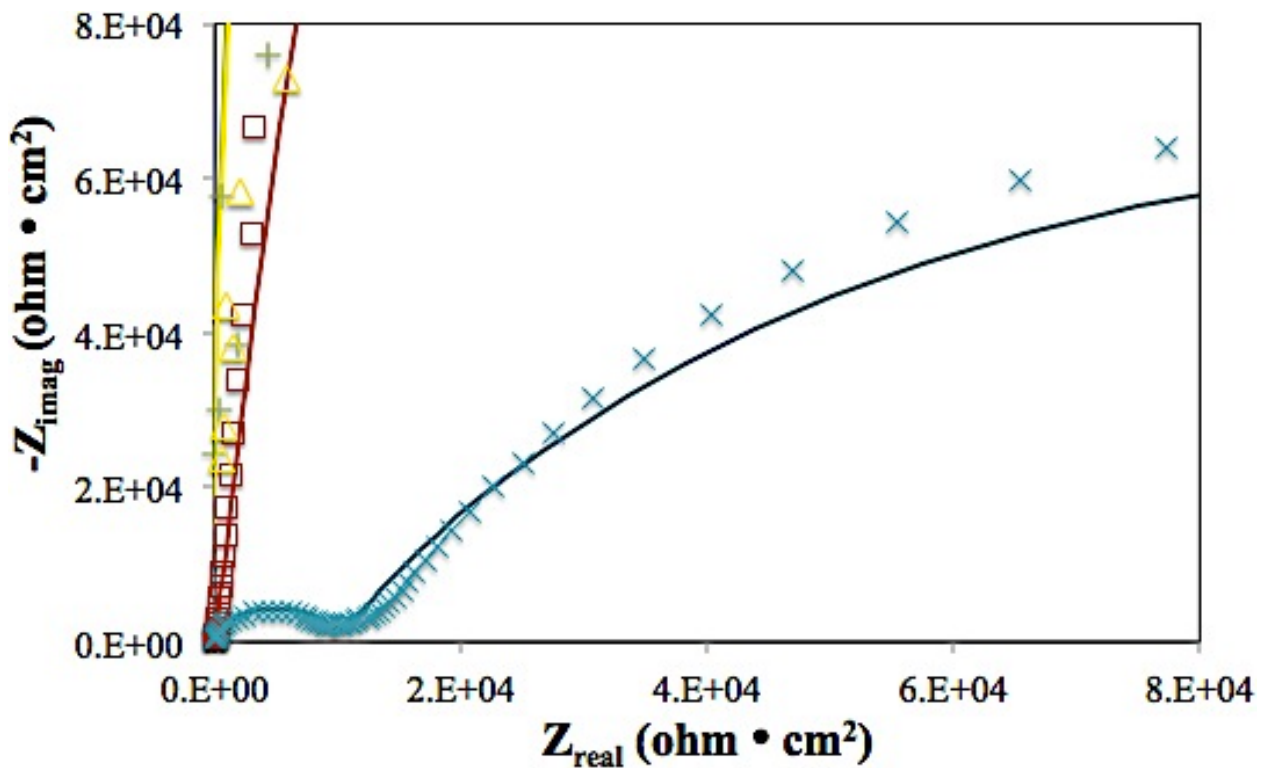
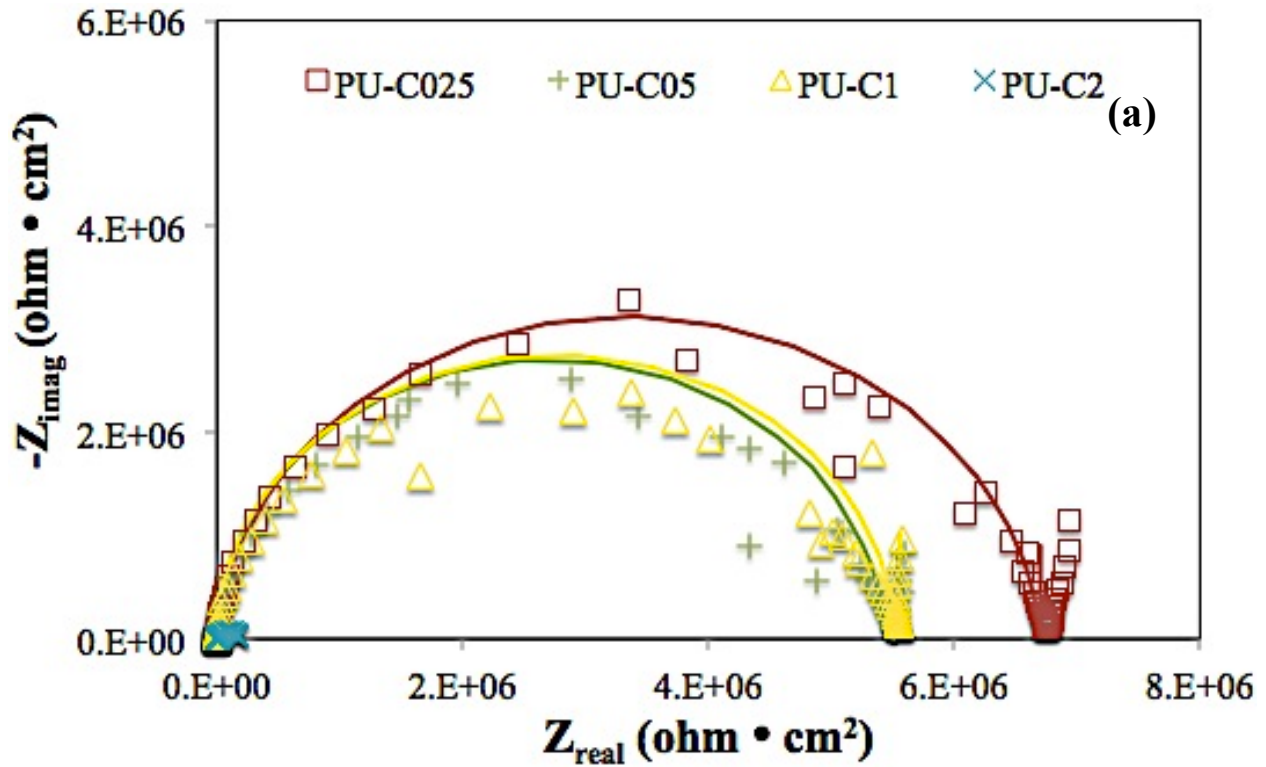


Figure 3.4-12: Nyquist plot of (a) non-corroded PU nanocomposites and (b) close-up of corroded PU-C2 after 60 days exposure to salt water

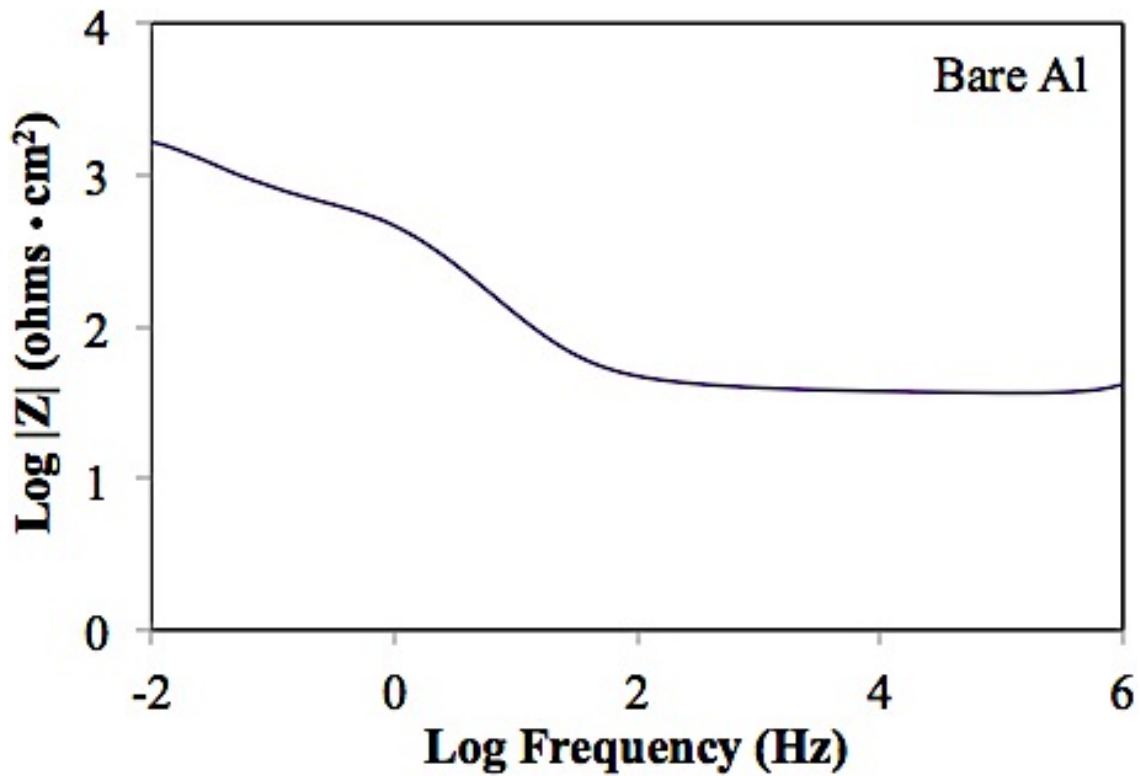


Figure 3.4-15: Bode plot of bare aluminum alloy

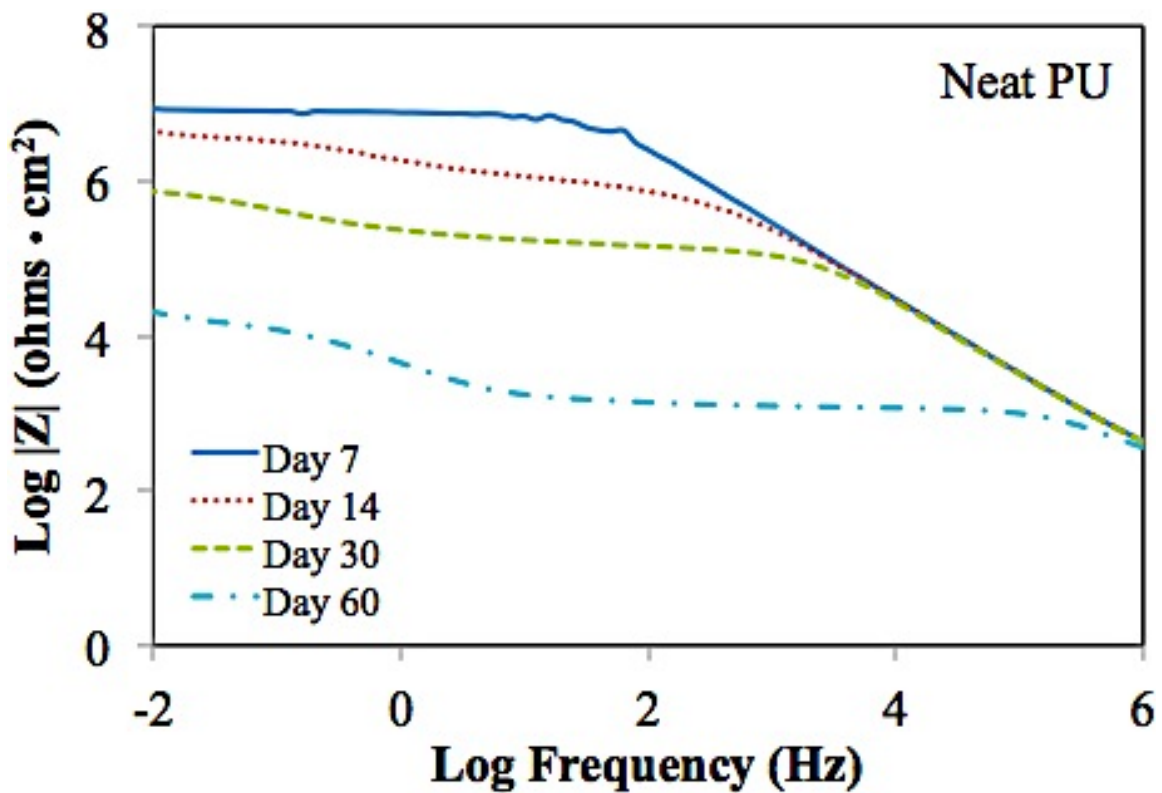


Figure 3.4-16: Bode plot of PU containing 0 wt% clay over 60-day exposure to salt water

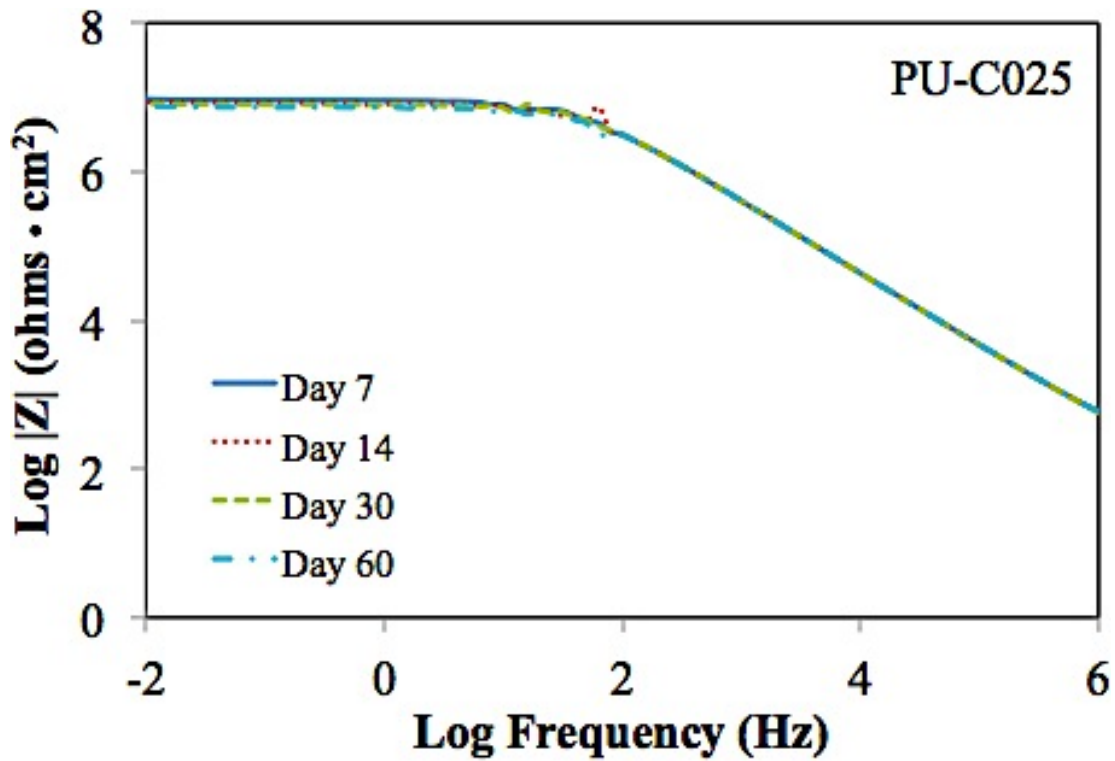


Figure 3.4-17: Bode plot of PU containing 0.25 wt% clay over 60-day exposure to salt water

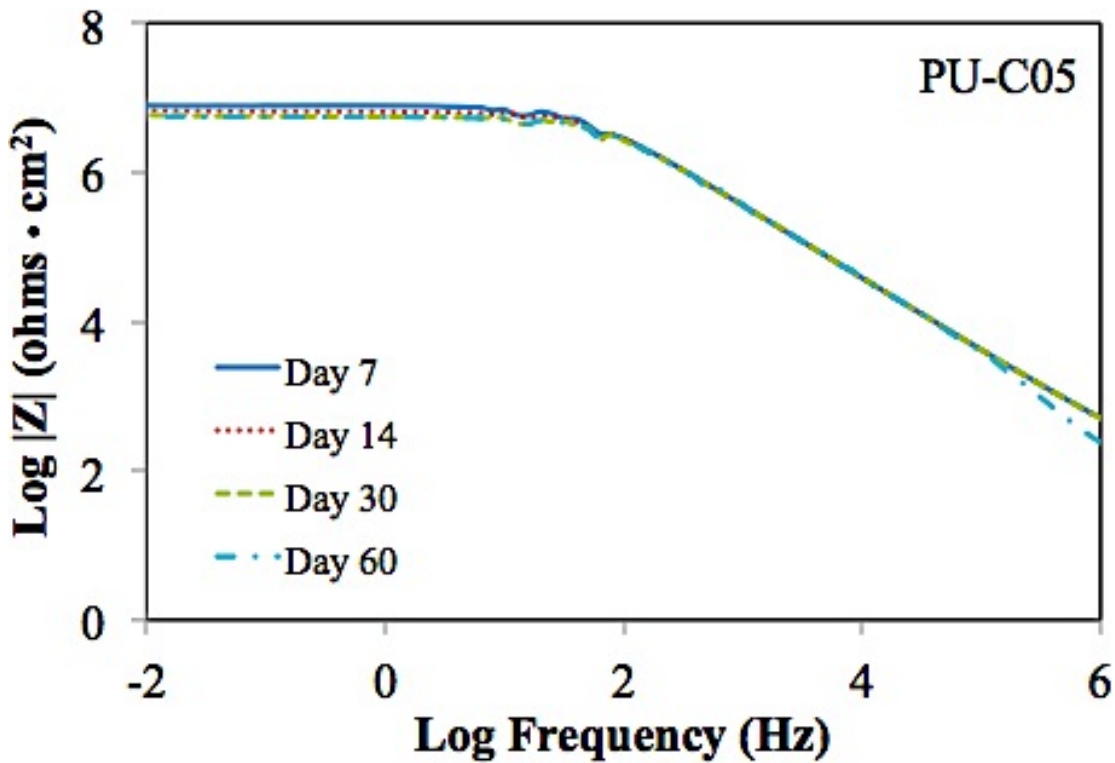


Figure 3.4-18: Bode plot of PU containing 0.5 wt% clay over 60-day exposure to salt water

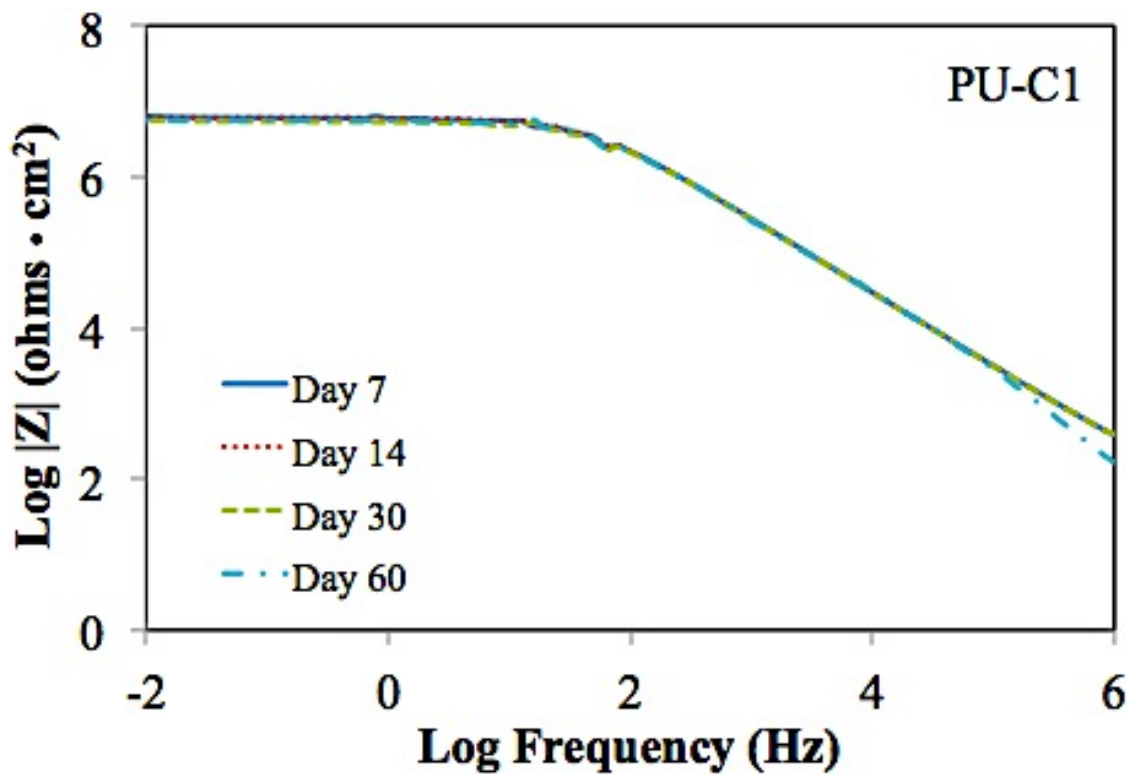


Figure 3.4-19: Bode plot of PU containing 1 wt% clay over 60-day exposure to salt water

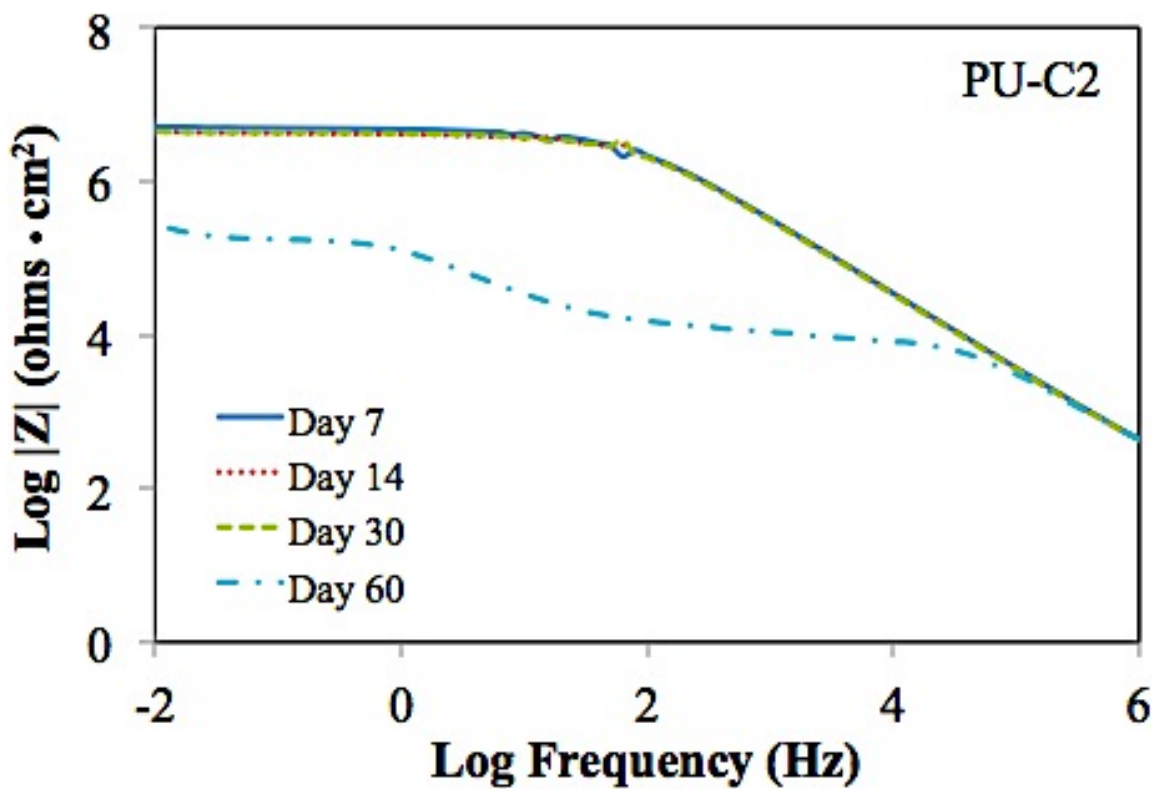


Figure 3.4-20: Bode plot of PU containing 2 wt% clay over 60-day exposure to salt water

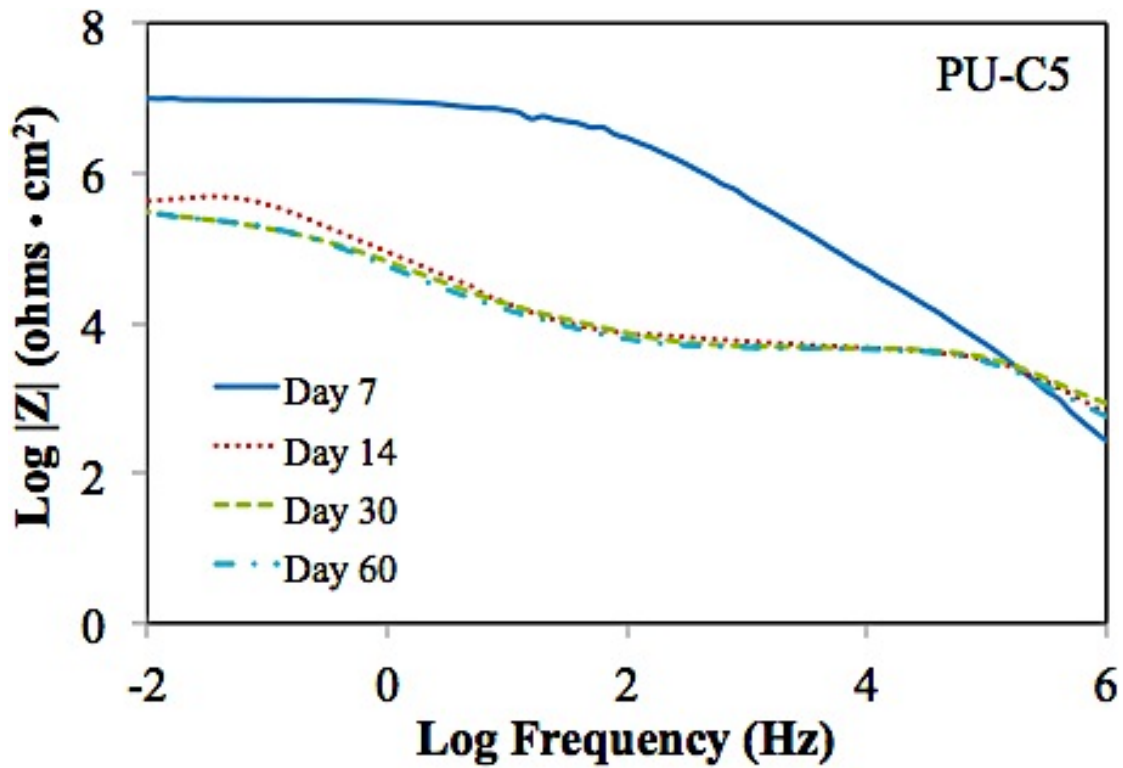


Figure 3.4-21: Bode plot of PU containing 5 wt% clay over 60-day exposure to salt water

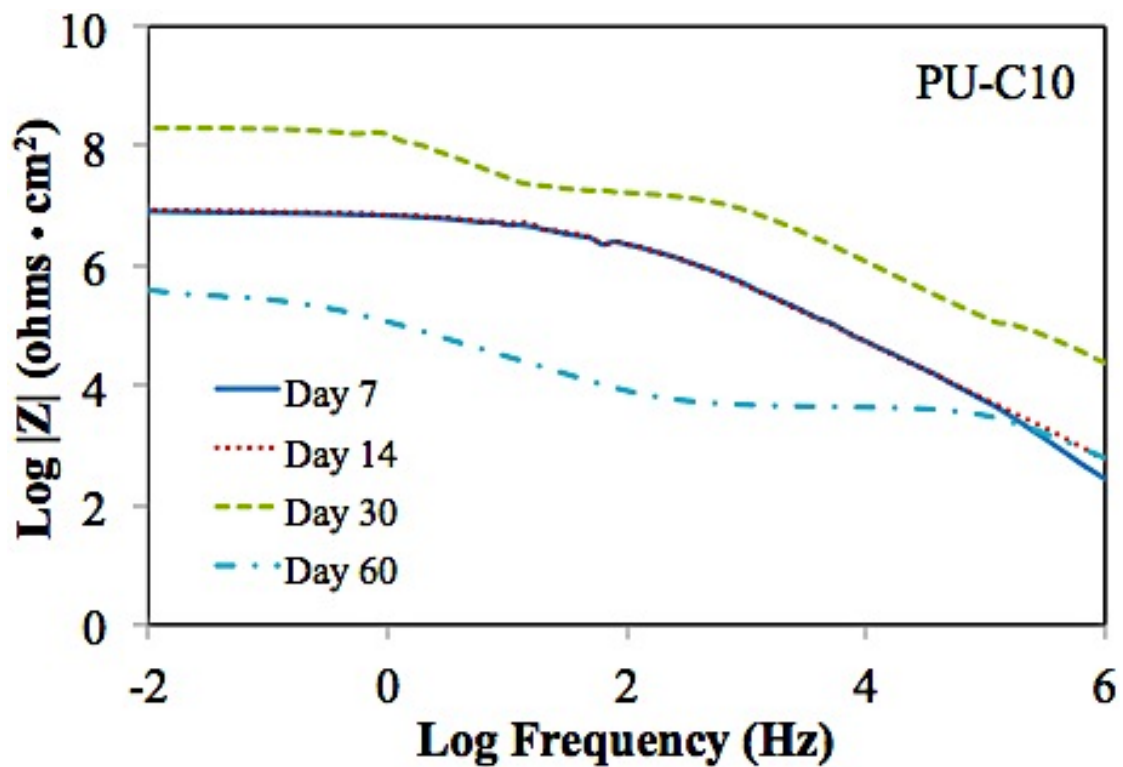


Figure 3.4-22: Bode plot of PU containing 10 wt% clay over 60-day exposure to salt water

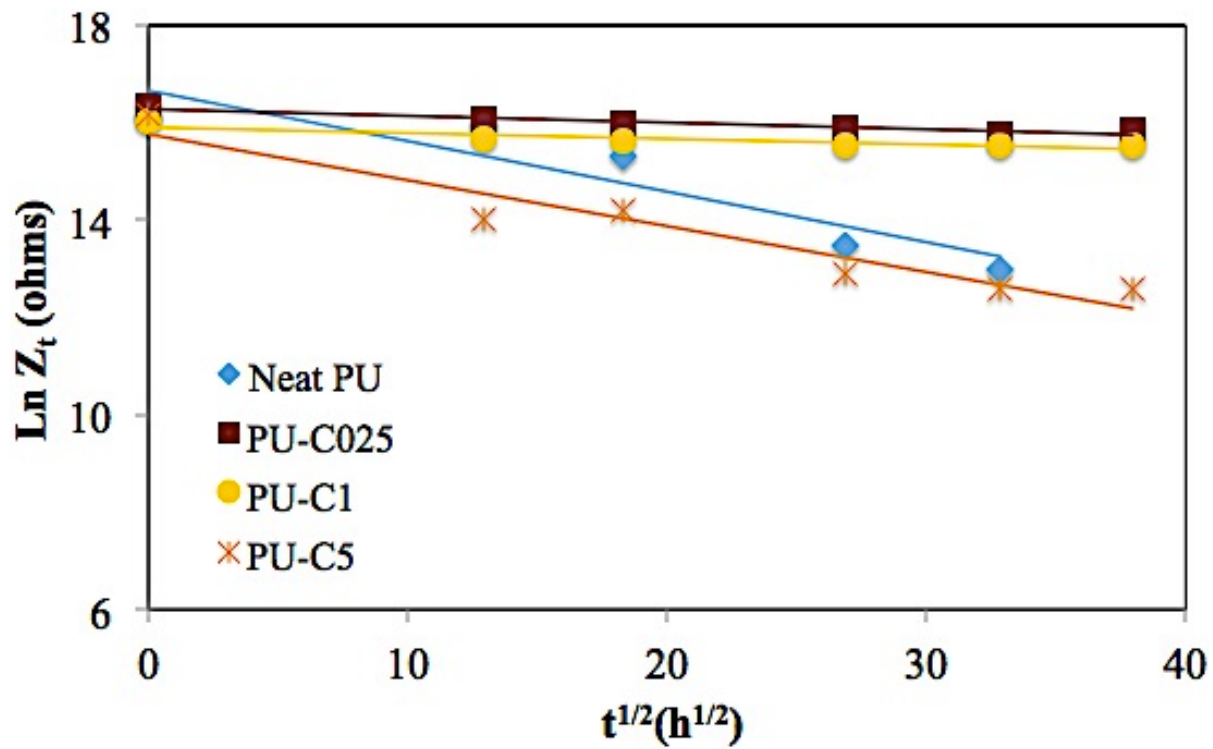


Figure 3.4-23: Change in initial impedance as exposure time is increased

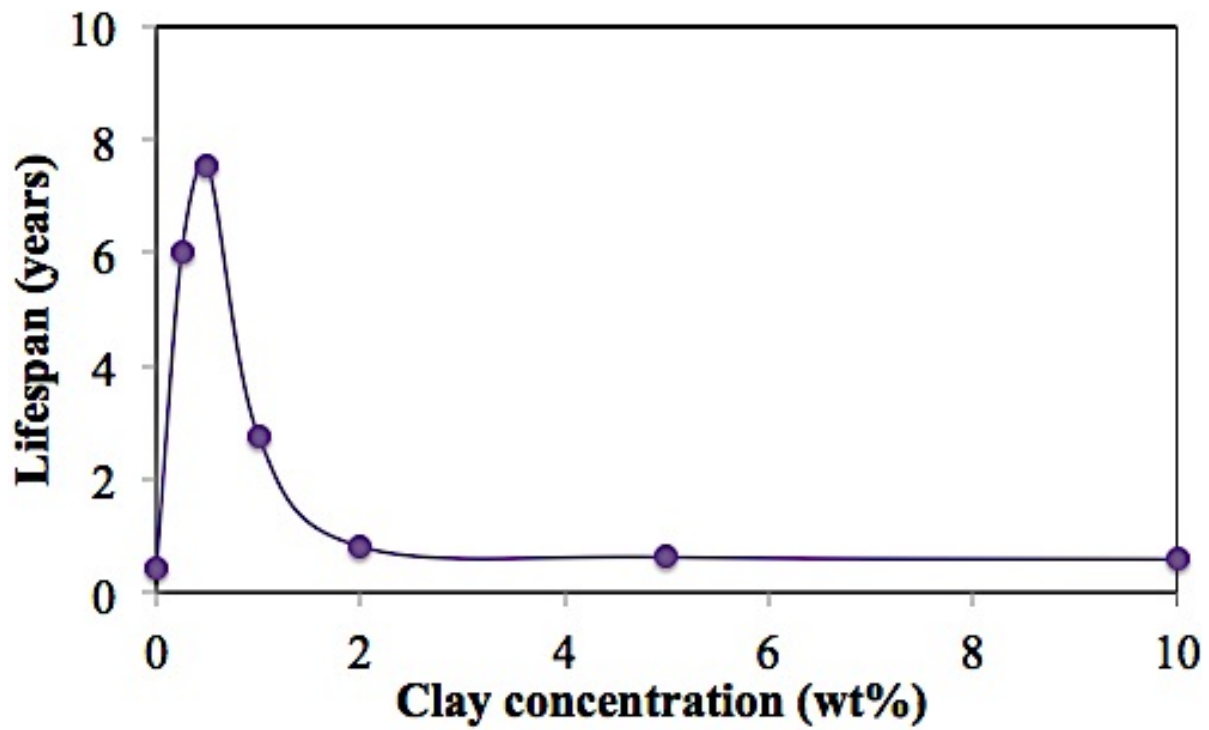


Figure 3.4-24: Predicted coating lifetime of neat PU and PU nanocomposites